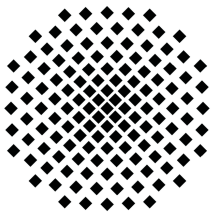

Ultrafast Nonlinear Spectroscopy of Hybrid Plasmonic Systems

Von der Fakultät Mathematik und Physik der Universität Stuttgart
zur Erlangung der Würde eines Doktors der
Naturwissenschaften (Dr. rer. nat.) genehmigte Abhandlung

vorgelegt von
Tobias Utikal
aus Neuwied

Hauptberichter: Prof. Dr. H. Giessen
Mitberichter: Prof. Dr. T. Pfau

Tag der Einreichung: 24. Januar 2011
Tag der mündlichen Prüfung: 23. Februar 2011

Physikalisches Institut der Universität Stuttgart
2011

Was wir wissen, ist ein Tropfen,
was wir nicht wissen, ein Ozean.

Sir Isaac Newton

Zusammenfassung

Die vorliegende Arbeit behandelt sowohl die nichtlinearen optischen Eigenschaften als auch die ultraschnelle zeitliche Dynamik von plasmonischen Hybridstrukturen. Als Modellsystem dienen metallische photonische Kristalle, in denen sowohl lokalisierte plasmonische Moden in einem metallischen Nanogitter als auch photonische Moden in einem Schichtwellenleiter gleichzeitig angeregt werden können. Durch die Kopplung der Moden kommt es zur Ausbildung von polaritonischen Eigenzuständen, die zu signifikanten Änderungen der linearen optischen Eigenschaften und der Dephasierungsdynamik führen.

Im ersten Teil der Arbeit wird die ultraschnelle zeitliche Dynamik auf einer Femtosekunden Zeitskala mithilfe einer nichtlinearen Autokorrelationstechnik untersucht. Das polaritonische Systems hat einen deutlichen Einfluss auf die Form der gemessenen Autokorrelationsfunktion. Unter Ausnutzung eines harmonischen Oszillatormodells können die Dephasierungszeiten aus den Autokorrelationsfunktionen extrahiert werden. Es zeigt sich, dass die Hybridisierung zu einer deutlichen Verlängerung der Dephasierungszeiten führt. Zusätzlich stellt sich heraus, dass die vollständige spektrale Information in Amplitude und Phase aus den Daten erhalten werden kann. Damit liefern die nichtlinearen Messungen einen deutlichen Mehrwert im Vergleich zu rein linearen Messungen.

Der zweite Teil der Arbeit beschäftigt sich konkret mit den nichtlinearen optischen Eigenschaften von plasmonischen Hybridstrukturen. Mithilfe von Spektroskopiemethoden im Spektralbereich der dritten Harmonischen zeigt es sich, dass sich die nichtlinearen optischen Spektren in ihrer Form deutlich von den linearen Spektren unterscheiden. Durch sorgfältige Variation sowohl der Strukturgeometrie als auch der beteiligten Materialien kann der Ursprung des nichtlinearen Signals eindeutig aus den nichtlinearen Spektren bestimmt werden. Verschiedene theoretische Ansätze erhärtet diese Beobachtungen.

Im letzten Teil werden die verlängerten Dephasierungszeiten schließlich ausgenutzt, um die polaritonischen Eigenmoden kohärent zu kontrollieren. Diese werden dabei durch einen ersten extrem kurzen Laserpuls angeregt. Je nach exakter Zeitverzögerung zum ersten Laserpuls schaltet ein darauf folgender zweiter Laserpuls sowohl die kohärente Anregung als auch die nichtlineare Antwort nach einigen zehn Femtosekunden aus oder erneut an. Durch einen dritten Laserpuls ist dabei die zeitliche Auflösung des gesamten Kontrollprozesses gegeben. Da im nichtlinearen Signal ein ausgeprägter Kontrast zwischen An- und Ausschalten erzielt werden kann, eignet sich diese Methode ideal für Anwendungen, die auf ultraschnellem plasmonischen Schalten basieren.

Abstract

In this thesis, the nonlinear optical properties as well as the ultrafast temporal dynamics of hybrid plasmonic systems are studied. The model system under investigation simultaneously provides localized plasmonic modes in a metallic nanowire grating and photonic modes in an adjacent dielectric waveguide slab. The coupling of the modes leads to the formation of polaritonic eigenstates and significant variations in the linear optical spectra as well as in the dephasing dynamics.

In the first part, the ultrafast temporal dynamics on the femtosecond timescale are studied by a nonlinear autocorrelation technique. The linear optical response of the polaritonic system has a major influence on the shape of the autocorrelation function. By employing a harmonic oscillator-based model, the dephasing times are extracted. Due to the hybridization, significantly prolonged dephasing times are observed. Furthermore, the full spectral response, i.e., amplitude and phase, is retrieved from the experimental data which renders the nonlinear experiments distinctly different from purely linear experiments.

The second part concentrates on the nonlinear response of the hybrid plasmonic structure. From third harmonic generation spectroscopy it is found that the shape of the nonlinear optical spectra is completely different when compared with the linear spectra. By carefully varying the structure geometry as well as the constituent materials, the origin of the nonlinearity can be unambiguously identified from the shape of the nonlinear spectra. The observations are confirmed by several theoretical considerations.

In the last part, the prolonged dephasing times of the polaritonic eigenmodes are finally utilized for coherent control experiments. Here, one eigenmode is excited by a first ultrashort laser pulse. Subsequently, a few tens of femtoseconds after the excitation, the eigenmode as well as its nonlinear response is either turned on or off by a second laser pulse dependent on the exact time delay between the pulses. A third laser pulse provides the necessary temporal resolution of the whole control process. Due to the high signal contrast between the suppressed and the reexcited case this technique is suitable for ultrafast plasmonic switching.

Publications

Parts of this work have already been published:

In scientific journals:

- T. Utikal, T. Zentgraf, T. Paul, C. Rockstuhl, F. Lederer, M. Lippitz, and H. Giessen, *Towards the origin of the nonlinear response in hybrid plasmonic systems*, Phys. Rev. Lett. in press (2011)

- T. Utikal, M. I. Stockman, A. P. Heberle, M. Lippitz, and H. Giessen, *All-optical control of hybridized plasmon polaritons in metallic nanostructures*, Phys. Rev. Lett. **104**, 113903 (2010)

- T. Utikal, T. Zentgraf, J. Kuhl, and H. Giessen, *Dynamics and Dephasing of plasmon polaritons in metallic photonic crystal superlattices: Time- and frequency-resolved nonlinear autocorrelation measurements and simulations*, Phys. Rev. B **76**, 245107 (2007)

At international conferences and workshops:

- T. Utikal, T. Zentgraf, T. Paul, C. Rockstuhl, F. Lederer, M. Lippitz, and H. Giessen, *Towards the origin of optical nonlinearities in hybrid plasmonic systems*, talk TUE2s.3, Nanometa, Seefeld, Austria (2011)

- T. Utikal, T. Zentgraf, M. Lippitz, and H. Giessen, *Group index enhanced third-harmonic generation in hybrid plasmonic systems*, 2nd International Workshop on Ultrafast Nanooptics, Bad Dürkheim, Germany (2010)

- T. Utikal, T. Zentgraf, M. Lippitz, and H. Giessen, *Third-harmonic generation spectroscopy in hybrid plasmonic systems*, talk O 32.2, DPG Spring Meeting, Regensburg, Germany (2010)

- H. Giessen, N. Liu, T. Utikal, M. Geiselmann, and M. Lippitz, *Coherent processes in 3D optical metamaterials and metallic photonic crystals*, 2nd international conference on metamaterials, photonic crystals, and plasmonics, Cairo, Egypt (2010)

- T. Utikal, M. I. Stockman, A. P. Heberle, M. Lippitz, and H. Giessen, *Ultrafast coherent control of hybridized plasmon polaritons in metallic nanostructures*, invited talk 7600-20, SPIE Photonics West, San Francisco, USA (2010)

- T. Utikal, M. I. Stockman, A. P. Heberle, M. Lippitz, and H. Giessen, *Ultrafast coherent control of plasmon polaritons on the nanoscale*, talk EI5.1, European Quantum electronics Conference (EQEC), München, Germany (2009)

- T. Utikal, M. I. Stockman, A. P. Heberle, M. Lippitz, and H. Giessen, *Ultrafast coherent control of nonlinear optical processes in plasmonic nanostructures*, talk IWA7, International Quantum Electronics Conference (IQEC), Baltimore, USA (2009)

- T. Utikal, M. I. Stockman, A. P. Heberle, M. Lippitz, and H. Giessen, *Ultrafast coherent control of third-harmonic generation in plasmonic nanostructures*, talk O 20.5, DPG Spring Meeting, Dresden, Germany (2009)

- T. Utikal, M. Lippitz, and H. Giessen, *Coherent control of waveguide-plasmon-polaritons*, talk THU5o.3, Nanometa, Seefeld, Austria (2009)

- T. Utikal and H. Giessen, *Metamaterials and plasmonics*, lecture series, International Workshop on Advanced Materials for Optoelectronics and Related Physics, Puebla, Mexico (2008)

- T. Utikal, M. Geiselmann, A. P. Heberle, M. Lippitz, and H. Giessen, *Coherent control of plasmon polaritons in metallic photonic crystals*, poster, Workshop on Ultrafast Nanooptics, Bad Honnef, Germany (2008)

- T. Utikal, T. Zentgraf, M. Lippitz, and H. Giessen, *Time-resolved optical interferometry of polaritonic states in metallic photonic crystal slabs*, talk QFC6, Quantum Electronics and Laser Science Conference (QELS), San Jose, USA (2008)

- T. Utikal, T. Zentgraf, A. Christ, S. G. Tikhodeev, N. A. Gippius, and H. Giessen, *Tailoring the polaritonic stop gap in metallo-dielectric photonic crystal superlattices*, talk HL 6.2, DPG Spring Meeting, Berlin, Germany (2008)

- T. Utikal, T. Zentgraf, J. Kuhl, S. G. Tikhodeev, and H. Giessen, *Ultrafast polariton dynamics in metallic photonic crystal superlattices*, talk O 13.8, DPG Spring Meeting, Regensburg, Germany (2007)

- T. Utikal, T. Zentgraf, J. Kuhl, and H. Giessen, *Ultrafast nonlinear effects in metallic photonic crystal superlattices*, talk MON5o.2, Nanometa, Seefeld, Austria (2007)

Additional scientific publications which are not presented in this thesis:

In scientific journals:

- D. H. Chae*, T. Utikal*, S. Weisenburger, H. Giessen, K. v. Klitzing, M. Lippitz, and J. Smet, *Excitonic Fano resonances in freestanding graphene*, Nano Lett. **11**, 1379 (2011) (*These authors contributed equally.)

- T. Utikal, T. Zentgraf, S. G. Tikhodeev, M. Lippitz, and H. Giessen *Tailoring the photonic band splitting in metallo-dielectric photonic crystal superlattices*, submitted (2010)

- M. Geiselmann, T. Utikal, M. Lippitz, and H. Giessen, *Tailoring the ultrafast dynamics of the magnetic mode in magnetic photonic crystals*, Phys. Rev. B **81**, 235101 (2010)

At international conferences and workshops:

- M. Hentschel, T. Utikal, M. Lippitz, and H. Giessen, *Size, gap, and material dependence of third harmonic generation from bowtie gapantennas*, poster WED4f.57, Nanometa, Seefeld, Austria (2011)

- S. Weisenburger, T. Utikal, H. Giessen, and M. Lippitz, *Third-harmonic generation from gold nanostructures using a femtosecond laser scanning microscope*, poster O 59.34, DPG Spring Meeting, Regensburg, Germany (2010)

- R. Podzimski, M. Reichelt, T. Meier, T. Utikal, and H. Giessen, *Controlling the third-harmonic generation in a metallic photonic crystal coupled to a waveguide*, poster O 59.36, DPG Spring Meeting, Regensburg, Germany (2010)

- T. Paul, M. Geiselmann, T. Utikal, T. Zentgraf, H. Giessen, C. Rockstuhl, and F. Lederer, *Enhanced third harmonic generation using plasmonic metamaterials*, poster EJ.P.2 MON, European Quantum electronics Conference (EQEC), München, Germany (2009)

- M. Geiselmann, T. Utikal, M. Lippitz, and H. Giessen, *Tailoring polaritonic dephasing in magnetic photonic crystals*, poster EI.P.8 WED, European Quantum electronics Conference (EQEC), München, Germany (2009)

- M. Geiselmann, T. Utikal, M. Lippitz, and H. Giessen, *Dephasing of optical magnetism in magnetic photonic crystals*, poster TUE4f.4, Nanometa, Seefeld, Austria (2009)

Contents

1. Introduction

In the field of optics and light-matter interaction, plenty of research interest has been focused on nanoscopic systems in the near past. Due to extremely sophisticated fabrication techniques, high quality nanostructures such as semiconductor nanowires [1], colloidal semiconductor quantum dots [2], fullerenes [3], carbon nanotubes [4], nitrogen-vacancy centers in diamond [5], or high-Q cavities [6] are produced nowadays. Here, the concentration of electromagnetic radiation onto the nanoscale leads to unprecedented optical effects.

Metallic nanostructures are of particular interest. The free electrons in the conduction band tend to be ideal for light-matter interaction. Usually, only the optimal reflection properties of metals are utilized in optics. However, in metallic nanostructures, which are much smaller than the wavelength of light, a plethora of interesting effects can occur [7, 8]. The illumination by light leads to coherent collective oscillations of the free electrons in the nanostructure, so-called plasmonic excitations, which show a distinct resonance behavior. These plasmonic effects have already been exploited in ancient past in the coloration of glasses, for example in church windows, although a deeper physical understanding was lacking. The admixture of powder of noble metals into the glass and the subsequent excitation of particle plasmons leads to the well-known colorful effects.

By exploiting these plasmonic excitations, the macroscopic optical properties of the structures can be engineered nearly at will. This is especially object of optical metamaterial structures whose optical responses are as well dominated by plasmonic effects. They usually contain specifically shaped nanoscopic unit cell building blocks in a periodic arrangement, whose periodicity is much smaller than the wavelength of light. Based on the concept of metamaterials, novel optical effects have been envisioned and presented, such as negative refraction [9, 10], perfect lensing [11], or cloaking [12].

Besides single plasmonic systems, combined structures have recently attracted a lot of interest as well, where plasmonic modes are hybridized with other plasmonic or photonic modes. The concept of plasmon hybridization leads to a further degree of freedom in order to tailor the optical responses of the systems [13]. In particular, the coupling of plasmonic excitations to photonic slab waveguide modes in metallo-dielectric photonic crystals structures has been object of a lot of research [14–18] in the last ten years.

Due to the rapid development of plasmonics, many applications already emerged in the

last years. A major focus is on small volume sensing applications [19, 20]. Here, the substance to be detected influences the dielectric function of the material surrounding the plasmonic structure and leads to a spectral variation of the optical resonances. In further proposals, the applicability of plasmonic structures for cancer therapy was mentioned [21]. Stockman *et al.* introduced the concept of a SPASER, which is an analog of a laser but rather for plasmonic excitations [22–24]. Recently, a plasmonic system has been utilized even for data storage [25].

A further advantage of plasmonic nanostructures lies in the potential of concentrating the electromagnetic radiation to much smaller volumes as it would be possible by focusing with conventional optical elements. Especially, with plasmonic nanoantennas the goal to overcome the Abbe diffraction limit is easily achievable [26–28]. In this manner, plasmonic nanoantennas allow the efficient coupling of light to nanoscopic objects such as single molecules [29] or quantum dots [30, 31] which do not couple efficiently to light themselves. The strong spatial concentration of the light further leads to high field enhancements in the vicinity of the nanostructures, thereby rendering plasmonic systems also interesting for nonlinear optics applications [32].

Despite of many applications and the utilization of the macroscopic optical properties, a deeper understanding of the microscopic effects in plasmonic nanostructures is still required. In particular, the nonlinear optical responses are hardly understood so far. In several preliminary investigations, a variety of sources of the optical nonlinearities has been proposed, for instance bulk and surface effects in the metal [33, 34] or plasmon-mediated field enhancement in the vicinity of the nanostructures [35]. In addition to this, resonance effects and the exact shape of the nanostructure seems to play an important role [36]. Especially, in metallo-dielectric photonic crystal structures, which are subject of this thesis, the contributions of plasmonic modes and photonic modes to the nonlinear response have to be considered simultaneously. So far, a complete microscopic description of the nonlinear optical processes is still lacking. In most theoretical approaches only effective nonlinear coefficients are determined, but their origin is still unclear. Here, novel sophisticated experiments have to be performed in order to systematically study the nonlinear response of plasmonic nanostructures.

Moreover, the temporal dynamics of the collective electron oscillation are highly interesting properties of plasmonic nanostructures. Due to extremely short response times down to the femtosecond scale, experiments in this direction are extremely challenging and have been performed so far by few research groups only [37–40]. However, the ultrafast responses of plasmonic modes together with the electric field localization render metallic nanostructures promising candidates for future integrated devices.

To utilize the ultrafast temporal dynamics in plasmonic systems, methods have to be found in order to control the excitations on the femtosecond time scale. Zentgraf *et al.* demonstrated how the hybridization of plasmonic and photonic modes can lead to strong variations of the dephasing dynamics in plasmonic systems [38]. However, only

static control is archived in this manner and variations in the temporal responses require changes in the structure geometry. Here, a dynamic control of the excitations on the nanoscale is highly desired where a plasmonic system could be turned on or off at any desired time. In order to achieve plasmonic switching, coherent control methods from semiconductor optics could be utilized [41].

For the deeper understanding of the optical responses of metallic nanostructures, chapter 2 provides an introduction to metal optics on the nanoscale. Especially, the contributions to the decay of plasmonic excitations are discussed. After that, the concept of plasmon hybridization is introduced and it is shown that the main principles can already be explained by a classical harmonic oscillator model. A special focus is on the hybridization of localized plasmonic resonances with photonic waveguide modes within a metallic photonic crystal structure. Since their optical properties are well understood nowadays, they serve as model systems for the nonlinear as well as the ultrafast experiments. At the end of the chapter, the fabrication techniques are presented and a theoretical scattering matrix model is discussed in order to describe the linear optical properties of metallic photonic crystals.

The focus of chapter 3 is on the experimental investigation of the plasmonic dephasing dynamics. At the beginning, the concept of nonlinear autocorrelation measurements is explained, where the plasmonic structures serve as the nonlinear medium and the experimental setup is presented. With the help of the harmonic oscillator model, theoretically obtained autocorrelation functions are fitted to the experimental ones and the dephasing times of the plasmonic modes can be extracted. By using more complex plasmonic structures, i.e., magnetic photonic crystals, the advantages of spectrally resolved autocorrelation functions are presented. They also serve as the basis for the retrieval method in the last section which is a further development of frequency-resolved optical gating (FROG). It is shown how the complete optical response information of a plasmonic system, i.e., amplitude and phase can be extracted from spectrally resolved autocorrelation functions.

Although the nonlinear optical properties of plasmonic nanostructures are already exploited in chapter 3, chapter 4 provides a deeper understanding. After a discussion on previous experiments in this direction, a modification of the metallic photonic crystal structures is presented which tends to be ideal for the following experiments. In order to reveal the origin of the nonlinearity in those systems, a new experimental concept based on third-harmonic generation spectroscopy is presented. By systematically varying the constituent materials of the structures, their contribution to the nonlinear response can be unambiguously identified from the nonlinear spectra. Following that, with the help of several theoretical approaches, these findings are confirmed from simulations. In the last part of this chapter, the influence of the group refractive index and slow light onto the nonlinear response has been investigated using simulations.

Chapter 5 concentrates on ultrafast coherent control of plasmonic excitations in metallic

photonic crystal structures. Since the term *coherent control* has been used for a variety of experimental approaches in the past, a short introduction is given in order to put the present experiments into proper context. In the following the all-optical control concept is explained in more detail. After the presentation of the experimental setup, various control results are compared. Since the experimental data contain many details, the harmonic oscillator model is extended in order to explicitly explain the data. Finally, first experimental results on four-wave mixing in metallic photonic crystals are discussed which can serve as a basis for further investigations on the plasmonic dephasing dynamics in the future.

The last chapters conclude the main results and give a short outlook to further experiments and applications.

2. Plasmonics

2.1. Optical properties of metals

Metals such as aluminum, gold, or silver are characterized by a high electrical and thermal conductivity. Thus in optics, they are extensively used as mirrors due to their excellent reflectivity in the visible part of the electromagnetic spectrum. It is commonly known that silver and aluminum provide a reflectivity which is nearly frequency independent in the visible on the one hand. The reflection of gold, on the other hand, becomes smaller for wavelength in the blue part of the spectrum which leads to the yellowish appearance of gold. It turns out that this absorption steams from interband transitions in the band structure of gold.

All these properties can be related to the electron configuration and the band structure of metals. Especially, the quasi-free conduction electrons play a dominant role for the optical properties of metals. Within a simple electron plasma concept, most of the optical properties can be successfully described. In this Drude-Sommerfeld model [7], the dielectric function is given by

$$\epsilon_\omega = 1 + \chi_{DS}(\omega), \tag{2.1}$$

where χ_{DS} is the intraband susceptibility of the free electron gas. The response of a free electron of mass m_e and charge e to an external electric field $\mathbf{E} = \mathbf{E}_0 e^{-i\omega t}$ is described by the equation of motion:

$$m_e \frac{\partial^2 \mathbf{r}}{\partial t^2} + m_e \Gamma \frac{\partial \mathbf{r}}{\partial t} = e\mathbf{E}_0 e^{-i\omega t}. \tag{2.2}$$

The phenomenological damping constant Γ is inversely related to the mean scattering time τ of the electrons. Since the electrons are only quasi-free and couple to bound electrons, the change in the motion of the electrons can be accounted for by introducing an effective electron mass m_{eff}. Note that Eq. 2.2 does not include linear terms as it will be shown for a classical harmonic oscillator later. Using the material polarization

$$\mathbf{P} = e n_e \mathbf{r} = \epsilon_0 \chi_{DS} \mathbf{E}, \tag{2.3}$$

with the electron density n_e, the Drude-Sommerfeld susceptibility follows as

$$\chi_{DS} = -\frac{\omega_p^2}{\omega^2 + \Gamma^2} + i\frac{\omega_p^2 \Gamma}{\omega(\omega^2 + \Gamma^2)} \qquad \text{with} \qquad \omega_p = \sqrt{\frac{n_e e^2}{\epsilon_0 m_e}}. \tag{2.4}$$

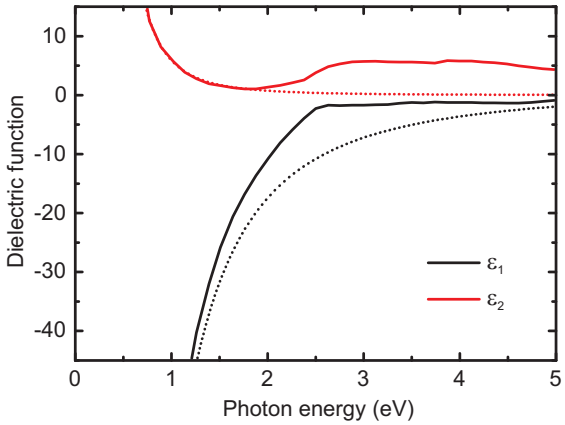

Figure 2.1.: Dielectric function of gold as a function of the photon energy. Experimentally measured values taken from [42] (solid lines) and theoretical fits using the Drude-Sommerfeld model (dotted lines).

The frequency ω_p is called plasma frequency and corresponds to the longitudinal collective excitation of the electron plasma in the bulk metal. If the influence of the damping is neglected ($\Gamma << 1$), ω_p is the eigenfrequency of an ideal volume plasmon.

From Eq. 2.1 and 2.4 it is found that the dielectric function can be decomposed in a real and an imaginary part:

$$\epsilon(\omega) = \epsilon_1(\omega) + i\epsilon_2(\omega). \tag{2.5}$$

The real part corresponds to the dispersion of the material and is related to the refractive index $n^2 = \epsilon_1$ while the imaginary part introduces absorption for incident light.

In 1972 Johnson and Christy carefully measured the dielectric function of gold [42]. In Fig. 2.1 real and imaginary part of the dielectric function are plotted separately. It turns out that the real part, i.e., $\epsilon_1(\omega)$, is negative over the whole spectral range. The experimental data can be fitted using the Drude-Sommerfeld susceptibility. Here, a damping constant $\hbar\Gamma = 0.08$ eV and a plasma frequency $\hbar\omega_p = 8.6$ eV were retrieved. For small frequencies (photon energies up to 2 eV) the agreement to the experimental data is quite good. However, for larger photon energies strong deviations of the experimental data from the model are obvious. These differences can be explained by interband transitions from the $5d$ band to the $6sp$ band in gold, starting from 2.48 eV, which are not included in the Drude-Sommerfeld model. For silver and aluminum, where the interband transitions start at much higher energies, the agreement of the model to experimental data is much better.

The interband transitions in gold are a disadvantage for optical experiments. However, in most cases, gold is the metal of choice due to convenient handling in the fabrication. For silver and aluminum, the interband transitions are shifted far to the blue and do not disturb the spectra in the visible. Here, oxidation is a disadvantage, especially for

silver nanostructures, which destroys the quality of the optical properties.

Besides the reflection properties of metals, the dielectric function can be utilized as well to calculate the skin depth of metals. This is the penetration depth δ of an electromagnetic wave with intensity I_0 which is incident normal to a metal surface. Considering Beer's law of absorption the intensity of the light drops as

$$I(z) = I_0 e^{-\alpha z} \tag{2.6}$$

From the imaginary part of the dielectric function, α is calculated. For a photon energy of 2 eV one finds a skin depth for gold of $\delta = 31$ nm [7]. The metallic nanostructures, which will be discussed later, typically have a thickness which is smaller or similar to the skin depth.

2.1.1. Surface plasmon polaritons

The collective electron excitations in metals give rise to various phenomena where only bulk plasmons were mentioned so far. The situation gets more complex when the dimensionality of the metal is reduced and when interfaces (e.g. metal-to-air) are introduced. Now, even for energies below the plasma frequency, bound surface modes exist due to the broken symmetry of the system. These surface plasmon polaritons (SPP) can be interpreted as bound or evanescent solutions of Maxwell's equations [43, 44]. The periodic displacement of the electrons leads to a charge density modulation or surface waves and electromagnetic field components parallel and perpendicular to the metal surface. The dispersion relation of p-polarized SPP is given by [45]

$$k_x = \frac{\omega}{c}\left(\frac{\epsilon_m \epsilon_d}{\epsilon_m + \epsilon_d}\right)^{1/2}, \tag{2.7}$$

where ϵ_m and ϵ_d are the permittivity of the metal and of the adjacent dielectric material, respectively. The dispersion relation reflects the non-radiative character of the SPP. It cannot couple to light since the wave vector k_x always remains smaller than ω/c. Therefore the dispersion relation is always below the light line. This also means that SPP cannot be directly excited by an external light field. However, by introducing a periodic corrugation on top of the metal film, the wave vector acquires an additional component due to the periodicity d_x and the SPP can be externally excited. The momentum matching condition for the wave vector of the SPP, k_{SPP}, is described by the relation

$$k_{SPP} = k_x + g\frac{2\pi}{d_x} \qquad \text{with} \qquad g = \pm 1, \pm 2, \ldots. \tag{2.8}$$

From another viewpoint the grating folds the dispersion relation back to the first Brillouin zone and the dispersion relation subsequently continues above the light line. The same concept will be exploited later in the excitation of photonic slab waveguide modes.

2.2. Particle plasmon polaritons

If the dimensionality of the metal is further reduced to a quasi one-dimensional (1D) structure, i.e., a metallic nanoparticle, the optical response becomes even more complex and resonances are found in the visible spectrum.

Already in 1908, Gustav Mie presented an analytic solution for the light scattering and the extinction of small spherical metal particles [8]:

$$\sigma_{sca} = \frac{2\pi}{|\mathbf{k}|^2} \sum_{n=1}^{\infty} (2n+1) \cdot \Re(a_n + b_n) \tag{2.9}$$

$$\sigma_{ext} = \frac{2\pi}{|\mathbf{k}|^2} \sum_{n=1}^{\infty} (2n+1) \cdot (|a_n|^2 + |b_n|^2). \tag{2.10}$$

σ_{sca} and σ_{ext} are the cross-sections for scattering and extinction, respectively, when light with wave vector $\mathbf{k}$ impinges on a metal particle. In the theory of Mie the electromagnetic field is divided in spherical multipoles and the scattered field is described as a superposition of these modes of order n with the weighting factors a_n and b_n. For small particles, dipole approximations (n=1) already lead to reasonable results.

In contrast to the two-dimensional (2D) surfaces, the particle provides all necessary wave vectors for the coupling to the external light field due to the spatial confinement. Therefore plasmon resonances can be directly excited with an external light field [see Fig. 2.2(a)]. The electric field displaces the free conducting electrons with respect to the positively charged lattice. The electrons experience a restoring force and start to oscillate within the metal particle at optical frequencies. The charge separation leads to a localized electric field with a dipole-like field distribution. It is confined to the small nanoparticle and can therefore be quite large. Due to the localization, the plasmon oscillation is called localized surface plasmon polariton or particle plasmon polariton (PPP). It has been found that the amplitude of the electron oscillation in the nanoparticle is much smaller than the particle and even the atomic radius and just on the order of $|x| = 0.01$ nm [46].

In the dipole approximation, the dipole moment p of the PPP, which is excited by an external electromagnetic field $\mathbf{E}$, can be written as [47]

$$p = \alpha \mathbf{E} \qquad \text{with} \qquad \alpha = 4\pi R^3 \frac{\epsilon_m - \epsilon_d}{\epsilon_m + 2\epsilon_d}, \tag{2.11}$$

where α is the polarizibility, R is the particle radius, ϵ_m the permittivity of the particle, and ϵ_d the permittivity of the surrounding dielectric. In this quasi-static regime, resonances are found if the denominator approaches a minimum. This is achieved if $\epsilon_m \to -2\epsilon_d$.

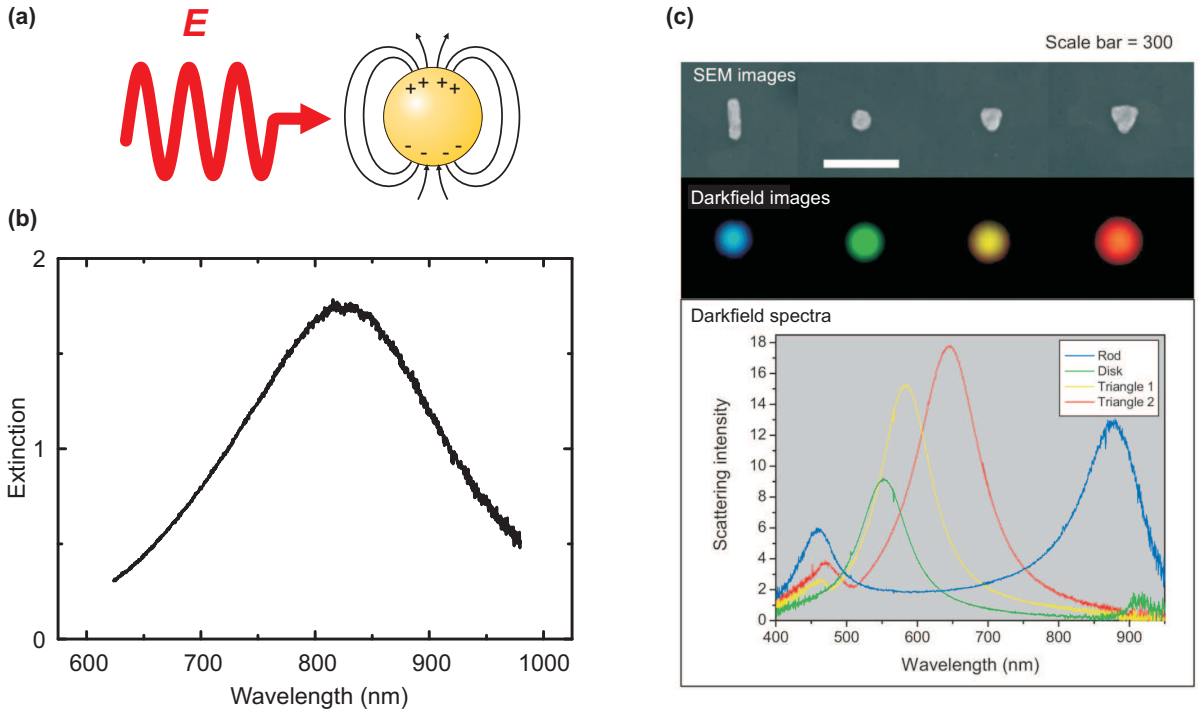

Figure 2.2.: (a) Schematic of the charge distribution in a metallic nanoparticle which is excited by an external electromagnetic light field. (b) Broad extinction resonance of a PPP in the visible spectral range. (c) The spectral position of the PPP resonance as well as the color of the scattered light field depends on the size and the shape of the nanoparticle (from [47]).

In linear extinction ($= -\ln(T), T$: transmission) spectra, the broad resonances are clearly visible. Figure 2.2(b) shows a PPP resonance centered at 820 nm. In this case the particle size is $\approx$ 100 nm. From Mie theory (compare Eq. 2.11) it is obvious that the surrounding dielectric influences the resonance position of the particle. Since the particles are mostly supported by a dielectric glass or quartz substrate, its dielectric function ϵ_d has to be taken into account for the resonance position. This fact makes metal nanoparticle also suitable for sensing applications [19]. If the surrounding dielectric, which could be a liquid as well, changes its refractive index, the PPP resonance is shifted in the spectrum and the shift leads to a transmission variation at a fixed wavelength. However, the shifts are in general rather small and the broad PPP resonance prevents a high sensitivity. It will be shown later how the sensitivity can drastically be increased by plasmon hybridization.

For particles with diameters of more than 10 nm the size influences the resonance position. Increasing the particle diameter shifts the resonance to the red. For particles, which are smaller than 10 nm, the size has no influence on the resonance position any more. However, the resonance shifts if the shape of the particle is changed. Figure 2.2(c) shows dark field scattering images of small metal nanoparticles with different shapes [47]. A rod appears blue in the dark field image and has its resonance around 450 nm. The sphere possesses its resonance at 550 nm and displays a green dark field image. If the shape is changed from the sphere to a triangle, the resonance is further shifted towards 600 nm and an increase of the triangle size leads to an additional red shift.

The resonance position is also influenced by the material of the particle. Silver and aluminum are interesting candidates since they have no interband absorption in the visible such as gold and provide resonance frequencies down to the blue. However, the oxidation of silver nanoparticles is a disadvantage. Therefore gold will be the material of choice throughout this thesis.

2.2.1. Spectral linewidth and dephasing of particle plasmon polaritons

In order to gain more insight into the optical resonance behavior of metal nanoparticles, a simple classical model is introduced in the following which will be the basis of most of the theoretical considerations in this thesis. Due to the dipole-like oscillation of the free electrons in the nanostructure, the PPP can be regarded as a driven and damped harmonic oscillator. Mathematically, a classical mechanical harmonic oscillator which is driven by an external force $F(t) = F_0 e^{i\omega t}$ is described by a differential equation for its displacement $x(t)$:

$$m\frac{d^2x(t)}{dt^2} + \gamma^*\frac{dx(t)}{dt} + Dx(t) = F(t), \tag{2.12}$$

where m is the oscillator mass, γ^* the damping constant, and $Dx(t)$ the restoring force. The amplitude x_0 of the oscillator as a function of the frequency is given by a Lorentzian curve

$$x_0(\omega) = \frac{F_0}{\sqrt{m^2\left(\omega_0^2 - \omega^2\right)^2 + (2\gamma\omega)^2}}, \tag{2.13}$$

where $\omega_0 = \sqrt{\frac{D}{m}}$ and $2\gamma = \gamma^*/m$.

For a PPP, which is driven by an external electromagnetic light field $E(t) = E_0 e^{i\omega t}$, the driving force is $F(t) = -eE(t)$ and Eq. 2.12 can be re-written as

$$\ddot{x}(t) + 2\gamma\dot{x}(t) + \omega_0^2 x(t) = -\frac{e}{m_e} E e^{i\omega t}. \tag{2.14}$$

Here, ω_0 is the resonance frequency of the plasmon oscillation which is determined by the particle size, shape, and material. The damping constant γ is an important measure for the dynamics of the plasmon oscillation. To draw the connection of the damping to the dephasing time of the PPP, the kinetic energy of a damped harmonic oscillator is considered. It decreases exponentially as $W_{kin}(t) \propto e^{-2\gamma t}$. After a time $\tau_p = 1/(2\gamma)$ the energy has dropped to $1/e$. Therefore, τ_p is called plasmon decay time. It is as well closely related to the plasmon dephasing time $T_2 = 2\tau_p$.

Just like for a classical damped harmonic oscillator the broad resonance in the extinction spectrum indicates a strong damping of the electrons oscillating in the nanostructure. In the following the relevant damping processes in metallic nanostructures are discussed in more detail. In general, the damping processes can be divided into radiative and non-radiative decays. The non-radiative processes disturb the collective oscillation of the electrons due to scattering in the metal and lead to a broadening of the PPP resonance. The scattering processes are either elastic, without energy dissipation, or inelastic, including energy dissipation.

The elastic scattering processes of the electrons are dominated by single particle scattering with other electrons (e-e), phonons in the lattice (e-ph), holes (e-h), or scattering at the particle surface (surf). The linewidth Γ is related to the scattering rates $1/\tau_i$ of the processes as

$$\Gamma = \hbar \sum_i \frac{1}{\tau_i} = \frac{1}{\tau_{e-e}} + \frac{1}{\tau_{e-ph}} + \frac{1}{\tau_{e-h}} + \frac{1}{\tau_{surf}} + \ldots. \tag{2.15}$$

The appearance of $\hbar$ shows that Γ is given in energy units. Dependent on the structure of the metal nanoparticle, the scattering rates have different relevances.

The inelastic scattering processes, which are non-radiative, are dominated by the generations of electron-hole pairs (interband absorption) and lead to an additional broadening of the linewidth which is known as Landau damping. However, it has been shown that

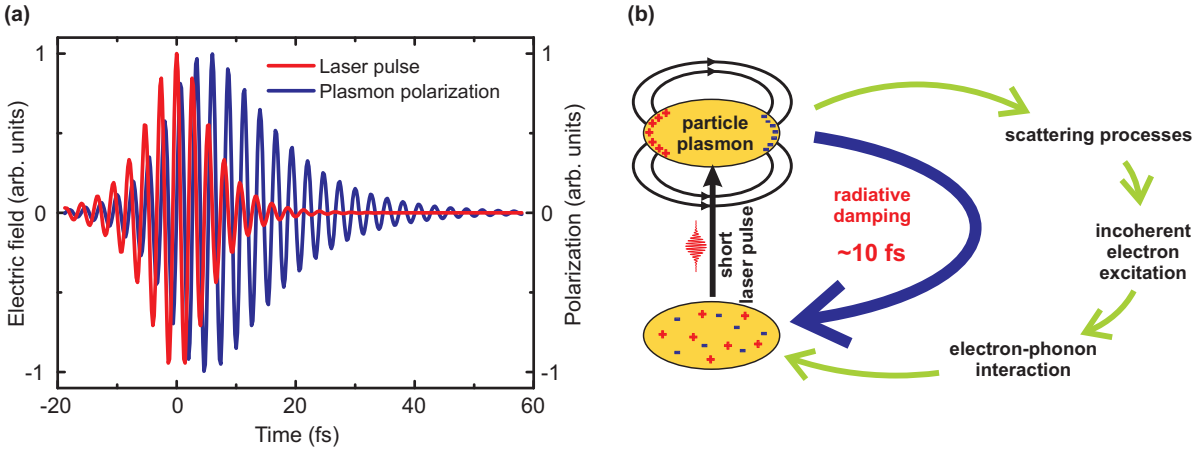

Figure 2.3.: (a) Simulation of the plasmon polarization in the time domain after excitation with an 8 fs laser pulse. A dephasing time of the PPP of $T_2 = 10$ fs is taken into account. (b) The excited PPP can decay via several channels while the radiative decay is the most prominent one for large structures.

these processes can be neglected below photon energies of 2 eV [48] and particle sizes above 5 nm [49, 50].

The radiative decay is another inelastic scattering process, where the electrons lose their energy by emitting photons which leads to an additional damping of the PPP oscillation. For spherical nanoparticles with radius R the radiative relaxation rate can be estimated to be proportional to the volume [51]:

$$\tau_{rad}^{-1} = \frac{2}{3} \cdot R^3 \cdot \frac{\omega^4}{c^3}. \tag{2.16}$$

Qualitatively this relation should also hold for more complicated nanostructures. For particles with a diameter of 100 nm and a wavelength of 800 nm Eq. 2.16 leads to a decay time of 8 fs which is in good agreement with experimental findings [52, 53]. Figure 2.3(a) shows a simulation of the plasmon polarization which is excited by a ultrashort laser pulse with a pulse duration of 8 fs. The PPP is described as a damped harmonic oscillator with a decay time of 10 fs. The plasmon polarization raises together with the electric field of the pulse. At a certain moment after the maximum of the pulse, the decay becomes stronger than the energy transfer from the decreasing electric field of the pulse to the plasmon polarization and the it starts to drop exponentially. The simulation shows that the plasmon polarization is completely lost a few tens of femtoseconds after the laser pulse excitation.

Directly after excitation, the electrons oscillate coherently in the nanostructure. However, due to the scattering processes, the phase relation between the electrons is lost and a coherent light-matter interaction is suppressed. These electrons lose their energy within a few picoseconds mainly due to electron-phonon interaction in the crystal lattice

and the sample heats up. The sample further thermalizes within a few 100 ps and the electrons are in their original state again [compare Fig. 2.3(b)].

The amplitude of the coherent electron oscillation is given by the number of electrons in the nanoparticle. If one electron loses its phase relation to the other electrons, the amplitude of the collective oscillation decreases. The decoherence processes including energy dissipation (radiative decay and inelastic scattering), on the one hand, are commonly characterized by a time constant T_1. On the other hand, the pure dephasing processes without energy dissipation (elastic scattering) are described by a time constant T_2^*. The total decoherence or dephasing time is finally given by

$$\frac{1}{T_2} = \frac{1}{2T_1} + \frac{1}{T_2^*}. \tag{2.17}$$

If an exponentially damped harmonic oscillation of the electrons is assumed, the dephasing time is directly related to the homogeneous linewidth

$$\Gamma_{hom} = \frac{2\hbar}{T_2}. \tag{2.18}$$

It has been found that the radiative decay is the most prominent one in the structures which are utilized in this thesis. Hence, T_1 is always much smaller than T_2^* such that Γ_{hom} is mainly determined by T_1 [52].

The processes discussed so far are only valid for single metallic nanoparticles. However, in the following experiments, large ensembles of nanostructures are investigated. Due to variations in the fabrication process, the nanostructures will always slightly vary in size. This leads to a fluctuation of the PPP resonance frequencies of each nanostructure. A phase shift between the various individual oscillators develops in time and the polarizations of the individual oscillators cancel. The overall coherence of the macroscopic material polarization is lost much faster than the dephasing time T_2 which implies that the resonance in the spectrum is inhomogeneously broadened. In 1999 Lamprecht *et al.* proposed a nonlinear autocorrelation technique to determine the homogeneous broadening of plasmonic resonances [52]. However, in 2005 Klein *et al.* showed that it is not always possible to distinguish between homogeneous and inhomogeneous broadening from a combination of linear and nonlinear optical experiments alone [40]. Only experiments such as four-wave mixing (FWM) or optical rectification can reveal the inhomogeneous broadening. At the end of this thesis, first experimental results on FWM in metallic photonic crystals are shortly discussed. However, scattering electron microscopy (SEM) pictures reveal that the size variation of the structures is rather small, thus inhomogeneous broadening can be neglected in a first approximation.

2.2.2. Field enhancement in plasmonic nanostructures

In order to understand the linear optical properties of plasmonic nanostructures such as scattering or extinction, it is sufficient to consider the far field of the structure alone. However, the optical near field distribution differs significantly from the far field since the electric field vector has to point in the normal direction of the particle surface due to the free electrons in the particle. The concentration of the electromagnetic field to the very small volume of the particle has mainly two consequences. First, it is possible to overcome the Abbe diffraction limit since the particles are much smaller than the wavelength. This is not possible by conventional optical components. Second, due to the field concentration the near fields can be quite strong and enhancement factors f of 10 to 100 are found, especially on resonance [26]. Those strong fields are very interesting for many applications such as surface enhanced Raman scattering (SERS) [54] or nonlinear optical effects.

In order to tailor the field enhancement, the shape of the nanostructures can be optimized. By introducing sharp tips with strong curvatures [27] huge field enhancements have been predicted. For example in bow tie nanoantennas [55] strong fields are expected in the gap region. Recently, the field enhancement in bow tie gap antennas has been utilized for nonlinear optical effects such as high harmonic generation in Argon gas [32]. However, fabrication tolerances set an experimental limitation for the sharpness of the structures and hence to the field enhancement.

Besides the optimization of the nanostructure shape, another property is utilized to enhance the local fields. It can be shown that the field enhancement factor f is directly proportional to the dephasing time of the plasmonic excitation in the structure [52]:

$$f \propto T_2. \tag{2.19}$$

It will be discussed in the following how the dephasing time and subsequently the field enhancement can be increased by the concept of plasmon hybridization.

2.3. Plasmon hybridization

In the discussion so far, the PPP in the metallic nanostructures were considered individually and interactions of PPP in neighboring nanostructures were neglected. However, the coupling of individual nanostructures is an important degree of freedom to tailor the optical properties of plasmonic systems. Since PPP can be regarded as damped harmonic oscillators, the plasmon-plasmon coupling is explained in the following using this classical picture again. PPP couple predominantly via their optical near fields. Since it decays exponentially with increasing distance from the nanostructure, the near field

coupling is only relevant for small distances of neighboring nanostructures on the order of a few nanometers. Starting from Eq. 2.12, two coupled classical harmonic oscillators (1 and 2) are mathematically written as

$$m\ddot{x}_1 + \gamma^*\dot{x}_1 + Dx_1 + D_F(x_1 - x_2) = q_1F(t) \quad (2.20)$$
$$m\ddot{x}_2 + \gamma^*\dot{x}_2 + Dx_2 - D_F(x_1 - x_2) = q_2F(t). \quad (2.21)$$

q_1 and q_2 determine the coupling strength to the driving force and D_F represents the coupling strength of the two oscillators. In the schematic in Fig. 2.4(a) the coupling of the two individual pendula is mediated by the spring.

To solve this set of differential equations one usually introduces two new variables $x^+ = x_1 + x_2$ and $x^- = x_1 - x_2$ and obtains two uncoupled differential equation by adding and subtracting Eq. 2.20 and 2.21:

$$m\ddot{x}^+ + \gamma^*\dot{x}^+ + Dx^+ = 0 \quad (2.22)$$
$$m\ddot{x}^- + \gamma^*\dot{x}^- + (D + 2D_F)x^- = 0 \quad (2.23)$$

To simplify the derivation, the excitation is assumed to be zero, i.e., $q_1 = q_2 = 0$. These uncoupled differential equations can easily be solved separately leading to two eigenmodes of the coupled system with resonance frequencies ω^+ and ω^-.

In Fig. 2.4(a) the eigenmodes of the two coupled oscillators are shown schematically. The symmetric one corresponds to a displacement of both oscillators in the same direction or in phase. For the other eigenmode the pendula oscillate antisymmetrically or out of phase. Figure Fig. 2.4(b) shows the spectrum of the coupled oscillators where one oscillator is externally driven, i.e., $q_1 = 1, q_2 = 0$. One obtains two peaks as a function of frequency which correspond to the two eigenmodes of the coupled system. The peak at smaller frequencies when compared to a single harmonic oscillator can be associated with the symmetric oscillation of the pendula while the peak at higher frequencies corresponds to the antisymmetric oscillation. The spectral splitting of the two modes is related to the coupling strength which is given by the spring constant in the present example.

In the coupling regime of PPP in two neighboring nanostructures, the interaction can be explained in a similar coupling or hybridization model [13, 56]. The hybridization model is equivalent to molecular orbital theory [57] and has recently been exploited for nanoparticle dimers [56], nanorice [58], and stacked cut-wire metamaterials [59]. Just like the pendula displacement, the relative charge distribution of the two nanoparticles can either be symmetric or antisymmetric. Usually, the eigenmode splitting is displayed in an energy diagram such as Fig. 2.4(c). If the nanoparticles are similar, their resonance energy is the same. In the symmetric case (in horizontal light polarization), the charges in the nanoparticles attract each other. This leads to a reduced restoring force of the electron oscillation inside the structure and hence a lower resonance frequency. Therefore the mode is lowered in energy with respect to the mode of the individual particle. In the

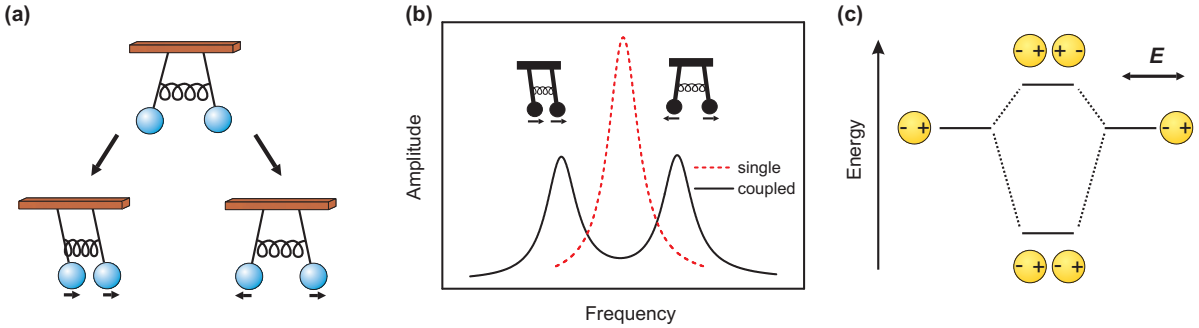

Figure 2.4.: (a) The oscillation dynamics of two coupled harmonic oscillators can be decomposed into two eigenmodes (symmetric and antisymmetric). (b) The symmetric eigenmode leads to a resonance of the coupled system with lower energy than the antisymmetric mode. (c) If two metallic nanoparticles are brought together, the charge distribution can be either symmetric or antisymmetric which leads in a lateral configuration to a reduced and increased resonance energy, respectively.

antisymmetric case the charges in the two nanoparticles repel each other which leads to an increased restoring force. The resonance frequency is higher and the energy of the mode is lifted. Using this simple hybridization model of attraction and repulsion of charges, the spectral mode positions can be qualitatively determined. Recently this model has been utilized to describe more complicated nanostructures consisting of up to seven nanoparticles [60].

2.3.1. Plasmon-induced transparency

To understand the eigenmode splitting of two coupled harmonic oscillators, the individual oscillators were considered to be equal so far. However, in many physical systems this is not necessarily the case. More often the fundamental modes differ strongly in resonance linewidth and excitation strength. Here, asymmetric Fano resonances [61] appear, which arise from the coupling of a narrow resonance (discrete state) with a broad resonance (continuum of states) [62]. It will be shown later that the coupling of asymmetric oscillators results in more degrees of freedom in order to tailor the linear optical responses, the resonance linewidth, and hence the dephasing dynamics.

In atomic physics, Fano resonances are discussed in the framework of electromagnetically induced transparency (EIT) [63–65]. For this effect a three level system is considered where the transition from the ground state $|0\rangle$ to an excited level $|1\rangle$ is dipole-allowed. Coupling of a metastable state $|2\rangle$ to $|1\rangle$ using an external pump laser leads to destructive quantum interference of the excitation pathways $|0\rangle - |1\rangle$ and $|0\rangle - |1\rangle - |2\rangle - |1\rangle$. The effect manifests itself in the broad absorption spectrum of the dipole-allowed transition,

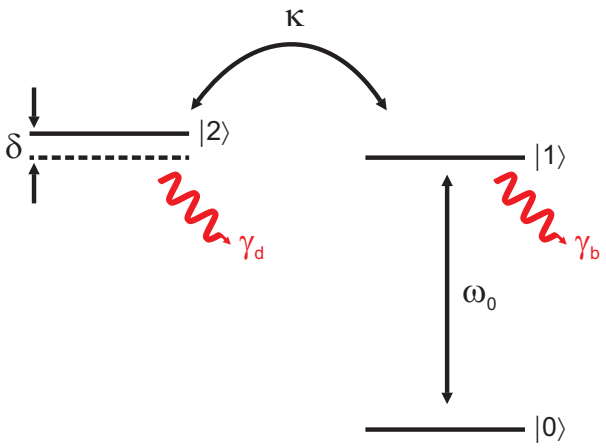

Figure 2.5.: Level scheme of an EIT system. The bright mode $|1\rangle$ can be excited with an external light field and is characterized by a damping γ_b. The dark mode $|2\rangle$ can only be excited by the coupling κ to the bright mode and decays with γ_d.

where a very narrow transparency window appears due to the coupling.

Recently it has been shown that the EIT effect is not restricted to quantum physical systems [66]. Similar effects occur also in purely classical systems like micro-sized optical resonators [67–69] where they can be described as well in the framework of classical harmonic oscillators. Furthermore, Zhang *et al.* theoretically proposed EIT-like effects in a plasmonic *molecule* structure [70] and introduced the term *plasmon-induced transparency*. Figure 2.5 shows a schematic of the involved modes. The structure provides on the one hand a superradiant mode (bright mode) $|1\rangle$ which can be excited by an external light field at frequency ω_0 and which is characterized by a strong damping γ_1. On the other hand, a subradiant mode (dark mode) $|2\rangle$ is required which does not couple to the external field. Therefore its damping γ_2 has to be very low and it is restricted to the Drude losses of the metal. Unlike in the atomic EIT system, the modes are coupled via the optical near fields of the structures. However, the destructive interference of the two modes leads as well to a narrow transmission window in the broad resonance.

Zhang *et al.* proposed an actual example for plasmon-induced transparency where the structure consists of three gold bars which are arranged in a dolmen fashion [see Fig. 2.6(a)]. Upon excitation by light which is polarized along the gold bar to the right, it provides the bright mode which is a fundamental dipole PPP mode. Since the two bars to the left are oriented in the horizontal direction, no fundamental PPP mode can be excited in the pair in the same spectral range. However, the field distribution of the PPP in the bar to the right can induce an antisymmetric field distribution in the pair of bars to the left, such as shown in Fig. 2.6(a). Because of symmetry considerations, this antisymmetric mode (quadrupole mode) cannot couple to the external light field and hence is dark. At the resonance of the dark mode, its back-action on the bright mode

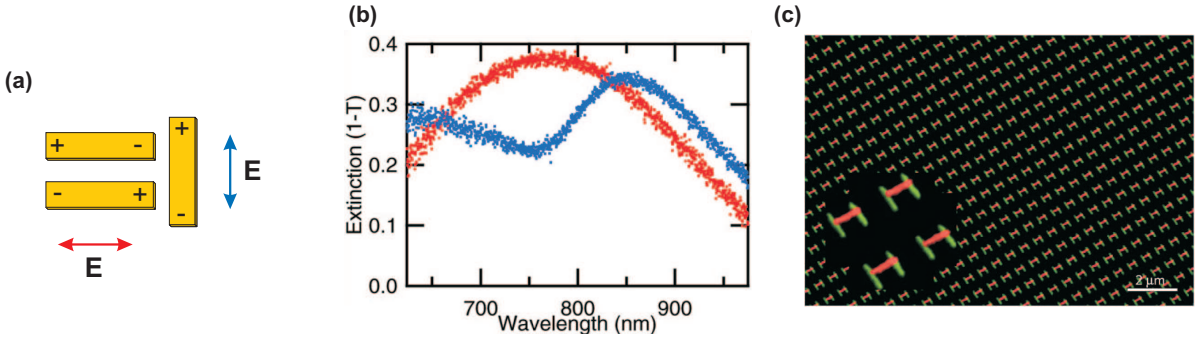

Figure 2.6.: (a) Plasmonic dolmen structure where the bright mode is excited in the single metal bar to the right which couples to the dark mode in the pair of bars to the left. (b) If the light is polarized along the single rod, the spectrum shows an extinction dip. [71]. (c) Three-dimensional (3D) dolmen structure leading to more pronounced EIT dips [72].

has a phase shift of π with respect to the direct excitation of the bright mode, hence the excitations interfere destructively and the bright mode disappears. The broad PPP resonance of the gold bar shows a narrow transmission window, similar to atomic EIT systems.

Using the classical harmonic oscillator model, the two coupled differential equations for the bright mode and the dark mode are

$$\ddot{x}_b + 2\gamma_b \dot{x}_b + \omega_0^2 x_b + \kappa \dot{x}_d = E(t) \tag{2.24}$$

$$\ddot{x}_d + 2\gamma_d \dot{x}_d + (\omega_0 + \delta)^2 x_d - \kappa \dot{x}_b = 0. \tag{2.25}$$

The coupling of the bright mode (subscript b) and the dark mode (subscript d) is denoted by κ. Only the bright mode is externally excited by $E(t)$ and the dark mode might be detuned with respect to the bright mode by δ. In order to obtain the narrow EIT dip, the condition $\gamma_d << \gamma_b << \omega_0$ has to be fulfilled. The ratio of the damping constants is the main condition in order to distinguish plasmon-induced transparency from normal mode coupling [72].

Soon after the theoretical predictions by Zhang *et al.*, Verellen *et al.* realized plasmon-induced transparency experimentally [71]. Figure 2.6(b) shows the relevant spectra. If the light is polarized along the two horizontal wires, it excites the fundamental PPP mode which leads to the broad resonance (red curve). For orthogonal polarization, the fundamental PPP is excited in the vertical bar which couples to the dark mode via the near field. The spectrum shows a dip in the extinction (blue curve). However, in this planar structure, the modulation depth is rather small and the EIT dip is still very broad. Later, in a 3D approach, Liu *et al.* lifted the dipole gold bar above the quadrupole [see Fig 2.6(c)]. In this manner, a more precise control of the distance between the dipole bar and the quadrupole bars is achieved. The near field coupling can be controlled in a

precise fashion and much more pronounced and narrow extinction dips are obtained [72]. It was shown as well that coupling of the bright mode to another bright mode does not lead to the EIT-effect and the narrow spectral features, thus confirming that the low damping of the dark mode is mandatory for EIT.

The narrow extinction dip in the spectrum can be utilized for several applications. In 2010 Liu *et al.* proposed an inverted and planar dolmen structure for an highly efficient glucose sensor [20]. As discussed before a change in the refractive index of the surrounding medium results in a spectral shift of the resonances. Compared to a pure PPP [19], the steep slopes of the resonances in EIT structures lead to drastic changes of the transmission at a fixed wavelength if the resonances are shifted and therefore a high sensitivity.

Another consequence of the narrow extinction dip is a large group refractive index and effects such as slow light in the structures. According to the Kramers-Kronig relation, a drastic change of the imaginary part of the dielectric function, i.e., the absorption, in a small spectral window is accompanied by large variations of the spectral phase. Since the group index is proportional to the derivative of the spectral phase, large values are expected. In chapter 4 the large group index in an EIT-like system will be exploited in order to tailor the nonlinear response of a plasmonic nanostructure.

2.3.2. Photonic waveguide modes

Besides the pure plasmon hybridization, the PPP could as well be coupled to non-plasmonic modes. The hybridization to photonic modes in a slab waveguide is extensively utilized in this thesis and will be discussed now in detail. Photonic waveguide modes are characterized by narrow spectral resonances with low dampings. Their physics is well understood which renders them excellent candidates for plasmon hybridization.

In order to excite photonic waveguide modes, the structure of interest consists of a thin dielectric slab with a thickness h_{wg} roughly between 100 nm and 200 nm on top of a dielectric substrate. If the refractive index of the dielectric slab (ϵ_{wg}) is larger than the refractive index of the substrate (ϵ_{sub}), photonic modes can be guided in this waveguide due to total internal reflection. After solving Maxwell's equations and by assuming boundary conditions, one finds the dispersion relation for the transverse electric (TE) modes [73]

$$\begin{aligned} h_{wg}\sqrt{k_0^2\epsilon_{wg}-k_x^2} = \; & \arctan\left(\sqrt{\frac{k_0^2(\epsilon_{wg}-\epsilon_{air})}{k_0^2\epsilon_{wg}-k_x^2}-1}\right) + \\ & \arctan\left(\sqrt{\frac{k_0^2(\epsilon_{wg}-\epsilon_{sub})}{k_0^2\epsilon_{wg}-k_x^2}-1}\right) + m\pi, \end{aligned} \tag{2.26}$$

and for the transverse magnetic (TM) modes

$$h_{wg}\sqrt{k_0^2\epsilon_{wg}-k_x^2} = \begin{array}{ll} \arctan & \left(\frac{\epsilon_{wg}}{\epsilon_{air}}\sqrt{\frac{k_0^2(\epsilon_{wg}-\epsilon_{air})}{k_0^2\epsilon_{wg}-k_x^2}-1}\right)+ \\ \arctan & \left(\frac{\epsilon_{wg}}{\epsilon_{sub}}\sqrt{\frac{k_0^2(\epsilon_{wg}-\epsilon_{sub})}{k_0^2\epsilon_{wg}-k_x^2}-1}\right)+m\pi. \end{array} \tag{2.27}$$

k_0 and k_x are the vacuum wave vector and the propagation constant within the dielectric slab, respectively. The order of the mode is given by $m = 0, 1, 2, \ldots$. These equations can be solved numerically and lead to the dispersion relation between $\omega = ck_0$ and the propagation constant k_x. Since the surrounding of the waveguide is asymmetric, i.e., $\epsilon_{vac} \neq \epsilon_{sub}$, the modes possess a cut-off frequency of

$$\omega_{cut} = \frac{c\arctan\sqrt{\frac{\epsilon_{sub}-\epsilon_{air}}{\epsilon_{wl}-\epsilon_{sub}}}}{d\sqrt{\epsilon_{wl}-\epsilon_{sub}}}, \tag{2.28}$$

below which propagation is inhibited. TE and TM modes exhibit slightly different dispersion, however, both dispersion curves lie below the vacuum and the substrate light cone. Just like SPPs, they cannot be excited by external light which is incident normal to the surface.

However, if corrugation is introduced at the top of the waveguide, for example by a dielectric grating with a periodicity d_x [see Fig. 2.8 left hand side], the guided modes turn to quasi-guided or leaky modes. The grating vector $g_x = 2\pi n/d_x$ is added or subtracted to/from the wave vector k_0, and momentum mismatch is circumvented:

$$k_x = k_0 \pm g_x. \tag{2.29}$$

The dispersion relation of the disturbed waveguide is found in an empty lattice approximation [74]. The periodicity d_x of the dielectric function $\epsilon(x) = \epsilon(x + d_x)$ of the slab leads as well to a periodic dispersion relation. Within the empty lattice approximation the dispersion relation of the undisturbed system is folded back to the first Brillouin zone. Figure 2.7 shows the periodic dispersion relation for a 180 nm thick hafnium dioxide (HfO_2) waveguide on top of a quartz substrate with a periodicity $d_x = 530$ nm. In this case, the cut-off frequencies are 0.64 eV for the TE-mode and 1.15 eV for the TM-mode, respectively.

The dispersion relation is now characterized by degenerate Bragg resonances at the center $k_x = 0$ and at the edge $k_x = \pm\pi/d_x$ of the first Brillouin zone and the modes lie above the vacuum and the substrate light cone. These quasi-guided modes can now be optically excited upon normal light incidence and have a finite linewidth when compared to the guided modes. Since the size of the Brillouin zone is determined by d_x, the resonance position of the waveguide modes upon normal light incidence can be easily varied by changing the grating periodicity. Upon oblige light incidence the degeneracy of the Bragg resonances is lifted. Besides the symmetric waveguide mode

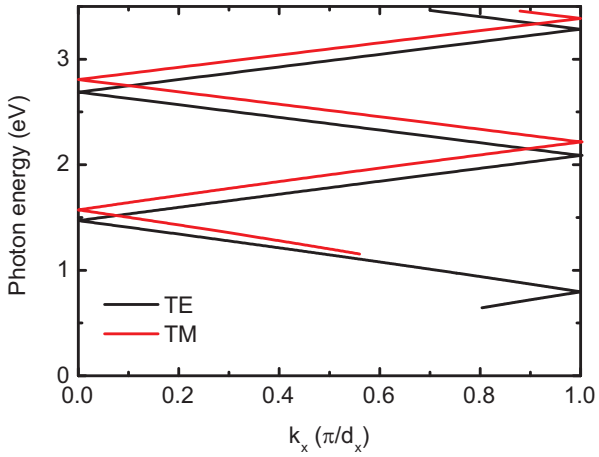

Figure 2.7.: Dispersion of the waveguide modes (TE, TM) within the empty lattice approximation for a 180 nm HfO_2 waveguide and a grating period of 530 nm. The cut-off energies are 0.64 eV (TE) and 1.15 eV (TM), respectively. Due to the symmetry of the dispersion relation, only positive k_x values are plotted.

also the antisymmetric waveguide mode, which is forbidden for $k_x = 0$ due to symmetry considerations, is simultaneously visible in the spectrum [16].

Recently it has been demonstrated how the waveguide mode dispersion can be further tailored. For example by introducing a superlattice structure exhibiting two commensurable or incommensurable periodicities, more than one waveguide mode can be excited in a small spectral range [17]. The occurrence and the resonance amplitude of the modes is determined by the structure factor of the superlattice. Furthermore, disordered gratings have been studied extensively in order to determine fabrication tolerances directly from the linear optical spectra [18].

2.3.3. Waveguide plasmon polariton

To utilize the waveguide modes for plasmon hybridization, the PPP have to be coupled to the waveguide modes. In metallic nanowire structures, PPP can be excited as well if the light polarization is orthogonal to the wire, which thus act as elongated particles [see Fig. 2.8 right hand side]. Therefore, the dielectric grating on top of the waveguide is replaced by a metallic grating [see Fig. 2.8 middle]. Typical parameters for such a metallic photonic crystal structure are $w = 180$ nm as the thickness of the HfO_2 waveguide and $d_x = 530$ nm as the grating period. The cross-section of the wires, usually made out of gold, is typically 100×20 nm^2 [see Fig. 2.9(a)]. The linear optical properties of metallic photonic crystal structures have been extensively investigated over the last years [14–16].

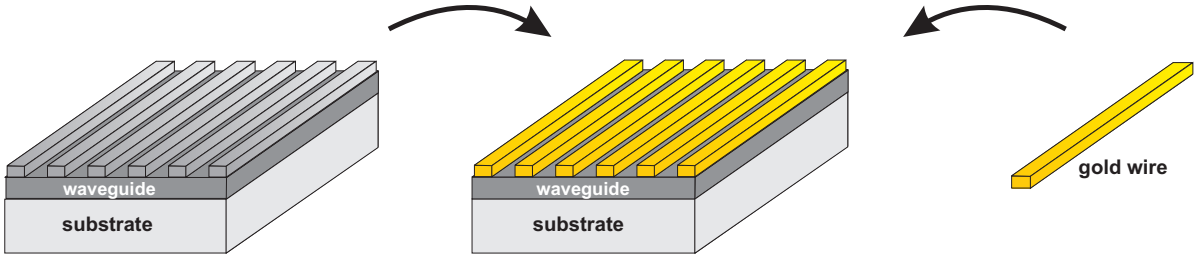

Figure 2.8.: Combination of a gold wire, providing a particle plasmon resonance, and a periodic corrugation on top of a dielectric slab waveguide, leading to a metallic photonic crystal structure.

Photonic crystals in general have been proposed first by Yablonovitch and John in order to inhibit spontaneous emission from a two-level system [75, 76]. They are characterized by a periodic structuring on the order of the light wavelength which leads to the formation of band gaps in the optical dispersion relation and a zero density of state in that gap. Therefore photonic crystals can be considered as semiconductors for photons.

In TE polarization the PPP is switched off and the undisturbed TE waveguide mode is observed [see Fig. 2.9(b)]. Its asymmetry is a clear indication of a Fano lineshape which is due to the coupling of the quasi-guided modes to the vacuum light modes via the grating [62]. However, in TM polarization, where PPP are excited in the wires, the spectrum drastically changes compared to a pure PPP resonance. The structure now supports PPPs in the wires and photonic waveguide modes in the slab, simultaneously. In the spectrum one observes two extinction maxima with an extinction dip inbetween.

In order to understand the linear spectra of the hybridized system, its dispersion relation is considered schematically in Fig. 2.10(a). The resonance position of the PPP is not affected if the grating period d_x is changed. Usually, the distance between the wires is much larger than the leakage of the optical near field around the wires so that the individual nanowires do not couple with each other. However, the resonance position of the waveguide mode can be shifted by changing the grating period. In the regime where the two modes get close to each other one does not observe a crossing of the resonances but rather an anticrossing. This is a typical polaritonic behavior which is well known from excitons in a microcavity [77, 78]. However, the polariton splitting obtained in the metallic photonic crystal structure exceeds the splitting in semiconductors by orders of magnitudes and reaches values of up to 250 meV [16]. In the polaritonic picture the two modes in the anticrossing regime correspond to the two eigenmodes of a so-called waveguide plasmon polariton (WPP).

In Fig. 2.10(b) the linear extinction spectra are simulated for increasing grating periods. The theoretical model is presented later on (compare section 2.6). For $d_x = 350$ nm the waveguide mode at short wavelengths and the PPP at larger wavelengths can be recognized separately in TM polarization. As the grating period is increased, the waveguide

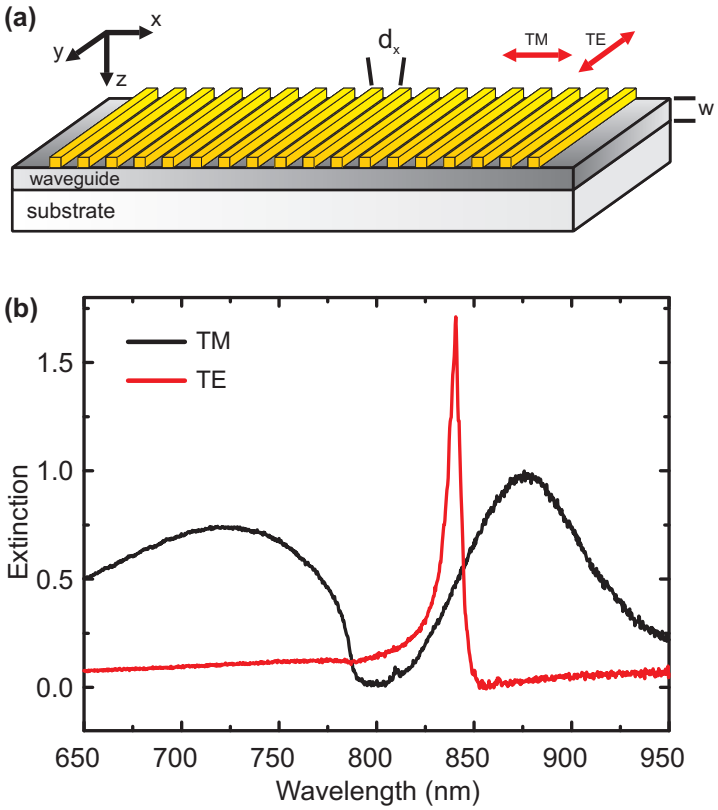

Figure 2.9.: (a) Metallic photonic crystal structure consisting of a plasmonic nanowire grating on top of a dielectric slab waveguide on a quartz substrate. (b) Extinction spectra of the structure under normal light incidence: In TE polarization, only the waveguide mode is excited which leads to a narrow Fano-shaped resonance. In TM polarization, the PPP in the nanowires is hybridized with the waveguide mode, which leads to two polariton branches in the spectrum.

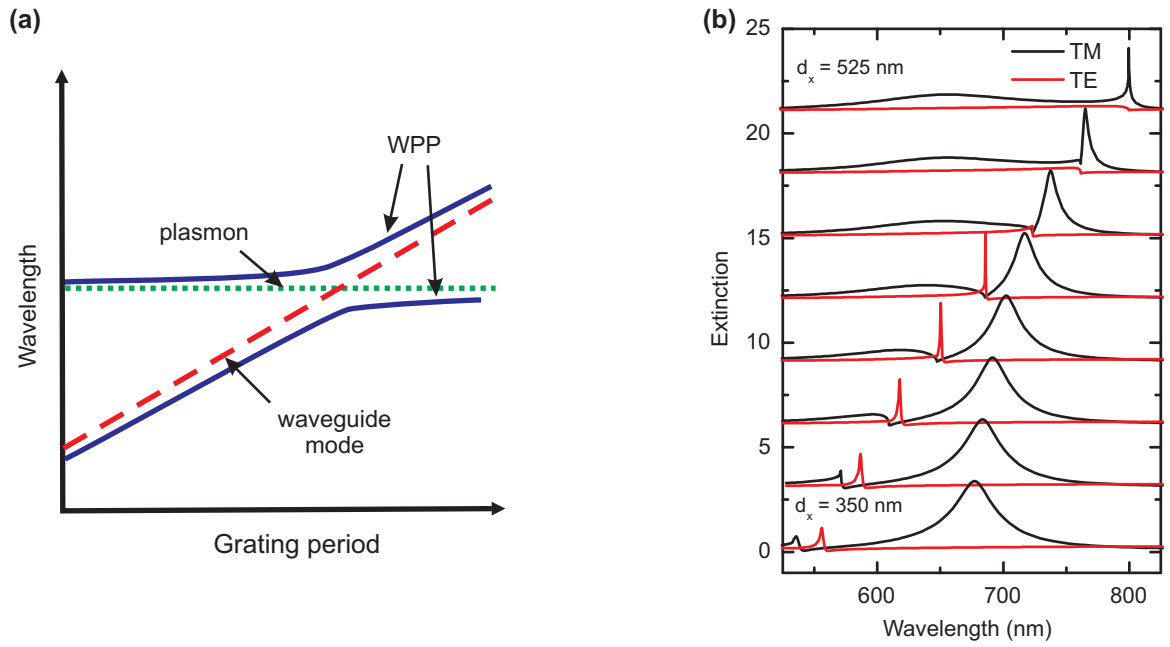

Figure 2.10.: (a) Dispersion relation of the WPP modes showing the polariton splitting between PPP and the waveguide mode schematically. (b) Calculated extinction spectra of metallic photonic crystals for increasing grating periods d_x. The short wavelength mode changes from waveguide character to plasmonic character.

mode is shifted to larger wavelength (compare TE polarization). However, in TM polarization the linewidth of the waveguide mode gradually increases while the linewidth of the PPP mode decreases. In the strong coupling regime ($d_x \approx 450$ nm) the two resonances cannot be identified as the waveguide mode or the PPP mode any more. One rather observes the two resonances of the WPP eigenmodes. For $d_x = 525$ nm the coupling has decreased again and the two resonances have exchanged their character. The PPP is now found at short wavelengths while the waveguide mode is at long wavelengths.

This series of spectra shows that the WPP eigenmodes transform from PPP to waveguide modes and vice versa. Dependent on the grating period the eigenmodes contain either more plasmonic or photonic character. The character can roughly be deduced from the linewidth: The broader the resonance, the more plasmonic character is inherent in the WPP eigenmode. For example in Fig. 2.9(b) the WPP mode at 875 nm is narrower than the mode at 725 nm. Therefore it exhibits more photonic character. Together with the linewidth, also the temporal dynamics of the WPP eigenmodes can be varied over a large range (compare Eq. 2.18). This will be important for the coherent control experiments in chapter 5 where hybrid plasmonic modes with long dephasing times are required.

From a different viewpoint, the extinction dip in between the WPP modes can as well be understood in the framework of EIT [79]. Here, the narrow waveguide mode serves as the dark mode and the PPP in the wires as the bright mode. In chapter 4 it will be shown how very narrow extinction dips are obtained by embedding the plasmonic grating in the dielectric waveguide.

2.4. Sample fabrication

Several methods for the fabrication of periodic metallic nanostructures have been presented in the past. The fabrication method of choice for this thesis is based on electron beam lithography (EBL) and will be discussed in detail in the following [80]. After that, two other promising fabrication methods are shortly presented.

The dielectric material supporting the nanostructures is a commercial 1 mm or 2 mm thick quartz substrate. Quartz is chosen in order to provide transparency in the ultraviolet (UV) at $\lambda = 260$ nm for the nonlinear experiments. On one side of the substrate the thin waveguide layer is deposited using a sputtering technique. Here, HfO_2 with a thickness of 180 nm has been chosen. Its refractive index together with the film thickness guarantee that the cut-off frequency of the waveguide modes is shifted out of the desired spectral region to the near infrared.

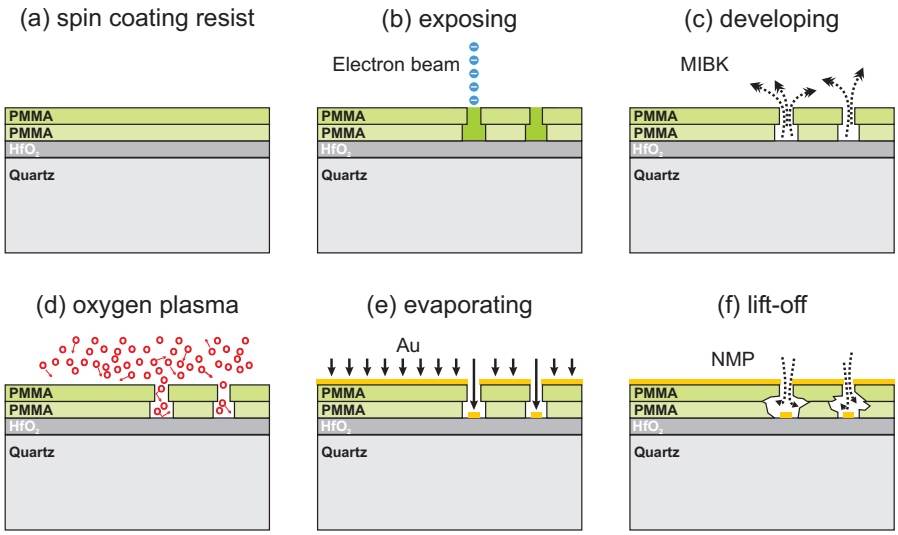

Figure 2.11.: Fabrication process of the plasmonic structures using electron beam lithography and a lift-off process (for further details see text).

After cleaning the substrate in a solvent, the electron beam resist is spin coated on the waveguide layer [Fig. 2.11(a)]. Here, a double layer of poly(methyl methacrylate) (PMMA) is used. The two layers have different molecular weights which results in a higher sensitivity of the lower layer to the electron beam exposure. After spin coating, each layer is baked at 160° C on a hot plate for several minutes to disperse the solvent. During electron beam exposure the electrons have to be drained in order to avoid charging of the substrate. Therefore, a thin (4 nm) layer of chromium is evaporated on the PMMA layers.

The sample is now exposed with the electron beam [Fig. 2.11(b)] in a *Raith E-line* machine. The device allows for write fields of 100×100 μm^2 size. The final spatial resolution is around 20 nm and it is limited e.g. by the proximity effect and the resolution of the resist. Within this work only wire structures have been investigated which simplifies the EBL fabrication process.

After the exposure, the chromium layer is removed with a commercial chromium etching solution. Following that, the electron beam resist is developed using methyl isobutyl ketone (MIBK) [Fig. 2.11(c)]. The different sensitivities of the electron beam resist layers result in an undercut which is advantageous for sharp corners of the nanostructures.

To remove residuals of the electron beam resist, the sample is shortly cleaned in a oxygen plasma [Fig. 2.11(d)]. High-purity gold is thermally evaporated in the next step while the electron beam resist serves as a mask for the nanostructures [Fig. 2.11(e)]. Gold adheres well to the HfO_2 layer. However for other substrates, a thin adhesion layer of chromium has to be used. A typical thickness of the gold structures is 20 nm which is

below its skin depth.

In the last fabrication step the electron beam resist together with the gold on top is removed from the substrate in a lift-off process using N-methyl-2-pyrrolidone (NMP) [Fig. 2.11(f)].

Nearly any structure on a surface can be fabricated with the EBL method. However, one is restricted to 2D structures. Recently an extension of this procedure has been presented, where 3D structures can be realized using a stacking method [81]. The first EBL fabrication process is followed by a planarization of the surface with a dielectric and a second layer can be fabricated on top of the first one. Using metallic alignment marks, the relative orientation of the structures in the different layers with respect to each other is guaranteed with a resolution of 10 nm. Up to five perfectly aligned layers of nanostructures have been realized so far but in principle the number of layers is not limited.

Figure 2.12(a) shows an optical microscope image of a metallic photonic crystal sample with six 100×100 μm^2 fields of gold wire gratings. The cross at the left side serves as a mark for the orientation of the sample in the optical setups. The individual wires can be resolved using a scanning electron microscope. Figure 2.12(b) is a SEM image showing three gold wires of the metallic photonic crystal structure with a very smooth shape. The grating period is 530 nm and the wire width 150 nm. From the SEM images it can be observed that the wire width variation is only a few percent. Therefore it is assumed that the inhomogeneous broadening of the PPP resonance is negligible.

Another cheap and rather simple method to fabricate metallic periodic nanostructures is interference lithography [82]. A dielectric substrate is spin coated with a photo resist in the first step. In an optical interference setup, two beams of a UV laser are aligned with an angle to the normal of the structure and overlapped on the sample. The resulting interference pattern leads to an exposure of the photo resist only at the interference maxima. After the exposure, the photo resist is developed and serves as a mask in the thermal evaporation process. The final nanostructure is obtained after the lift-off. Although the method is rather cheap and large area nanostructures can be fabricated, the quality of the structures is much worse and the resolution is smaller comparable to EBL structures. The shape variation is limited as well.

Recently a third method has been reported, which is cost-effective and allows for the fabrication of large area nanostructures with different constituent shapes [83]. In the first step a Langmuir-Blodgett film of polystyrene microspheres is prepared on the substrate. The holes between the spheres serve as masks in the subsequent thermal evaporation process of the metal. Using a sophisticated rotation of the sample during the evaporation, structures such as split ring resonators, nanospirals, or triangle pentamers can be fabricated. Unfortunately, the structure constituent quality is still not quite as good as EBL structures and the pattern is restricted to a hexagonal shape.

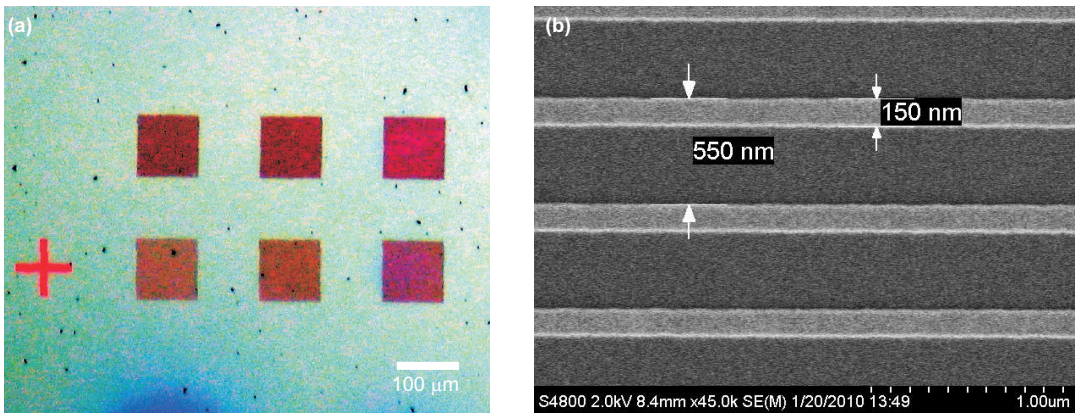

Figure 2.12.: (a) Optical microscope picture of a metallic photonic crystal sample showing six 100×100 μm^2 gold grating fields. (b) Scanning electron microscope picture of several gold wires showing very little size variations.

2.5. White light transmission setup

The linear optical spectra of the metallic photonic crystal structures are measured in a white light transmission setup which is schematically shown in Fig. 2.13. The broadband light of a halogen lamp is collimated and slightly focused onto the sample to a spot size of ≈ 100 μm after passing a linear crystal polarizer. Here, the excitation is set for TE or TM polarization. The sample can be rotated with an angular resolution of 0.5° in order to measure the transmission for different angular excitations. Behind the sample the light is re-collimated with a second achromatic lens and guided to a grating spectrometer with a adjacent liquid nitrogen cooled CCD camera.

The main advantages of the setup are the pinholes before and especially behind the sample. They restrict the light to normal incidence in order to avoid the excitation of the antisymmetric waveguide mode which already appears for incident angles of 0.5°. Especially with the pinhole behind the sample, which has a diameter of 100 μm, only angular components up to 0.2° are detected and the antisymmetric waveguide modes are barely visible in the spectra [compare the small peak at 810 nm in Fig.2.9(c)]. The experimental setup allows to measure the transmitted light intensity I. The extinction is calculated as

$$\text{Extinction} = -ln\frac{I}{I_0}, \tag{2.30}$$

where I_0 is the transmitted light intensity through the substrate and the waveguide but without the plasmonic nanostructures.

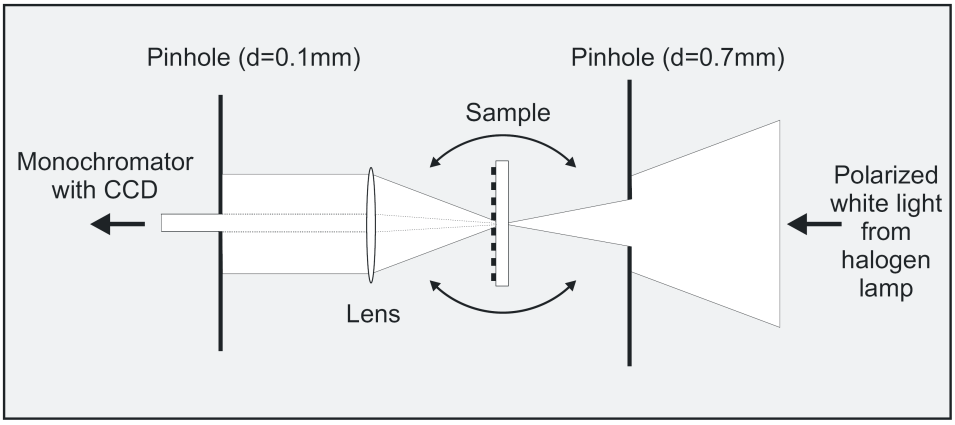

Figure 2.13.: White light transmission setup for linear optical measurements of the plasmonic nanostructures. The pinholes are used in order to reduce the angular components which would excite the antisymmetric waveguide modes in the metallic photonic crystal structures.

2.6. Scattering matrix algorithm

It has been shown that the Mie theory provides exact solutions for the scattering cross-section of spherical metal particles. However, for geometries which are different from a sphere, other theoretical approaches have to be utilized.

In this section, a numerical simulation method is presented which allows to calculate the linear optical responses of periodic nanostructures and layered systems, such as reflection, transmission, and absorption. It is also possible to calculate electric and magnetic field distributions within the structure. This scattering matrix algorithm was first proposed by Whittaker *et al.* [84] and has been extended by Tikhodeev *et al.* [74].

As input parameters only the geometry of the structure together with the dielectric function of the materials has to be implemented. In this thesis the scattering matrix algorithm is utilized for the metallic photonic crystal structures. Figure 2.14(a) shows a metallic photonic crystal structure together with the nomenclature of the involved variables.

In the first simulation step the structure is divided in layers in the z-direction. The Maxwell equations

$$-\frac{1}{c}\frac{\partial \mathbf{H}}{\partial t} = \nabla \times \mathbf{E} \tag{2.31}$$

$$\frac{1}{c}\frac{\partial \mathbf{D}}{\partial t} = \nabla \times \mathbf{H}, \tag{2.32}$$

are solved for each layer separately. For the metallic photonic crystal structures the first

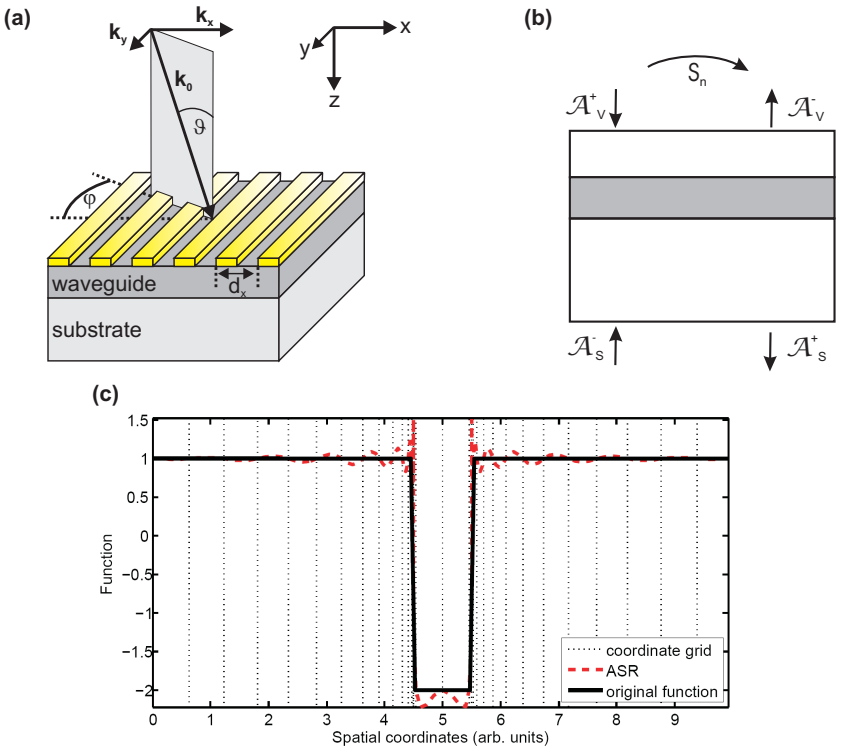

Figure 2.14.: (a) Nomenclature of the sample parameters. (b) Schematic of the scattering matrix algorithm. (c) Example of the coordinate transformation using adaptive spatial resolution for a piecewise constant function (from [85]).

layer contains one unit cell of the periodic gold grating. The periodicity of the dielectric function is contained in $\mathbf{D}$. To solve the Maxwell equations, the electric field in one layer is decomposed in plane waves such as

$$\mathbf{E}(x,y,z,t) = \mathbf{E_G} \exp\left(ik_{x,\mathbf{G}}x + ik_{y,\mathbf{G}}y\right) \times \exp\left(iKz - i\omega t\right). \tag{2.33}$$

The magnetic field is calculated accordingly. The wave vectors are calculated as

$$k_{x,\mathbf{G}} = k_x + G_x \quad \text{and} \quad k_{y,\mathbf{G}} = k_y + G_y \tag{2.34}$$

together with the reciprocal lattice vector

$$\mathbf{G} = (G_x, G_y, 0) = \frac{2\pi}{d_x}(g_x, g_y, 0), \quad g_{x,y} = 0, \pm 1, \pm 2, \ldots, \pm\infty. \tag{2.35}$$

Here d_x is the periodicity of the lattice. Each of the plane waves $\mathbf{E}(x,y,z,t)$ is one Bragg-order (harmonic) of the associated layer. Via Eq. 2.34 the incident light with wave vector $\mathbf{k} = (k_x, k_y, k_z)$ is coupled to all Bragg-orders, i.e., all plane waves which are given by the different values of $\mathbf{G}$. This leads to an infinite number of plane waves which sum up to the total electromagnetic field in the layer. Since an infinite number is not reasonable for the calculations, the sum is truncated at a value g_{max}. Thus the number of harmonics is given by $N_g = (2 \cdot g_{x,max} + 1)(2 \cdot g_{x,max} + 1)$. The accuracy of the calculation increases with N_g however the calculation time scales as N_g^3.

In the next step, the amplitudes of the waves have to be coupled with the waves in the adjacent layers. Therefore, the solutions of the Maxwell equations in each layer are divided into sets of eigenvectors parallel to the z-direction. The amplitudes of the plane waves can be combined to vectors such as

$$\mathbf{A}(z) = \begin{pmatrix} \mathbf{A}^+(z) \\ \mathbf{A}^-(z) \end{pmatrix}. \tag{2.36}$$

All components which propagate in the positive (negative) z-direction are assigned by + (-). Using a transfer matrix $\mathbb{T}_L$ the vectors are coupled at different z-values

$$\mathbf{A}(z+L) = \mathbb{T}_L \mathbf{A}(z). \tag{2.37}$$

The transition from one layer to the adjacent one can be written accordingly

$$\mathbf{A}|_{z=z_{b,a}+0} = \mathbb{T}_{b,a}\mathbf{A}|_{z=z_{b,a}-0}. \tag{2.38}$$

The transfer matrix formalism would be already enough to describe the light propagation in the structure. However it turns out that the algorithm diverges for evanescent waves.

To overcome this problem the scattering matrix algorithm is utilized. Here, the amplitudes of the plane waves which propagate into the sample are combined to a vector

$$\mathbf{B}_{in} = \begin{pmatrix} \mathbf{A}_v^+(z) \\ \mathbf{A}_s^-(z) \end{pmatrix}. \tag{2.39}$$

The subscript v describes the vacuum side at the upper side of the sample, s is for the substrate [see Fig. 2.14(b)]. The amplitudes of the plane waves which propagate out of the sample are combined accordingly.

$$\mathbf{B}_{out} = \begin{pmatrix} \mathbf{A}_s^+(z) \\ \mathbf{A}_v^-(z) \end{pmatrix}. \tag{2.40}$$

In the last step the scattering matrix combines these vectors.

$$\mathbf{B}_{out} = \mathbb{S}_{v,s}\mathbf{B}_{in}. \tag{2.41}$$

The whole scattering matrix is obtained in an iterative fashion. First, the unity matrix is assumed for $N = 0$ layers. Following that, the matrix for $N + 1$ layers is iteratively calculated from the matrix for N layers by utilizing the inverse transfer matrix. Finally, the components of the complete scattering matrix contain the spectral values of the reflection, the transmission, and the absorption of the whole structure.

The bottleneck of the scattering matrix algorithm originates from the periodic metallic nanostructures. In the layer incorporating the nanostructure, the dielectric function undergoes steep steps in the x-direction. For optimum convergence of the algorithm a large number N_g of harmonics has to be used which drastically increases the computation time. Recently, Weiss *et al.* extended the scattering matrix algorithm with an adaptive spatial resolution method in order to account for this problem [85]. The resolution in x-direction is increased at x-values where the dielectric function undergoes steep steps and it is reduced elsewhere. Figure 2.14(c) shows this schematically. With that improvement the number of harmonics N_g for optimum convergence could be reduced by a factor of 10.

Figure 2.15 shows a comparison of the measured extinction spectrum of a metallic photonic crystal in TM polarization together with a scattering matrix simulation. Very good agreement has been found. The peak positions of the WPP modes as well as the linewidths are nearly perfectly reproduced by the simulation. Variations in the extinction amplitude are due to fabrication tolerances, surface roughness, and a finite number of wires which are illuminated in the experiment.

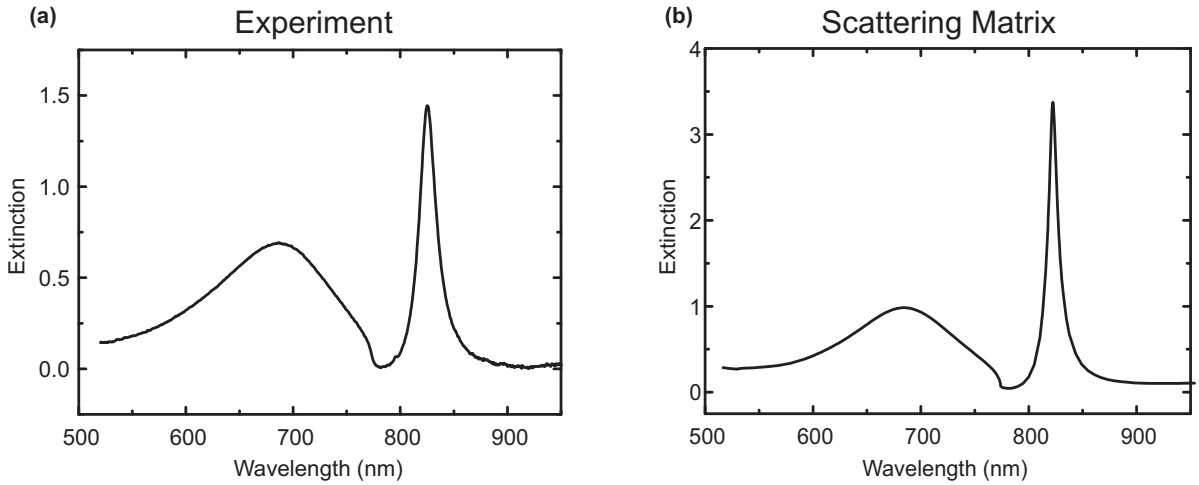

Figure 2.15.: Comparison between a measured (a) and simulated (b) extinction spectrum in TM polarization. Peak positions and linewidths are perfectly reproduced by the scattering matrix simulations.

3. Measuring the plasmonic dephasing

The ultrafast optical response of plasmonic nanostructures, which manifests itself as broad resonances in the linear optical spectra, render them promising candidates for future applications in data processing and integrated devices. In the previous chapter it has been shown that after the excitation with light, the free conduction electrons coherently oscillate in the particle with a fixed phase relation. A coherent light-matter interaction is only possible within that temporal window on the order of a few femtoseconds. This short time scale is a major experimental challenge in order to investigate the temporal dynamics of plasmonic systems.

To directly resolve the temporal evolution of an optically excited system, usually fast photo detectors are utilized. However, their temporal resolution is typically limited to the nanosecond time scale. For faster processes, other experimental techniques have been developed in the past and some of them are shortly presented here. They all utilize the fact that a macroscopic material polarization maps the microscopic processes in the system. The coherent macroscopic material polarization is excited by a short laser pulse in a first step and subsequently probed with a second pulse after a delay. In that way, the influences on the second pulse or additionally generated signals contain the information about the microscopic processes in the system.

A well-known method in optical spectroscopy is the pump-probe technique [86,87]. Here, a first intense laser pulse (pump pulse) excites electrons, excitons, electron-hole pairs, or a material polarization in the sample. The pump pulse duration has to be sufficiently short in order to provide the temporal resolution. Due to the excitation, the dielectric function of the system is change as long as the system remains in the excited state. The changes in the optical properties are measured with a second weak pulse (probe pulse) which does not influence the dielectric function. By varying the time delay between pump and probe pulse, the temporal evolution of the excitations in the system is resolved. This method is typically used on a timescale below 100 fs. For a plasmonic system, the pump-probe technique is disadvantageous since the dielectric function is not influenced significantly. Furthermore, the high pump pulse intensities easily lead to a destruction of the metallic nanostructures. Nevertheless, with a modified pump-probe technique the temporal dynamics of plasmonic systems can be investigated.

In a FWM experiment, pump and probe pulse of equal intensity are combined in the system in a nonlinear fashion. In the first step, the pump pulse with wave vector

k_1 generates a macroscopic material polarization in the sample which decays with the dephasing time T_2. The probe pulse with wave vector k_2 can interact with the material polarization in a a third-order nonlinear process and generate the FWM signal, e.g., in the direction $2\mathbf{k}_2 - \mathbf{k}_1$. This signal as a function of the delay between pump and probe pulse provides information about the temporal evolution of the material polarization. If the FWM signal is further nonlinearly combined with a third pulse, inhomogeneous broadening of the resonances can be distinguished from homogeneous broadening by a photon echo signal. At the end of this thesis, first experimental steps in this direction are presented.

Another well established method is based on two photon photoemission. Here, the pump pulse excites the electrons in a metal to an intermediate state. The subsequent probe pulse provides the energy to emit the electrons into the vacuum. Dependent on the excitation energy and the emission angle, information about the coherence of the intermediate state are deduced. [88,89]. This method was improved by Petek *et al.* with an interferometric two pulse excitation technique in order to measure the dephasing of hot electrons at copper surfaces [90].

In this work, a different two-pulse method to investigate plasmon dynamics is employed which is based on a nonlinear autocorrelation technique. Originally, it had been developed to characterize ultrashort laser pulses. However, it will be shown in the following that this technique can be utilized as well for the investigation of the ultrafast coherent processes in plasmonic systems.

3.1. Nonlinear autocorrelation technique

In laser physics, a similar problem as in plasmonics occurs when it comes to the characterization of ultrashort laser pulses [91]. For pulse durations in the sub-nanosecond regime it is not possible any more to utilize fast photodetectors for gaining temporal resolution. However, a sophisticated correlation technique has been developed in the past in order to circumvent this problem. Here, the electric field evolution of an unknown pulse can be monitored at each time step with a shorter reference pulse such as in a strobe light experiment. Nevertheless, the problem remains how to characterize the reference pulse. It finally turns out that it is sufficient to use the pulse itself as the reference. In an autocorrelation measurement, a pulse pair is generated from the unknown laser pulse, e.g., in a Michelson interferometer. Here, the two pulses travel along different paths where a temporal delay τ between the pulses can be imposed. The pulses are recombined to the same beam again behind the interferometer and the total electric field of the pulse pair can be written as

$$E_{tot}(t,\tau) = E(t) + E(t+\tau). \tag{3.1}$$

The interferometric superposition of the two electric fields leads to a suppression or amplification of the total intensity of the beam as a function of the time delay between the pulses. Since the response time of standard photo detectors is much longer than the oscillation period of the electric field, only the time average of the intensity is measured. The intensity at the detector as a function of the time delay τ can therefore be written as

$$I_{ACF,1}(\tau) \propto \int^{T_R} [E(t) + E(t+\tau)]^2 \, dt, \tag{3.2}$$

where T_R is the detector response time. Equation 3.2 is called first order interferometric autocorrelation function (ACF). It has its maximum for perfect pulse overlap ($\tau = 0$) and is uniform if the delay is large. For delays $\tau > 0$ a fringe pattern is observed dependent whether the two electric field interfere constructively or destructively. However, due to the temporal averaging of the intensity, the phase information of the electric field is lost. Therefore the linear autocorrelation does not provide any further information about the electric field evolution when compared to a spectrogram. If the pulse carrier frequency changes with time (chirped pulses), the pulse duration is prolonged but the shape of the spectrum and the linear ACF are not affected.

To obtain additional information about the electric field of the laser pulses it is mandatory to measure higher order, i.e., nonlinear ACF. Therefore a nonlinear optical medium is used in front of the detection unit where higher harmonics of the electric fields are generated. Details about nonlinear optical processes are the basis of chapter 4. For second harmonic generation (SHG), beta barium borate (BBO) crystals turn out to be an ideal nonlinear medium. Since SHG is a second order nonlinear process the intensity is proportional to the square of the electric field. Thus, the second order ACF is given by

$$I_{ACF,2}(\tau) \propto \int^{T_R} \left[|E(t) + E(t+\tau)|^2 \right]^2 dt. \tag{3.3}$$

Again the second order ACF is maximum for perfect constructive interference of the two pulses and zero if the electric field of the two pulses interfere destructively. Since a second order nonlinear process in involved, the intensity ratio between perfect pulse overlap ($\tau = 0$) and large delays ($\tau >> 0$) is always 8:1 [92]. The period of the interference fringe pattern is directly related to the carrier frequency of the pulses. In contrast to the linear ACF, the second order ACF comprises at least some information about the phase of the electric field and therefore about the shape of the pulses. However it turns out that only linear phase changes can be unambiguously extracted. For the complete information about the electric field of the pulse, all higher order ACFs would be required, which is experimentally not practicable. Nevertheless, by assuming a certain shape of the laser pulses, the pulse duration can already be obtained from an ACF of nonlinear order. Another drawback of nonlinear ACF is its symmetric shape with respect to $\tau = 0$. This leads to an ambiguity in the time direction of $E(t)$.

So far, the ACF method provides information about the shape of ultrashort laser pulses. Throughout the discussion it has been assumed that the response of the nonlinear

medium is instantaneous to the excitation by the laser pulses and that no memory, i.e., coherence, remains in the medium after the pulse. However, this fact will dramatically change if a plasmonic structure is used as the nonlinear medium. Since the coherent electron oscillation remains present in the system for a short period of time after the pulse, the second pulse will not only interact with the first pulse but as well with the coherent material polarization in the sample. This will drastically change the shape of the ACF. It will be shown later how the temporal dynamics of the plasmon excitation can be deduced from the shape of the nonlinear ACF.

3.1.1. Laser system

Another requirement in order to investigate the ultrafast plasmon dynamics is an appropriate light source which provides the relevant temporal resolution. Since the spectral position of the plasmon resonances can easily be shifted to the near infrared, few-cycle Ti:sapphire oscillators render to be ideal for those kind of experiments. In this work a commercial laser (*VENTEON*) with sub-8 fs pulse durations is used which is pumped by a 5.5 W *cw*-solid state laser operating at 532 nm (*Coherent Verdi V10*).

A schematic of the femtosecond laser system is shown in Fig. 3.1(a). The frequencies of the broad emission spectrum of the Ti:sapphire crystal are coupled using Kerr-lens mode locking. Mode locking operation is initiated by shaking one of the cavity mirrors. The dispersion management is accomplished by specifically designed chirped mirrors which are sensitive to the broad emission spectrum. Thus, pulse durations as low as 8 fs can be achieved. Additionally, a pair of glass wedges is placed in the cavity to allow for precise dispersion tuning. The main advantage of the *VENTEON* laser is a rather high average output power of $\approx$ 500 mW which is necessary for the nonlinear experiments.

One major drawback of the laser for the time-resolved ultrafast measurements is the complicated shape of the laser spectrum [see Fig. 3.1(b)]. It stretches from 650 nm to 950 nm but is far away from a Gaussian pulse shape. This observation already indicates that the pulse shape in the temporal domain is as well non-Gaussian. This assumption can be confirmed from SHG autocorrelation measurements using a BBO crystal as the nonlinear medium. The crystal has a thickness of only 20μm in order to achieve phase matching for the broad laser spectrum. Fig. 3.1(c) shows the second order ACF. For perfect temporal pulse overlap ($\tau = 0$) the intensity is maximum and the intensity ratio is 8:1 as theoretically expected. The ACF is perfectly symmetric and shows the fringes which originate from the interference of the electric field of the two pulses.

The electric field envelope of ultrashort laser pulses with a duration of a few femtoseconds is usually described best by a $sech^2$-function. Fig. 3.1(c) shows as well a theoretical fit of the ACF envelope by assuming a $sech^2$-pulse shape with a duration of 8 fs as a fit parameter [93]. For small delays of the pulses the agreement is very good. However,

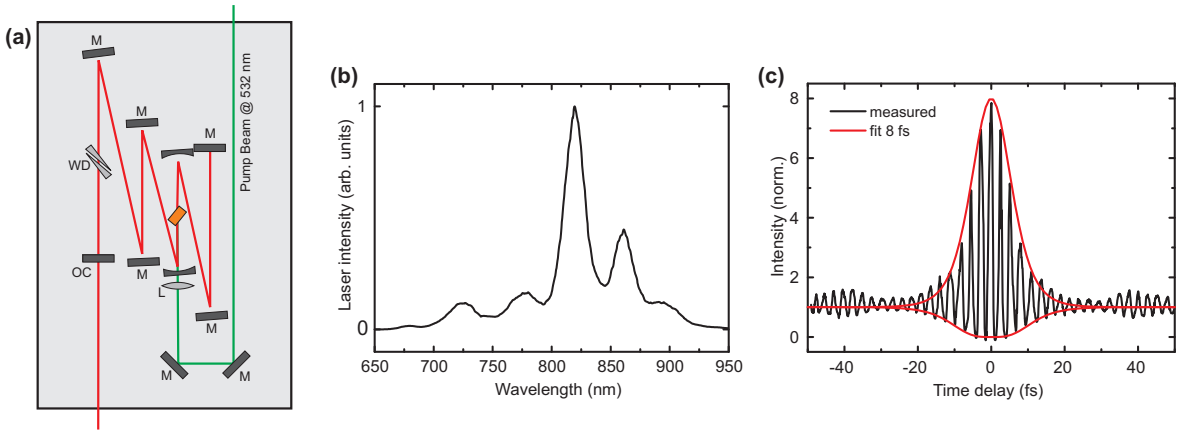

Figure 3.1.: (a) Schematic of the *Venteon* laser. The Ti:sapphire crystal is pumped by a 5.5 W *cw*-laser at 532 nm. The intra cavity dispersion can be optimized using the two wedges (WD). (b) Broad but modulated spectrum of the laser. (c) Second-harmonic autocorrelation function measured data using a BBO crystal together with a fit function. From the fit, a pulse duration of 8 fs is retrieved. Side lobes are visible around ±40 fs which result from satellite pulses.

around delays of 40 fs one observes a second lobe of the autocorrelation envelope which might originate from satellite pulses after the main pulse. For the coherent control experiments, which are discussed in chapter 5, it could be assumed that the satellite pulses are a disadvantage and that pulses with an ideal $sech^2$-shape would be favorable. However, it will turn out that the main control results are achieved even with the non-perfect laser pulses.

Nevertheless, for future ultrafast experiments at the setup it is planed to improve the shape of the laser pulses behind the laser. A promising method in this direction is called multiphoton intrapulse interference phase scan (MIIPS) [94]. Here, using a phase mask the spectral amplitude and phase of the pulses are iteratively varied until the desired pulse shape is achieved. It remains to be seen if the precision of the ultrafast experiments can be further improved by this method.

3.1.2. Experimental setup

Experiments with few-femtosecond laser pulses are extremely challenging mainly due to dispersion of the dielectric optical components and subsequent broadening of the pulses in the temporal domain. Since the laser spectrum is very broad, the various frequencies experience a different dispersion even when passing through air. Therefore the pulse duration is already significantly increased while the beam travels from the laser through

the experimental setup to the sample. To avoid this effect, a pair of chirped mirrors is used together with a pair of adjustable glass wedges right behind the laser. The pulses are pre-compressed by the mirrors, which consist of a multilayer of dielectrics. Since the different spectral components are reflected at different depths in the multilayer, the frequency components can be delayed with respect to each other. Due to dispersive materials in the experiment, they finally retrieve their original pulse duration directly at the sample.

To optimize the pre-compression, the second harmonic ACF is measured *in-situ* using a BBO crystal at the position of the sample. The shape of the autocorrelation is improved by selecting an appropriate number of bounces of the beam on the chirped mirrors and finally by fine-tuning of the dispersion using the glass wedges. Nevertheless, any dispersive optical components such as filter glass or lenses in the experimental setup are avoided.

The most sensitive part of the experimental setup is the actively stabilized Michelson interferometer. It allows to split the laser pulses into pairs whose time delay can be set in a range for -100 fs to 100 fs with a resolution of 40 as. The pulses are separated using a 1.5 mm thick beam splitter into two orthogonal beam paths incorporating two retro reflectors [see Fig. 3.2(a)]. The reflector in one arm is mounted on a piezo actuator and the time delay is changed by varying the length of the beam path. The pulse pair is recombined to the same beam using a second beam splitter. The latter one is rotated by 180° in order to provide the same amount of dispersive material for both pulses [95].

The Michelson interferometer is actively stabilized by a He-Ne laser in a Pancharatnam configuration [96]. Its light is linearly polarized and passes the interferometer slightly below the pulses. In one arm of the interferometer a $\lambda/2$-waveplate rotates the polarization of the He-Ne light by 90°. After recombination of the two He-Ne beams behind the interferometer, the light is guided through a different part of the experiment which incorporates a $\lambda/4$-waveplate. Here the linearly polarized light is converted to circularly polarized light. Since the beams of the He-Ne in the two interferometer arms have orthogonal linear polarization, they are converted to light with left and right circular polarization by the $\lambda/4$-waveplate. In combination, left and right circularly polarized light add up to linear polarized light again. However, it can be shown that the polarization angle of the light depends on the phase delay between the separate beams in the two interferometer arms [96, 97]. The linear polarized light subsequently passes a linear sheet polarizer which serves as an analyzer of the polarization angle. Afterwards the transmitted intensity is detected with a photodiode. Any relative changes in the length of the two interferometer arms lead to a rotation of the polarization angle behind the $\lambda/4$-waveplate and subsequently to an intensity change behind the polarization analyzer. This intensity change is fed back via a PID to the piezo actuator which changes the path length in one interferometer arm until the previous intensity is obtained at the photodiode. By rotating the polarization analyzer an artificial intensity variation is imposed which is traced back by the stabilization to the piezo actuator and leads to

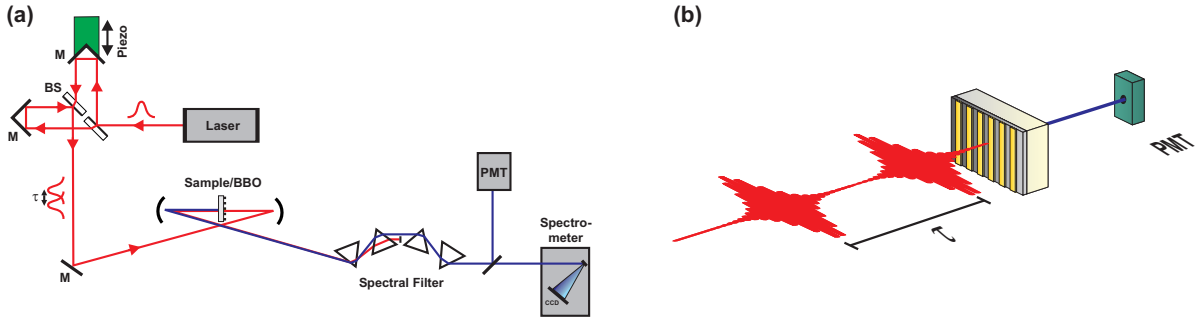

Figure 3.2.: (a) Schematic of the experimental setup. The pulse pairs are generated in a stabilized Michelson interferometer and focused with a spherical mirror onto the sample. The nonlinear signal is separated from the fundamental light using a prism sequence and detected either with a photomultiplier or a spectrometer. (b) The light incidence is normal to the sample with the polarization perpendicular to the gold wires in order to excite the PPP.

a continuous variation of the path length and subsequently a variation of the temporal delay between the laser pulses.

After the preparation of the two pulses, the light is guided to the sample. The pulses are focused onto the sample using a spherical mirror ($f = 101.6$ mm). With a knife-edge technique the diameter of the focus is determined to 30 μm. Hence, it is large enough to excite an appropriate amount of gold wires on the sample but still smaller than the gold wire gratings which have a footprint of 100×100 μm^2. The divergence angle is calculated to $\approx 1°$. Therefore it can be expected that the antisymmetric waveguide mode of the metallic photonic crystal structures is only slightly excited.

Meanwhile the setup has been equipped with a second beam path. Here the light is focused onto the sample with a Cassegrain reflective objective. The focal spot size is reduced below 1.5 μm which enables the investigation of single plasmonic structures in the future [33].

Due to the focusing of the light onto the sample, high pulse intensities are achieved which lead to sufficient nonlinear optical effects in the samples. In order to provide propagation for third-harmonic light at 260 nm, only quartz optics are used behind the sample. The fundamental and the higher harmonic light are further re-collimated with a second spherical mirror. In order to filter the weaker high harmonic signal out of the intense fundamental light, a prism sequence consisting of four similar fused silica prisms is used which spatially separates the spectral components. By inserting a beam block behind the second prism, the high harmonic light is isolated. Since the next two prism reverse the beam paths, it is still possible to align the remaining setup with the intense fundamental light after removing the beam block. For the detection of the high harmonic light, a photomultiplier tube (PMT) (*Hamamatsu IP28*) is used which has an optimized

conversion efficiency in the UV regime. For spectrally resolved measurements, a grating monochromator (*Roper Scientific, Spectra Pro*) with a subsequent liquid-nitrogen-cooled and UV-enhanced charge coupled device (CCD) camera is utilized.

3.1.3. Experimental results

In order to prepare the experimental setup for ACF measurements, the Michelson interferometer has to be calibrated and the $\tau = 0$ delay has to be found. Behind the interferometer, the pulses are focused onto the BBO crystal and the intensity of the second-harmonic light is detected. By rotating the polarization analyzer of the stabilization part, the temporal delay is varied and the $\tau = 0$ position is reached at maximum SHG intensity. To verify the alignment of the experimental setup it is advantageous to measure a nonlinear autocorrelation function and analyze its symmetry with respect to $\tau = 0$. It turns out that a proper collinearity and a perfect spatial overlap of the beams on the sample is crucial in order to achieve a symmetric ACF.

In the following, only third-harmonic ACF are discussed since the 1D metallic photonic crystal structures generate no second-harmonic light (compare chapter 4). In order to obtain a reference ACF, in the first step a thin layer of indium tin oxide (ITO) (thickness d = 140 nm) on top of a quartz substrate is used as the nonlinear medium. This material turns out to be ideal for efficient THG. The two pulses from the Michelson interferometer are focused onto the ITO layer and the third-harmonic light is measured using the PMT [see Fig. 3.2(b)]. The polarization analyzer of the interferometer stabilization is first rotated until the largest delay τ is reached. Then the analyzer is rotated in steps which reduces the delay and the THG intensity is measured for each step. For THG the intensity as a function of τ can be written as

$$I_{ACF,3}(\tau) \propto \int^{T_R} \left[|E(t) + E(t+\tau)|^3\right]^2 dt. \tag{3.4}$$

Fig. 3.3(a) shows the measured autocorrelation function. It is perfectly symmetric with respect to $\tau = 0$ and shows an intensity ration of 32:1 between $\tau = 0$ and $\tau >> 0$ [92]. Similar to the second-harmonic ACF, side lobes are visible in the ACF envelope around $\pm$ 40 fs which result from the satellite pulses. Due to the dependence of the intensity on the third order of the electric field, the main intensity peak is much higher and the side lobes are less pronounced.

If a metallic photonic crystal structure is used instead of the ITO layer, the third-harmonic ACF has a completely different shape. Figure 3.4 shows the linear optical response of the structure where the two WPP resonances can be identified. Figure 3.3(b) is the related nonlinear ACF which is measured at the sample. At first the ACF is much broader than the ACF of the ITO layer. Even for large delay times, where the pulses no longer overlap temporally, a rather large THG signal can be observed. The second

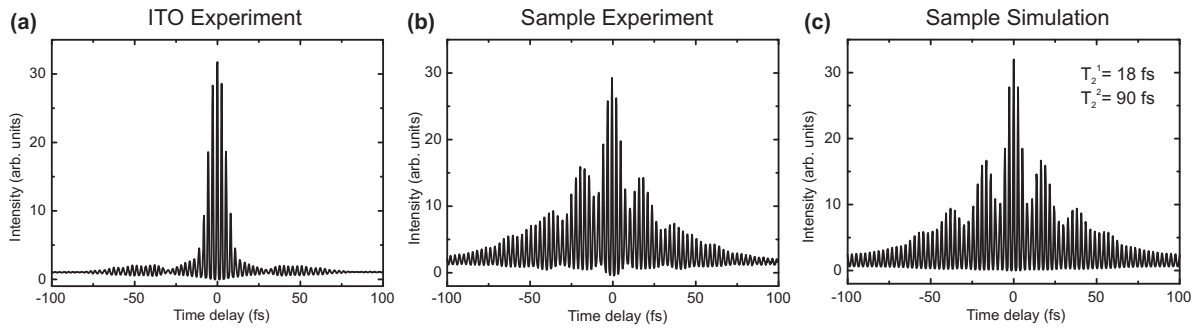

Figure 3.3.: (a) Third-harmonic autocorrelation function of an ITO layer. (b) Experimental data using a metallic photonic crystal structure as the nonlinear medium. (c) Simulations using the harmonic oscillator model with dephasing times of 18 fs and 90 fs for the two polariton branches, respectively.

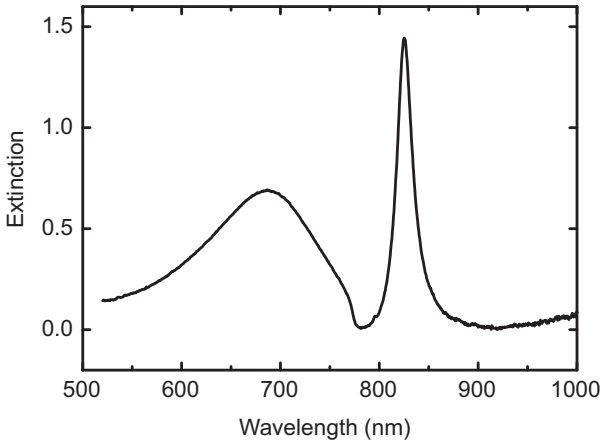

Figure 3.4.: Extinction spectrum of a metallic photonic crystal structure, which is used for the ACF measurements, showing a broad and a narrow WPP resonance.

difference is a beating of the ACF envelope with a period of ≈ 20 fs. Since the laser pulses are the same, the changes in the shape of the ACF have to originate from the plasmonic system. It can be found furthermore that the shape of the ACF varies for different structure geometries and different linear optical responses of the systems [38, 92, 98]. In the next section the harmonic oscillator model is utilized once more in order to retrieve the temporal dynamics of the plasmonic system from the shape of the nonlinear ACF.

This experimental technique has first been presented by Lamprecht *et al.* in order to study the dephasing of pure PPP [37,52]. A few years later, Zentgraf and Klein utilized the method for metallic photonic crystal structures where the ultrafast dynamics of the WPP modes were investigated [38,40]. In the meantime more complicated metallic photonic crystal structures incorporating a plasmonic superlattice were studied as well [98]. Recently, Hanke *et al.* showed that it is even possible to utilize the method for single plasmonic nanoantenna structures [99].

3.1.4. Harmonic oscillator model

For the theoretical description of the nonlinear ACF in Eq. 3.3 and 3.4 it was assumed that the response of the nonlinear crystal is instantaneous and that no coherence remains in the system after the pulses. Therefore the shape of the nonlinear ACF is directly related to the shape of the laser pulses. However, if the response of the nonlinear medium is not instantaneous and the medium maintains a material polarization after the excitation by the laser pulses, the shape of the ACF should change as well. If the shape of the laser pulse is known beforehand, all variations of the ACF have to originate from the nonlinear medium and it is possible to extract its optical response.

For metallic photonic crystals it has been shown in chapter 2 that pronounced resonances are found in the linear extinction spectra. These resonances already indicate that the optical response is not instantaneous and that a material polarization is still present in the sample after the excitation.

In the following, a basic model is developed to account for the variations in the shape of the ACF. Here, the WPP modes are described as damped harmonic oscillators [37, 38, 52]. Finally, by fitting the theoretically obtained ACF to the experimental one, the dephasing times of the WPP modes are retrieved. To simplify the model in a first step, a system which provides solely PPPs is considered *and the PPP resonance is described as a harmonic oscillator*. Just like in Eq. 2.14 the differential equation for the displacement of the electrons is given by

$$\ddot{x}(t) + 2\gamma\dot{x}(t) + \omega_0^2 x(t) = -\frac{e}{m_e}E(t), \tag{3.5}$$

where m_e is the electron mass and γ is the damping constant which is related to the dephasing time $T_2 = 1/\gamma$. The solution of this equation reads

$$x(t) \propto \int_{-\infty}^{t} E(t')e^{-\gamma(t-t')} sin\left[\omega_0'(t-t')\right] dt' \qquad \text{with} \qquad \omega_0' = \sqrt{\omega_0^2 - \gamma^2}. \tag{3.6}$$

The equations for the polariton polarization

$$P^{pl}(t) = -N \cdot e \cdot x(t) \qquad \text{and} \qquad P^{pl}(t) = N \cdot \alpha \cdot E_{pl}(t) \tag{3.7}$$

connect the displacement $x(t)$ with the local plasmon field E_{pl} in the vicinity of the structure. Here, α is the polarizibility and N the number of oscillators. Taking the total electric field of the two pulses into account (Eq. 3.1), the local plasmon field is given by

$$E^{pl}(t,\tau) \propto \int_{-\infty}^{t} E_{tot}(t',\tau)e^{-\gamma(t-t')} \sin\left[\omega_0'(t-t')\right]dt', \tag{3.8}$$

which incorporates the external light field as well as the plasmon field. Here, the external light field $E(t)$ is deduced from the measured laser spectrum by a Fourier transformation.

The expression contains an exponential damping term with the damping constant γ, which describes the decay of the PPP oscillation, and an oscillating term.

In the case of the coupled system where the PPP is hybridized with the waveguide mode, two resonances, which are related to the eigenmodes of the WPP, appear in the spectrum. They can as well be described as individual harmonic oscillators. Therefore Eq. 3.8 is easily expanded to several oscillators. Now the local polariton field is given by

$$E^{WPP}(t,\tau) \propto \int_{-\infty}^{t} \sum_j E_{tot}(t',\tau) A_j e^{-\gamma_j (t-t')} \sin\left[\omega_j'(t-t')\right] dt', \tag{3.9}$$

where $j = 1, 2$. Each WPP branch is characterized by an amplitude A_j, a resonance frequency ω_j, and a damping constant γ_i which will later on serve as fit parameters. In the third-harmonic regime, the local polariton field leads to a nonlinear polarization $P^{(3)}_{WPP}(t,\tau)$, which is the source of the nonlinear signal:

$$I_{THG}(t,\tau) \propto [P^{(3)}_{WPP}(t,\tau)]^2 \propto \left[(E_{WPP}(t,\tau))^3\right]^2. \tag{3.10}$$

Finally, the ACF can be calculated as

$$I_{THG}(\tau) \propto \int^{T_D} \left[|E_{WPP}(t,\tau)|^3\right]^2 dt \tag{3.11}$$

$$\propto \int^{T_D} \left[\int_{-\infty}^{t} \sum_j E_{tot}(t',\tau) A_j e^{-\gamma_j (t-t')} \sin\left[\omega_j'(t-t')\right] dt' \right]^6 dt. \tag{3.12}$$

Fig. 3.3(c) shows an ACF which is calculated from the harmonic oscillator model. The fit parameters A_i, T_2^i, and γ_i have been chosen in a way that the measured ACF [Fig. 3.3(b)] is ideally reproduced. For this sample the fit parameters are:

$$\begin{array}{lll} A_1 = 1, & T_2^1 = 18fs, & \lambda_1 = 710nm, \\ A_2 = 0.333, & T_2^2 = 90fs, & \lambda_2 = 810nm. \end{array}$$

The calculated ACF shows the same features as the measured one. It is much broader than the ACF from the ITO sample and the beating of the envelope is reproduced as well. Since the electric field of the laser pulses enters in the simulation, its influence to the shape of the ACF is already inherent. From the simulations, the dephasing time of the narrow WPP mode at 810 nm is determined to be 90 fs which is one order of magnitude larger as the dephasing times of pure PPP. This result shows that the hybridization of the PPP with photonic waveguide modes does not tailor the linear optical spectra alone but changes the temporal dephasing dynamics of the system as well. The dephasing time of the broad wavelength WPP mode at 710 nm is found to be 18 fs.

The simulations help as well to understand the beating of the ACF envelope. It is a result of the simultaneous excitation of both WPP modes with the broad laser spectrum and the spectral splitting of the WPP modes is in good agreement with the beating period. Since many fit parameters are necessary to reproduce the measured ACF, the retrieved parameters can only be determined with an uncertainty of approximately 10%.

It is worthwhile to note that it is not the PPP dephasing time which is prolonged by the hybridization. Rather the eigenmodes of the coupled WPP system can have longer dephasing times than a pure PPP. The upper limit for the dephasing time of the WPP eigenmodes is certainly determined by the dephasing time of the pure waveguide mode in the slab. The more photonic character is present in the WPP mode, the longer is the dephasing time. It will turn out that the nonlinear optical effects in metallic photonic crystals are predominantly a consequence of the plasmonic character of the WPP modes. Therefore, when designing appropriate metallic photonic crystals for the coherent control experiments in chapter 5, one will always have to deal with a trade-off between long dephasing times on the one hand and sufficient plasmonic character of the mode on the other hand.

3.1.5. Spectrally resolved autocorrelation

A deeper understanding of the ACF shape is achieved if the nonlinear signal is spectrally resolved. In the experiment, for each time delay of the two pulses, the THG light is detected using the spectrometer, and a 2D spectrally resolved ACF is obtained. Figure 3.5 shows a typical spectrally resolved ACF. Several spectral components are visible which have different temporal evolution. For example the beating in the spectrally integrated ACF does not appear in the whole THG spectrum. The spectral component at 265 nm is strongly modulated by a beating while the component at 272 nm decreases monotonously. In previous work it has been found that the spectral components are due to THG of the individual WPP modes ($3\omega_1$ and $3\omega_2$) as well as sum-frequency generation (SFG) of both modes ($2\omega_1 + \omega_2$ and $2\omega_2 + \omega_1$) in the third-order regime [40, 98]. It can be shown that only the components from SFG incorporate the beating because both WPP modes are involved. The amplitude of the four nonlinear components mainly depends on the convolution of the laser spectrum and the linear optical response of the sample.

By using the right set of fit parameters the spectrally resolved ACF can as well be calculated from the harmonic oscillator model. However, so far the harmonic oscillator model does not provide additional information about the WPP system. All information, especially the dephasing time of the WPP modes, could be retrieved as well from the linear optical spectrum alone. For a full understanding of the optical response of metallic photonic crystals it would be important to determine the dispersive part of the dielectric function, i.e., the spectral phase change which is introduced by the sample, addition-

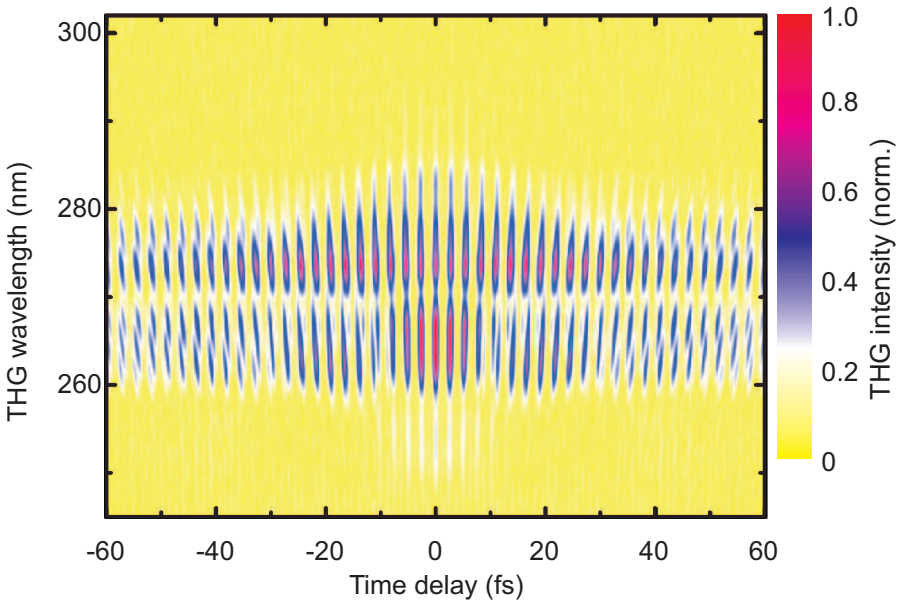

Figure 3.5.: Spectrally resolved THG autocorrelation function measured of a metallic photonic crystal. One can see mainly two spectral components (at 265 nm and 272 nm) with a completely different temporal behavior.

ally. This information is already inherent in the spectrally resolved ACF but cannot be retrieved using the harmonic oscillator model. In section 3.2 a different approach is presented in order to retrieve the phase information as well from the spectrally resolved ACF. It is based on frequency-resolved optical gating (FROG) which is another method for the characterization of ultrashort laser pulses.

3.1.6. Dephasing of optical magnetism

The spectrally resolved ACF technique is as well used to investigate the ultrafast dynamics of more complex plasmonic structures such as metallic photonic crystal superlattices [92, 98]. The example which is discussed here is a magnetic photonic crystal [100–102]. The unit cell of the structure consists of two plasmonic wires on top of each other with a dielectric spacer layer inbetween. Fig. 3.6(a) shows a transmission electron micrograph of one wire pair which has been obtained by cutting a slice of the magnetic photonic crystal with a focused ion beam. One can clearly distinguish the gold wires from the 25 nm thick dielectric MgF_2 layer. The structure was fabricated in the same way as the metallic photonic crystals (see chapter 2.4) by evaporating gold, MgF_2, and gold in a series before the lift-off. The process leads to a trapezoidal shape of the wire pair where the width of the upper wire is slightly smaller than the width of the lower one.

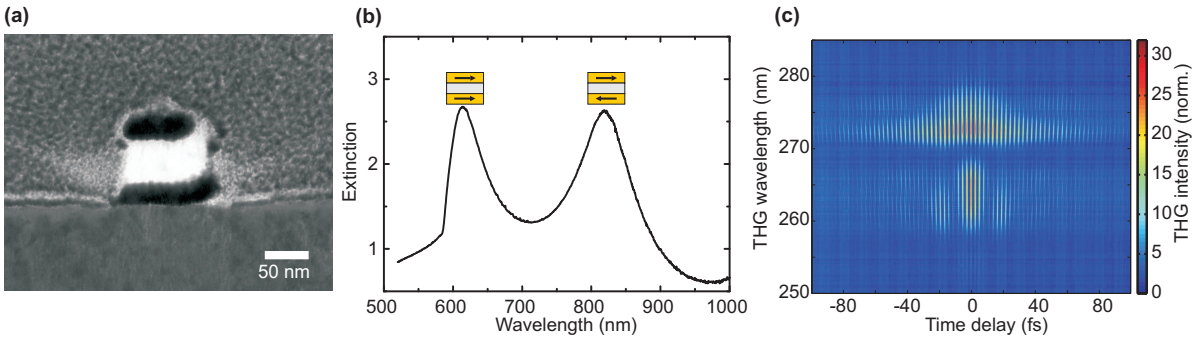

Figure 3.6.: (a) Transmission electron micrograph of a magnetic photonic crystal consisting of two gold wires with a dielectric spacer inbetween. (b) The individual PPP in the wires oscillate in phase or out of phase leading to two resonances in the extinction spectrum. (c) Spectrally resolved THG autocorrelation of a magnetic photonic crystal hybridized with a photonic waveguide mode.

Since PPPs can be excited in both wires simultaneously, the two individual PPP hybridize to a symmetric and an antisymmetric mode. In contrast to the horizontal coupling in Fig. 2.4(c), the antisymmetric mode is lowered in energy in the linear extinction spectrum and therefore at larger wavelength than the symmetric mode [Fig. 3.6(b)]. The antisymmetric mode is of special interest. Since the upper wire has the opposite charge distribution compared to the lower wire, a ring current can be identified. From electrodynamics it is known that a ring current leads to an orthogonal magnetic moment which is located here in the dielectric spacer layer. Since the charge distribution is oscillating at optical frequencies, the magnetic moment also flips sign accordingly. Therefore the antisymmetric mode is also called magnetic mode. The appearance of magnetic moments in photonic structures is a new paradigm in optics and has been extensively investigated in optical metamaterials [103–105].

In magnetic photonic crystals, the magnetic mode is coupled and hybridized with photonic waveguide modes such as the PPP modes in metallic photonic crystal [100]. Thus the dephasing time of the magnetic polariton modes can be tailored as well by varying the grating geometry. Spectrally resolved ACF of magnetic photonic crystals have been measured to determine the dephasing times. Figure 3.6(c) shows a spectrally resolved ACF of a magnetic photonic crystals. Again dephasing times of up to 80 fs were obtained. In the future these structures could be utilized for further magnetooptical effects. Therefore the MgF_2 spacer layer would be replaced by a magnetoactive material. Due to the long dephasing times of the hybrid magnetic modes, strong magnetooptical effects such as Faraday or Kerr rotation could be achieved.

3.2. Interferometric frequency-resolved optical gating

The spectrally resolved ACF technique together with the harmonic oscillator model is a powerful tool to investigate the ultrafast temporal dynamics of hybrid plasmonic systems. However, it is not possible to obtain the full optical response information of the structures by using this method. As for every absorbing material not only the amplitude of the transmitted light is modulated by the sample but also the spectral phase. The dispersive part of the dielectric function of the structure, which modulates the spectral phase of the light is an important measure in order to determine parameters like the group refractive index or the group velocity of light in the system. It will be shown in the next chapter how the group index can for example influence the nonlinear optical responses of a plasmonic structure. Thus, for further experiments and applications, the knowledge of the absorptive *and* dispersive part of the dielectric function is mandatory.

With the help of the harmonic oscillator model it is not possible to retrieve the phase information. However, this information is already inherent in the spectrally resolved ACF traces. Therefore a method has to be found in order to extract the phase information from it. For this problem, methods from laser pulse characterization can be utilized again. It has been shown before that a nonlinear ACF already provides certain phase information of ultrashort laser pulses. In 1993 an advanced pulse characterization method has been presented which is called frequency-resolved optical gating (FROG) [106]. This technique will be the basis in order to obtain the complete optical response of metallic photonic crystals. It is explained shortly in the following section.

3.2.1. Pulse characterization using FROG

Since the first experiments by Trebino *et al.*, several examples of FROG have been presented. Among others SHG FROG [107], THG FROG [108], or transient grating FROG [109] should be mentioned. In this section SHG FROG is used to explain the basic principles. Especially for the phase retrieval algorithm there are no big differences among the methods.

In the SHG FROG experiment, a pair of unknown but identical laser pulses is generated in separate beams and spatially overlapped in a nonlinear crystal [see Fig. 3.7(a)]. One of the pulses experiences a variable time delay τ such as in an ACF measurement. Due to the oblique incidence of the laser pulses, there is only a SHG signal in the normal direction of the nonlinear crystal if the pulses overlap temporally. This SHG signal is detected with a spectrometer as a function of the time delay and one obtains a symmetric FROG trace such as it is shown in Fig. 3.8(b).

In the next step the FROG trace is processed using a FROG retrieval algorithm. The

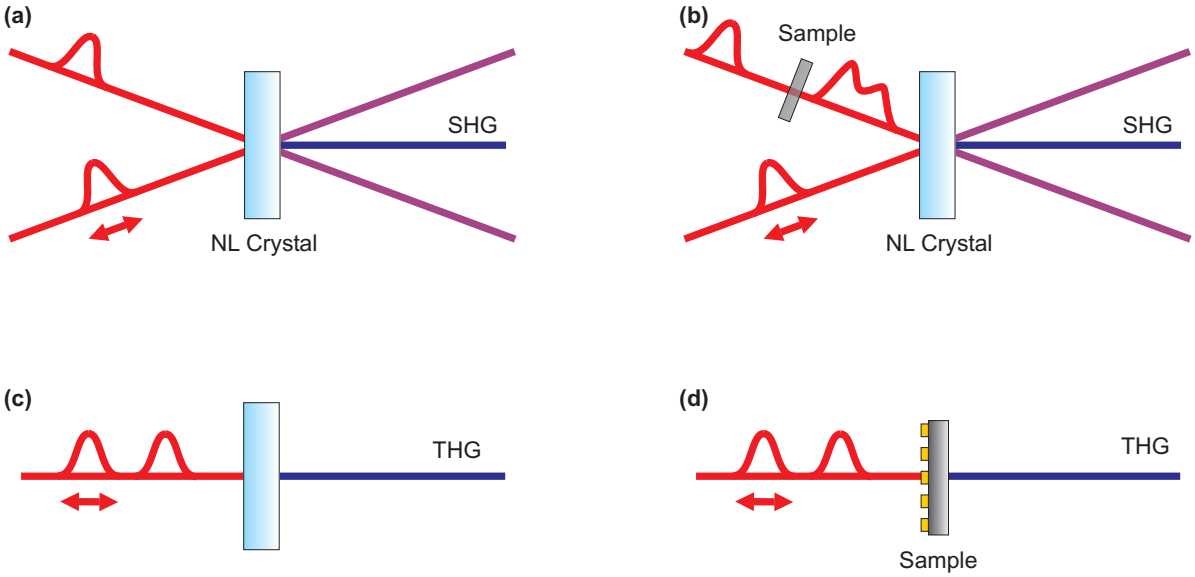

Figure 3.7.: Experimental configurations for (a) SHG FROG and (b) XFROG. (c) Interferometric FROG configuration for the characterization of laser pulses. (d) The metallic photonic crystal structure serves as the nonlinear medium.

FROG trace is first subdivided in a square grid with a size of $N \times N$ grid points. Following that, the algorithm starts with an initial guess for the electric field $E_{sig}(t, \tau)$ of the pulses and iteratively improves it until the ideal shape of the electric field is found. During the iteration two constraints have to be fulfilled. The first one is the nonlinear constraint

$$E_{sig}(t, \tau) = E(t)E(t + \tau). \tag{3.13}$$

The second one is the data constraint

$$I_{FROG}(\omega, \tau) = \left| \int_{-\infty}^{\infty} E_{sig}(t, \tau) e^{-i\omega t} dt \right|^2 . \tag{3.14}$$

It can be shown that the algorithm converges since the FROG trace is a 2D plot. Nevertheless the experimental FROG trace will always contain errors and noise, therefore ideal convergence will never be reached. To determine a measure for the quality of the convergence, a FROG error G is calculated:

$$G = \left[\frac{1}{N^2} \sum_{i,j=1}^{N} \left(I_{FROG}(\omega_i, \tau_j) - |E_{sig}(\omega_i, \tau_j)|^2 \right)^2 \right]^{\frac{1}{2}} . \tag{3.15}$$

If the FROG error is below a certain value, convergence is assumed to be reached. For example, for a grid size of 64×64 the FROG error has to be below $G < 0.005$ in order to achieve convergence [110]. Finally, the FROG algorithm delivers the complex value

of the electric field, i.e., amplitude and phase information. One important requirement in order to achieve small FROG errors is a perfect symmetry of the FROG trace with respect to $\tau = 0$. Therefore, a proper spatial overlap of the two beams on the nonlinear medium has to be guaranteed.

A few years after the development of FROG, a variation of this technique has been utilized in order to retrieve the complete optical response which is imposed by a photonic material [111]. The experimental configuration of this cross-correlation FROG (XFROG) technique is shown in Fig. 3.7(b). One of the laser pulses passes the unknown material an is modulated by its linear optical response. The resulting laser pulse is overlapped again with the undisturbed one in the nonlinear crystal and a XFROG trace is recorded. If the electric field of the pulses is completely known, all variations of the XFORG trace originate from the linear optical response of the sample and can finally be retrieved.

3.2.2. Phase retrieval from interferometric FROG traces

Unfortunately, non-collinear FROG and XFROG experiments have one disadvantage. If the spectral phase is to be retrieved over a broad spectral range, either the laser has to be tuned step by step or broad-band excitation has to be used. In the latter case it is very challenging to achieve complete phase matching in the nonlinear crystal over the full spectral range. This problem can be solved by changing the setup to a collinear configuration where both pulses follow the same beam path [see Fig. 3.7(c)]. The ITO layer is used as the nonlinear medium and the signal at the third harmonic is detected. Like the spectrally resolved ACF in Fig. 3.5, the interferometric FROG trace of an unknown laser pulse is now dominated by an interference fringe pattern 3.8(a). In the following, only third-order nonlinearities are considered. Due to the additional interference information, the retrieval algorithm cannot handle these traces. Therefore the interferometric FROG trace has to be reduced to the conventional FROG trace. One way to achieve this has been demonstrated in two individual publications [112, 113].

In the first step, the interferometric FROG trace is Fourier-transformed with respect to the time delay axis. The result is a trace with delay frequency components at multiples of ω_0, $2\omega_0$, and $3\omega_0$, where ω_0 is the laser center frequency. Additionally there is a DC component which contains the desired FROG information. By applying a multiple Gaussian filter function around the DC component, the other frequency components are suppressed. After a back-transformation and subtracting a delay-independent background, the fundamental FROG trace is found [see Fig. 3.8(b)] and can be easily processed using the retrieval algorithm. Fig. 3.8(c) shows the retrieved spectrum of the laser together with its spectral phase. The agreement with the measured spectrum is quite good although the FROG-error is 0.085 (N = 64) and therefore still a little bit too large. Due to the complicated spectrum, convergence has not been achieved completely. The temporal evolution is shown in Fig. 3.8(d). The satellite pulse, which was already

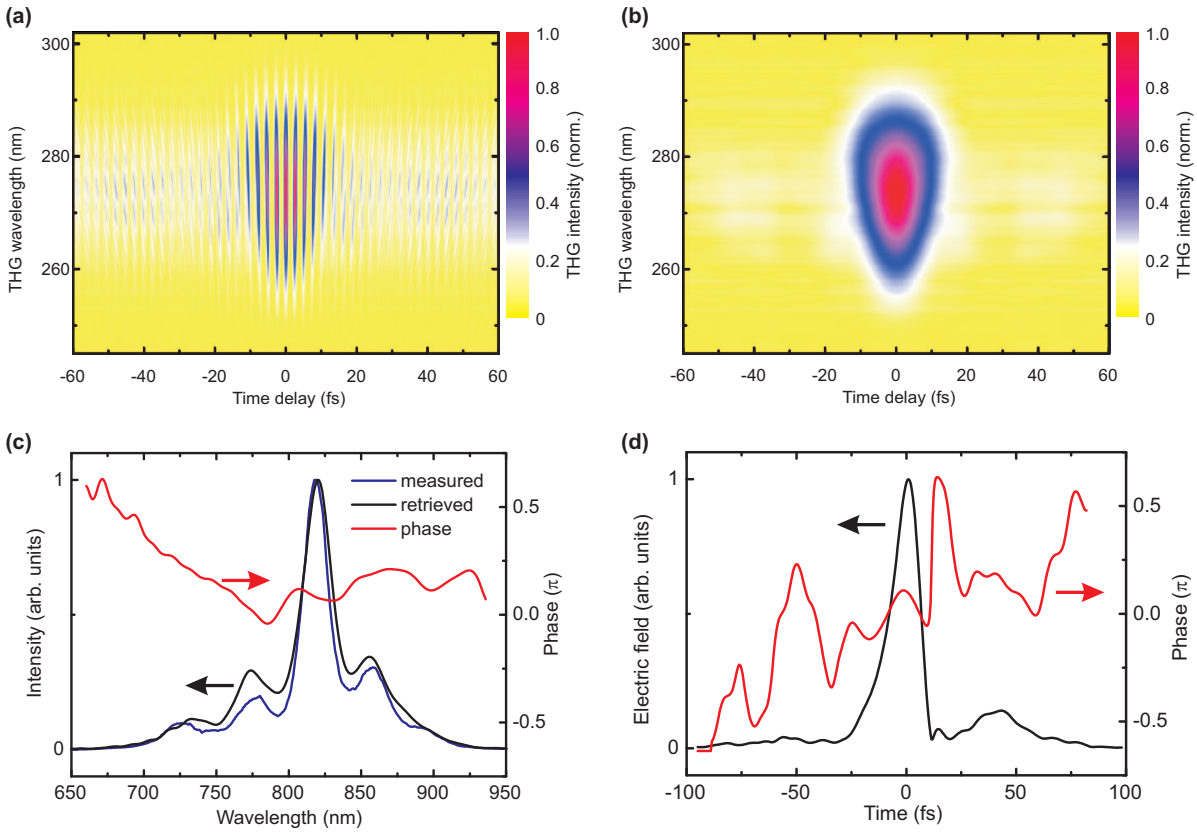

Figure 3.8.: (a) Interferometric FROG trace measured at an ITO layer. (b) FROG trace after Fourier-filtering. (c) Laser spectrum together with the spectral phase. (d) Electric field of the laser pulses in the time domain showing the satellite pulses around 40 fs.

predicted from the ACF measurements, can clearly be identified about 40 fs after the main pulse.

Since the standard FROG trace can be extracted from the interferometric FROG trace, it should be possible as well to do a collinear XFROG-like experiment in order to obtain the phase information of a metallic photonic crystal structure. In 2010 Anderson *et al.* have presented this method for plasmonic excitations in a metallic tip [114]. The tip was illuminated with a collinear pulse pair, served as the nonlinear medium, and the interferometric FROG trace was measured after characterizing the laser pulses. Subsequently, the FROG trace was extracted from the interferometric trace using Fourier-filtering. After the retrieval, the complex electric field $P(\omega)$ was obtained. $P(\omega)$ incorporates the electric field $E(\omega)$ of the laser pulses together with the response function $R(\omega)$ of the plasmonic structure:

$$P(\omega) = R(\omega) \cdot E(\omega). \tag{3.16}$$

If $E(\omega)$ is known, $R(\omega)$ can easily be calculated in the frequency domain. Anderson *et al.* demonstrated a very nice agreement of the retrieved amplitude and phase of the plasmonic structure compared to simulations.

In the following this method is utilized for metallic photonic crystals with two WPP resonances in the spectrum. For metallic photonic crystals, XFROG measurements have already been performed in the past to retrieve phase information [115]. However, up to now it was only possible for rather narrow band laser excitation. Thus, the spectral phase was only retrieved for TE polarization in the narrow spectral window of the waveguide mode. For TM polarization a broad-band laser has to be chosen which makes XFROG experiments extremely challenging in a non-collinear configuration. However in a collinear configuration, many problems can be circumvented.

In contrast to the interferometric FROG measurements, the metallic photonic crystal structure itself acts as the nonlinear medium [see Fig. 3.7(d)]. The spectrally resolved ACF trace (see Fig. 3.5) can already be used for the retrieval. The interference fringes are removed using Fourier filtering and the standard FROG trace is extracted. By using the FROG retrieval algorithm, $P(\omega)$ is found and $R(\omega)$ can be calculated since $E(\omega)$ has already been determined before (see Fig. 3.8). For the retrieval of the trace in Fig. 3.5, the minimum FROG error $G = 0.011$ has been achieved which is even higher than the error which was obtained in retrieving $E(\omega)$. Additionally to the complicated laser spectrum, the optical response of the metallic photonic crystal leads to a more detailed FROG trace and thus a larger FROG error.

Figure 3.9(a) shows the amplitude and phase of the response function for the metallic photonic crystal structure. The amplitude of the response function fits well to the measured extinction. Especially the long wavelength WPP mode, which is around 830 nm in the present case, is well reproduced. Major disagreements are only found at the edges of the spectrum. Here the amplitude of the laser spectrum is rather low and an exact

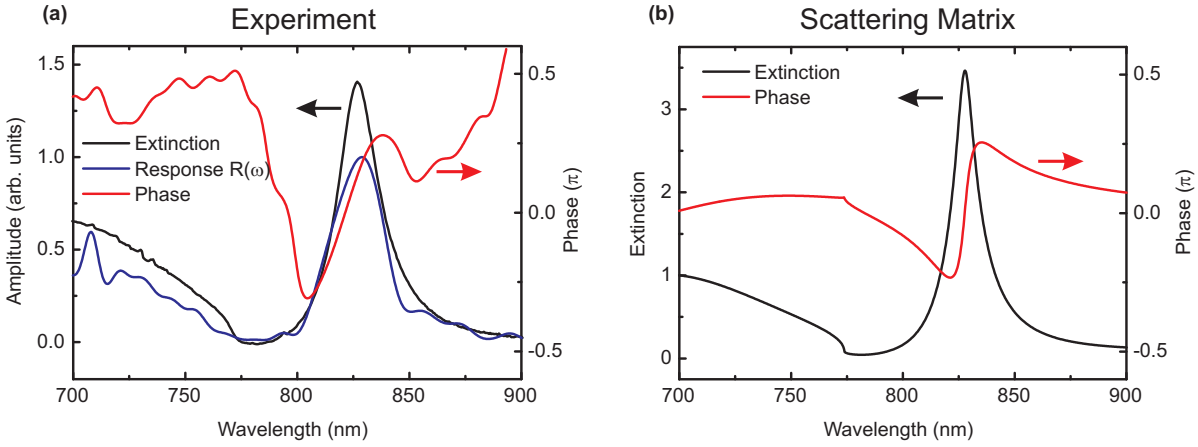

Figure 3.9.: (a) Amplitude and phase of the response function retrieved from the interferometric FROG trace of a metallic photonic crystal. Also shown is the extinction measured with the white light transmission setup. (b) Extinction and phase calculated with the scattering matrix method.

retrieval is hardly possible. In order to get a feeling for the retrieved spectral phase, scattering matrix simulations were performed which also deliver spectral phase information [see Fig. 3.9(b)]. In comparison to the theoretical results, the retrieved spectral phase shows the main features such as the inflection points in spite of the large FROG errors. Especially around the long wavelength WPP mode even the absolute value of the phase is in good agreement with the simulations and major differences are mainly found at the edges of the spectrum.

Finally, it has been shown that additional information can be obtained from the spectrally resolved ACF which was not possible with the harmonic oscillator model before. Using the interferometric FROG retrieval, the optical response of metallic photonic crystal structures can be characterized completely in amplitude and phase over a broad spectral range. By using laser pulses with a less complicated spectral shape, the quality could be improved further in the future. Nevertheless, this method still relies on one assumption: No spectral or temporal shape of the nonlinear susceptibility $\chi^{(3)}$ has been assumed so far. Since the metallic photonic crystal structure is used as the system to be investigated and as the nonlinear medium simultaneously, the method is not sensitive to complicated nonlinear responses. All spectral dependencies of $\chi^{(3)}$ would result in a wrong interpretation of the linear optical response. However, since the agreement between experimental data and simulations is rather good, the assumption of a spectrally flat nonlinear susceptibility seems to be reasonable. Providing excellent laser pulses with Gaussian spectral shapes is a prerequisite for future experiments. They can be obtained by using amplitude and phase 4-f pulse shapers. In the following chapter the nonlinear response of metallic photonic crystal structures will be discussed in more detail. It will be shown that each constituent material of the structures shows a rather different nonlinear response.

4. Nonlinear response of plasmonic nanostructures

4.1. Introduction to nonlinear optics

So far, the linear optical properties of plasmonic nanostructures were discussed predominantly. With linear optical experiments properties of the structures such as absorption or transmission can be characterized. In linear optical experiments the impinging light intensity is rather weak and has no influence on the optical response of the structure. However, especially in ultrafast experiments like in the previous chapter, extremely short laser pulses are used which possess very high peak intensities up to 100 kW. Additionally, the field localization around the plasmonic nanostructures and the associated field enhancement can lead to even larger intensities. In the nonlinear ACF experiments additional light frequencies are generated at higher harmonics of the fundamental light. In the following, the origin of these nonlinearities together with the generation of higher harmonics is discussed in more detail.

In the linear optical regime, the light-matter interaction is described by the Lorentz oscillator model. The motion of an electron in the material upon excitation by an external electromagnetic field is given by

$$\ddot{x} + \omega_0^2 x = -\frac{e}{m_e} E(t), \tag{4.1}$$

where $x(t)$ is the displacement of the electron. Similar to a harmonic oscillator in classical mechanics (compare Eq. 2.12) the electron experiences an elastic linear restoring force which is associated with a quadratic potential $V(x) \propto x^2$. The material polarization, which is proportional to the displacement of the electron (Eq. 3.7), has a linear relation to the external electric field $\mathbf{E}(\omega, t)$

$$\mathbf{P} = \epsilon_0 \chi^{(1)} \mathbf{E} \tag{4.2}$$

Here ϵ_0 is the vacuum permittivity and $\chi^{(1)}$ is the susceptibility tensor which carries the information about the linear optical properties of the material. The susceptibility $\chi^{(1)}$ is directly related to the refractive index n as $n^2 = 1 + \chi^{(1)}$. The material polarization itself can further be the source of an electric field oscillating at the same frequency ω.

The linear relation between the displacement of the electron and the material polarization is only valid for weak excitation. If the intensity of the exciting electromagnetic field is high, the displacement of the electron is very large and it experiences anharmonicities of the potential $V(x)$. Thus, $V(x)$ can no longer be approximated by a quadratic function. Therefore also the linear relation between the displacement and the material polarization is no longer valid. For this case $\mathbf{P}$ is expanded in a Taylor series:

$$\mathbf{P} = \epsilon_0 \chi^{(1)} \mathbf{E} + \epsilon_0 \chi^{(2)} \mathbf{EE} + \epsilon_0 \chi^{(3)} \mathbf{EEE} + \dots . \tag{4.3}$$

The first term is again the linear response of the material. The next higher order terms take the anharmonicities of the potential into account and depend on higher powers of the electric field. They contain further higher order material parameters $(\chi^{(2)}, \chi^{(3)}, \dots)$ which describe the nonlinear properties of the material. The second term in Eq. 4.3 is the first nonlinear term and depends on the square of the electric field. It leads to a nonlinear material polarization which is the source of an additional electric field which oscillates at twice the fundamental frequency. This process is called second harmonic generation (SHG) and is schematically depicted in Fig. 4.1(a). Two photons of the fundamental light are combined in the material and generate one photon at the double frequency. The third term in Eq. 4.3 contains the electric fields to the power of three and leads to an additional electric field at the threefold frequency. This third-order process is called third-harmonic generation [see Fig. 4.1(b)]. In the experiment, not only an electric field at a single frequency can lead to a nonlinear signal but also a combination of different electric fields at different frequencies ω_i can be taken into account. In that case, the nonlinear polarization oscillates at the sum or the difference of the fundamental frequencies [see Fig. 4.1(c)]. In the third-order regime the following frequencies can be found if three electric fields with frequencies ω_1, ω_2, and ω_3 contribute:

$$\begin{aligned} &3\omega_1, \quad 2\omega_1 \pm \omega_2, \quad 2\omega_1 \pm \omega_3, \\ &3\omega_2, \quad 2\omega_2 \pm \omega_1, \quad 2\omega_2 \pm \omega_3, \\ &3\omega_3, \quad 2\omega_3 \pm \omega_1, \quad 2\omega_3 \pm \omega_2, \\ &\qquad\qquad\qquad\quad \omega_1 \pm \omega_2 \pm \omega_3. \end{aligned}$$

For higher order nonlinear processes even more frequency components are present but their amplitudes decrease strongly for common materials and most of them are spectrally far away from the visible spectral range.

The nonlinear susceptibilities $\chi^{(i)} (i = 2, 3, \dots)$ are tensorial quantities and determine the amplitudes of the nonlinear signals. For materials whose microscopic structure is inversion symmetric it can be shown that the even nonlinear susceptibilities are zero on the electric dipole level. Therefore only the odd harmonics are found in the experiment. This is the case for 1D metallic photonic crystals whose grating structure is inversion symmetric. Therefore SHG is negligible and THG is the first nonlinear order that can be detected.

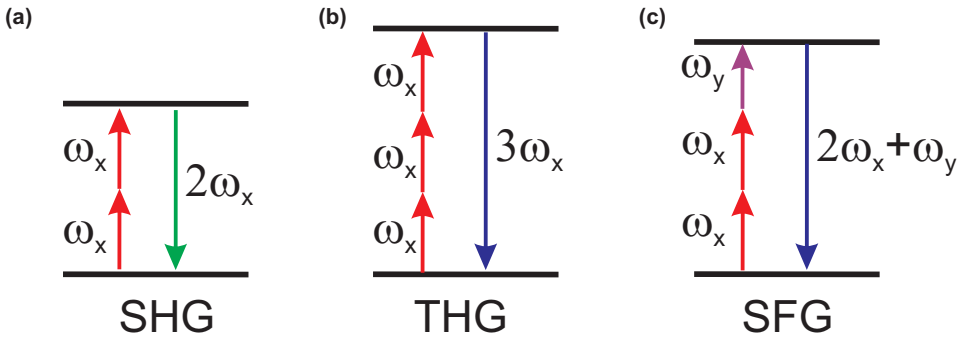

Figure 4.1.: Schemes of nonlinear processes: (a) second-harmonic generation (SHG), (b) third-harmonic generation (THG), and (c) sum-frequency generation (SFG).

In the ultrafast spectroscopy experiments in chapter 3 it has been shown that metallic photonic crystal structures generate a rather large signal at the third harmonic but it was not *a priori* clear where this nonlinearity originates from. In the harmonic oscillator model, the intensity of the THG signal was simply assumed to be proportional to the cube of the linear polariton polarization. No actual values for $\chi^{(3)}$ were assumed so far and the origin of the nonlinearity was not discusses. Thus, the following sections should lead to a deeper understanding of the nonlinear processes in metallic photonic crystals.

4.2. Origin of the nonlinearity in plasmonic structures

The research field of plasmonics has developed tremendously over the last few years and all kind of structures and shapes have been considered for different nanooptical applications. However, the nonlinear responses of plasmonic nanostructures have been investigated only by a few research groups. It has been shown that different structure shapes can be utilized for high harmonic generation and some experiments should be shortly introduced here.

Lippitz *et al.* used colloidal plasmonic nanoparticles to determine the THG intensity as a function of the particle size [see Fig. 4.2(a)] [33]. The particle size ranged from 40 nm to 150 nm and they where excited at 1500 nm. Thus the third-harmonic at 500 nm was resonant to the PPP in the particles. The experiments showed that the THG intensity increases with a third- to fourth-power dependence in particle diameter. From theory it was predicted that the THG intensity should increase with a sixth-power dependence if the nonlinear susceptibility originates from the bound electrons is the particle. In that case, the nonlinear response would be a bulk effect. A fourth-power dependence is found if the free electrons in the particle are considered [116]. Due to the finite

size of the particle the free electrons experience deviations of the harmonic potential at the surface of the particle. Unfortunately, from these experiments it could not finally be clarified whether bulk or surface effects dominate the nonlinear response since the theory of Fomichev *et al.* does not work for particle sizes above 50 nm due to retardation effects. Additional experiments using even smaller particles would help in the future to distinguish the surface from the bulk effect. Recently, preliminary experiments pointing in this direction have been performed [117].

Canfield *et al.* investigated SHG in T-shaped plasmonic dimer structures [see Fig. 4.2(b)] by varying the gap size between the upper horizontal and the lower vertical metal bar [34]. One would expect that a small distance between the metal bars leads to a strong field enhancement in the gap region and subsequently a high SHG signal [118, 119]. The field enhancement in the gap should only be present for vertical incident polarization but not for horizontal polarization. However, the results could not be explained simply by field enhancement. The authors investigated the local field distribution in the vicinity of the nanostructure for both incident polarizations. They rather found for horizontal polarization that the field enhancement is restricted to the boundary of the horizontal particle and concluded SHG to be a surface effect. The horizontal metal bar itself would not lead to a SHG signal because of its centro symmetry. The contributions to the local tensor from the portions of the perimeter possessing opposite surface normals tend to cancel. [120]. Thus, the more symmetric the structure, the less SHG is generated. However, due to the presence of the vertical bar, the local field enhancement becomes disturbed and the asymmetry in the local electric field leads to the SHG signal [121]. For horizontal incident polarization, the strongest fields were not found in, but rather around the cap due to the structural asymmetry. In this case, the asymmetry in the local field distribution helped as well to explain the appearance of SHG.

Besides the nonlinear response of plasmonic nanostructures, optical metamaterials attracted interest in the nonlinear regime as well. Using metamaterials it is in principle possible to tailor the linear optical properties at will. But it has also been predicted that the nonlinearities play an important role [122]. Once the nonlinear response of optical metamaterials is completely understood, it would be even possible to custom-design nonlinear optical materials. Klein *et al.* investigated the SHG and THG response of split ring resonator (SRR) structures [see Fig. 4.2(c)] [36, 123]. Those structures can be regarded as small LC-oscillator circuits at optical frequencies. The open ends of the wires form a capacitance C and the wire itself a coil with one winding and an inductance L. If the incident light is polarized parallel to the gap, the free electrons start to oscillate along the ring leading to a magnetic dipole moment perpendicular to the structure plain [103, 124]. If the incident light was resonant to this magnetic mode, an intense SHG signal was detected. It was much stronger when compared to the orthogonally polarized excitation, where pure PPP resonances are excited in the left and right arm of the SRR. Additionally, the authors compared SHG and THG intensities to plasmonic structures which do not provide a magnetic moment. Here, no nonlinear signal was detected which rules out hot spot effects. From these findings the authors concluded

that the enhancement of the nonlinear signal is strongest for resonant [125] excitation of modes with magnetic dipole character. This effect could qualitatively be explained from Lorentz force considerations [126]. In the meantime this magnetic effect has been utilized to enhance the nonlinear response of crystalline GaAs [127].

Recently, Valev *et al.* investigated a special kind of plasmonic nanostructures which show optical chirality and which therefore respond differently to left and right circularly polarized light. The unit cell of the structure consists of four G-shapes which are rotated with respect to each other in a pre-defined manner [see Fig. 4.2(d)]. The authors found that the chirality of the structure also enters in the nonlinear response. The SHG signal as well showed a chiral behavior. For certain experimental configurations and symmetry considerations the SHG was attributed to higher order plasmonic modes associated with the plasmonic field enhancement of the nanostructure.

The experimental examples show that different origins of the nonlinearity are presently discussed. Although in theoretical approaches effective nonlinear coefficients were determined [128, 129], a full microscopic theory of the nonlinear response in plasmonic nanostructures is still lacking. In theory, the origin of the nonlinearity is as well controversially discussed:

Zeng *et al.* developed a classical electromagnetic theory where the free-electrons is the metal are approximated as a Coulomb-interacting electron gas and their motion upon light excitation is described by the plasma equations [130]. They proposed that their classical model is easy to implement and that no microscopic model is required. The theoretical results of SHG were compared to the experimental data of Klein [36,123] and Canfield [34] and a good agreement was found even when effects of the surface electrons were not taken into consideration. Rather, the overall shape of the nanoparticle was found to play the dominant role. From their model the authors hence concluded that metal bulk effects play the dominant role in SHG of metallic nanostructures and surface effects are negligible in first place.

However a few months later, Wang *et al.* contradicted those findings [131]. Using a two-beam SHG experiment on a metal surface they found a way to separate the bulk from the surface effects. They concluded that surface effects, having an electric dipole origin, dominate the nonlinearity in metallic nanostructures over bulk effects, having magnetic dipole and electric quadrupole origins.

In summary, several origins of the nonlinearity of metallic nanostructures are presently discussed and are again schematically illustrated in Fig. 4.3. The first one are bulk effects of the electrons in the metal [Fig. 4.3(a)]. The second origin are contributions from the electrons at the surface boundary [Fig. 4.3(b)]. The third possible contribution originates from the local field enhancement in the vicinity of the nanostructure, hence the dielectric surrounding of the structure generates the higher harmonic light [Fig. 4.3(c)]. Additionally, intrinsic resonances of the structures have to be considered.

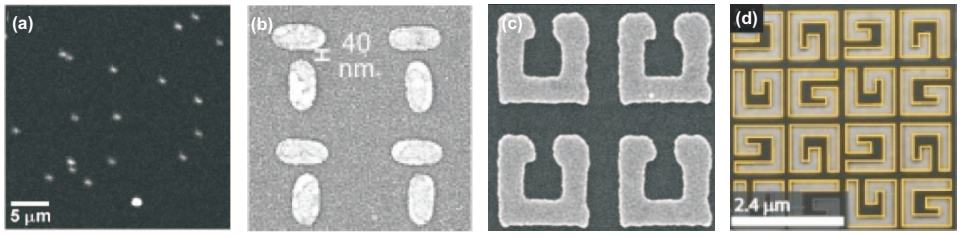

Figure 4.2.: Examples for nonlinear experiments using plasmonic nanostructures: (a) single particles [33], (b) dimers [34], (c) split ring resonators [36]), and (d) planar chiral nanostructures [35].

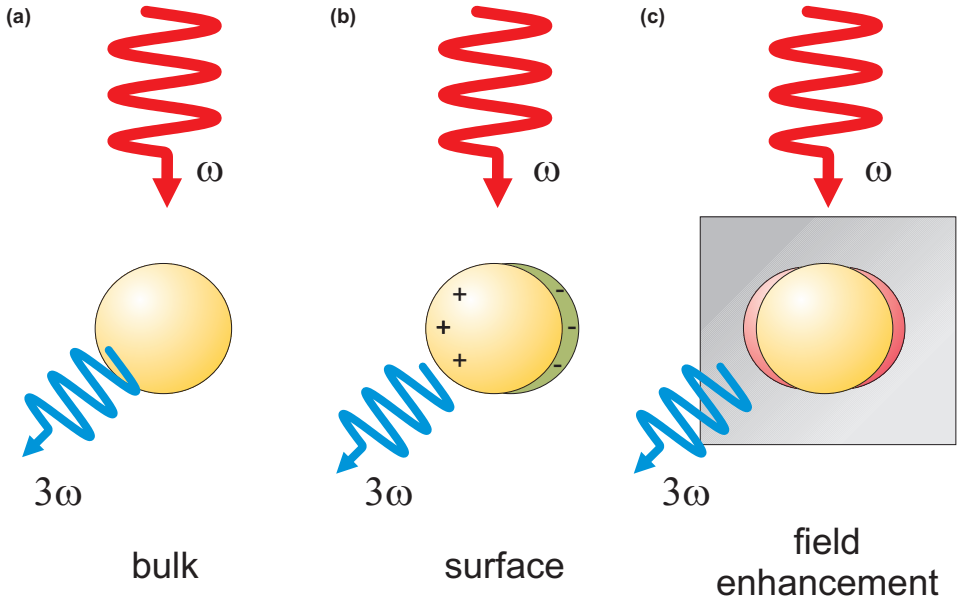

Figure 4.3.: Possible origins of the nonlinearity in plasmonic nanostructures in surrounding media: (a) Nonlinearity of the bulk gold. (b) Nonlinear oscillations of the electron due to anharmonicities at the surface. (c) Harmonic generation in the substrate due to plasmon-mediated electric field enhancement.

The variety of contributions to the nonlinear response which are retrieved from the investigations of different metallic nanostructures render it difficult to give an *a priori* prediction of the nonlinear response of a specific plasmonic nanostructure. In the following, a spectroscopic THG method is introduced in order to reveal the origin of the nonlinearity in metallic photonic crystals. It will be shown that by systematically varying the structure geometry and the constituent materials, the experimental data provide the answer to the eminent question where the nonlinearity in those hybrid plasmonic structures originates from. Several theoretical approaches are discussed afterwards which confirm the findings qualitatively.

4.3. Embedded metallic photonic crystal structure

In the following, the origin of the nonlinearity in metallic photonic crystal structures should be investigated in more detail. One important question is whether the metal or the dielectric waveguide serves as the origin of the nonlinear signal. To answer this question, THG spectroscopy experiments are performed and it is suspected that the contributions of the two materials can be spectrally separated.

As it will become clear later, a small polariton splitting of the two WPP modes is desired in this experiment, i.e., the extinction dip inbetween the WPP modes should be as narrow as possible. This can be achieved by embedding the plasmonic grating into the dielectric waveguide [see Fig. 4.4(a)]. In the fabrication process the grating is patterned on the substrate in a first step using electron beam lithography, then the dielectric waveguide is thermally evaporated on the substrate and the grating in a second step.

In order to understand the influence of the grating position within the waveguide on the polariton splitting of the WPP modes, the analogy to the two coupled harmonic oscillators is reviewed (see Fig. 2.4). In the case of two classical harmonic oscillators the splitting of the eigenmodes is proportional to the coupling strength which is mediated by the spring. Similarly, the polariton splitting of the WPP modes in the metallic photonic crystal structure can be influenced by the coupling of the PPP to the waveguide mode. Here, the coupling strength of the PPP to the waveguide mode is determined by the overlap of the electric near field of the PPP and the electric field distribution within the waveguide. This is schematically depicted in Fig. 4.4(b). On the one hand, the near field of the PPP decreases exponentially with distance. Therefore the electric field overlap could be reduced by moving the plasmonic grating away from the waveguide. This can only be done sufficiently by using a dielectric spacer layer between the plasmonic grating and the waveguide. In previous experiments this method has been investigated in more detail [132]. However, it turns out that rather thick spacer layers have to be used in order to decrease the polariton splitting sufficiently, which is experimentally challenging.

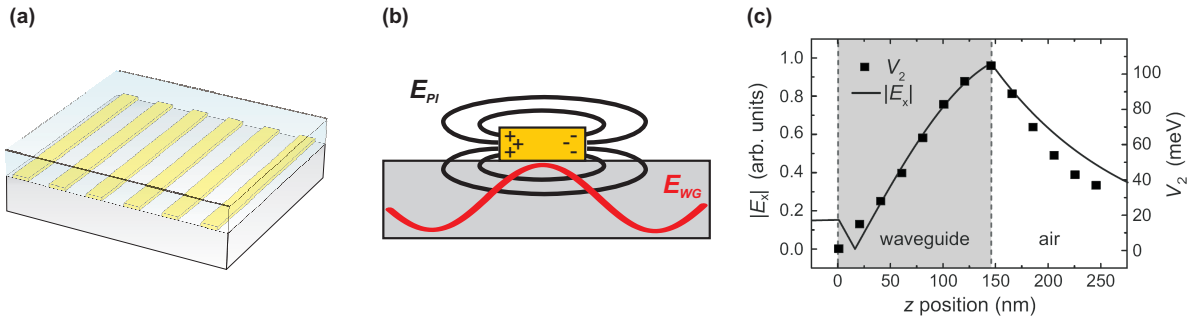

Figure 4.4.: (a) Embedded metallic photonic crystal structure having the waveguide on top of the grating. (b) Schematic of the overlap of the electric field in the waveguide and the plasmonic field. (c) Absolute value of the E_x-component amplitude of the electric field throughout the structure together with the coupling parameter V_2 (from [133]).

On the other hand, the field distribution in the waveguide is not uniform. If the dispersion relation for the waveguide is known, the electric field distribution can be calculated. The relevant field component is E_x since this component can interact with the PPP which oscillates in the x-direction as well. Fig. 4.4(c) shows the absolute value of the E_x-component of the waveguide mode in the structure. It has its maximum at the waveguide-to-air interface and decreases exponentially in the air half space. Since the waveguide is surrounded by materials with different dielectric functions, the field distribution is not symmetric and the minimum of $|E_x|$ is not found in the middle of the waveguide.

To confirm the relation between $|E_x|$ and the coupling of the PPP to the waveguide mode, an effective Hamiltonian H_{eff} of the system near the center of the first Brillouin zone is considered [15, 133],

$$H_{eff} = \begin{pmatrix} E_{wg} + \tilde{c}k_x & V_1 & V_2 \\ V_1 & E_{wg} - \tilde{c}k_x & V_2 \\ V_2 & V_2 & E_{pl} - i\Gamma \end{pmatrix}, \tag{4.4}$$

where the diagonal elements represent the fundamental modes. E_{wg} and $\tilde{c}$ are the TM mode energy and the group velocity, E_{pl} and Γ the energy and the damping of the individual PPP, respectively. The off-diagonal elements are the photon-photon coupling energies between the symmetric and antisymmetric TM waveguide mode, V_1, and the waveguide-plasmon coupling energy, V_2. H_{eff} can be derived from a set of coupled equations describing the coupling of the fundamental modes of the system (PPP and waveguide modes). Together with the coupling constants the eigenvalues of H_{eff} represent the eigenstates of the coupled system (WPP modes). To determine V_2 as a function of z-direction, extinction spectra are calculated for different z-positions of the wires in the waveguide. By fitting H_{eff} to the calculated spectra, V_2 is obtained. Fig. 4.4(c) shows the behavior of V_2 as a function of the z-position of the wires in the waveguide.

As expected, V_2 follows the trend of the electric field component E_x in the waveguide. Therefore the ideal position for the grating to achieve minimum coupling and the smallest polariton splitting of the WPP modes is found at the bottom of the waveguide.

Fig. 4.5(a) shows the linear extinction spectrum of an embedded metallic photonic crystal structure. As waveguide material tungsten oxide (WO_3) with a thickness of 120 nm has been used since it has a larger refractive index (n = 1.91) compared to quartz and can easily be evaporated thermally. The gold grating period is 550 nm and the wire cross-section is 140×30 nm^2. The spectrum is characterized by a broad resonance in the near infrared with a narrow extinction dip at 850 nm with a FWHM of only 10 nm which is strongly modulated in amplitude. In other words the WPP mode resonances at around 836 nm and 866 nm show a rather small polariton splitting of only 51 meV.

Due to the narrow and a strong modulation of the extinction dip, which is much more pronounced than in the pure plasmonic EIT structures, these structures have ideal properties for optical sensing applications [19, 20, 134]. However in 3D plasmonic EIT structures, a single unit cell provides the optical response alone which drastically reduces the effective sensing volume. For the embedded metallic photonic crystal structures, a bunch of unit cells (gold wires) has to be illuminated simultaneously in order to achieve the narrow dip in the spectrum.

4.4. Experimental setup

To investigate the nonlinear optical properties of the embedded metallic photonic crystal structures, ultrashort laser pulses have to be used again for the excitation which provide high peak intensities. However, the *VENTEON* laser with the broad spectrum has some disadvantages for the following experiments. Since the spectrum covers the whole extinction spectrum of the sample, both WPP modes at ω_1 and ω_2 are excited at the same time. Therefore the THG spectrum has a complicated shape since in the THG regime contributions at $3\omega_1$, $3\omega_2$, $2\omega_1 + \omega_2$, and $2\omega_2 + \omega_1$ are expected [98]. It would be rather advantageous to measure the THG spectrum in small wavelength steps and observe the nonlinear responses of small spectral regions of the linear spectrum. Thus a different femtosecond laser system (*Coherent, MIRA*) with larger pulse durations on the order of 150 fs is used. Fig. 4.5(a) shows the spectrum of the laser with a linewidth of ≈ 7 nm which can be tuned continuously over a spectral range from 750 nm to 900 nm. Now the two WPP modes can be excited separately. The limited tuning range of the laser is one reason for the embedded structure with the reduced polariton splitting since it is desired to have both WPP modes within the tuning range of the laser.

Fig. 4.5(b) shows a schematic of the experimental setup. Because the 150 fs laser pulses are not as sensitive to dispersion as the 8 fs pulses, standard optics components can

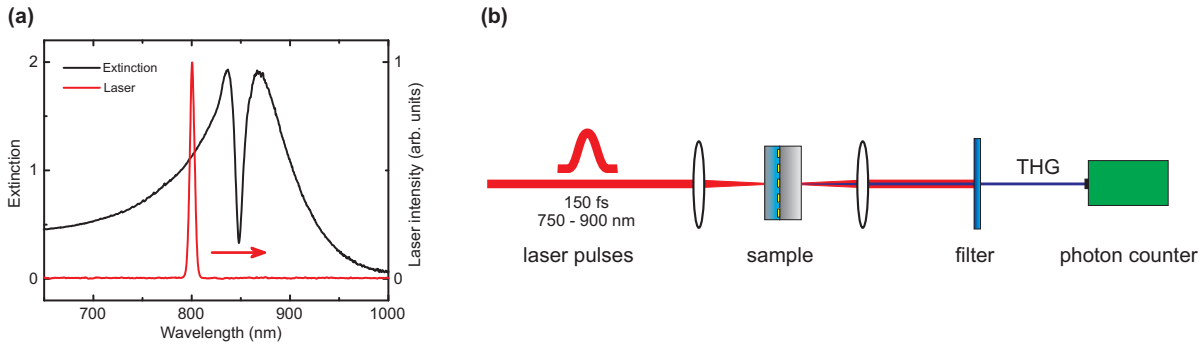

Figure 4.5.: (a) Extinction spectrum of an embedded metallic photonic crystal structure showing a narrow extinction dip. The laser with a linewidth of 7 nm is tuned over the resonances. (b) Schematic of the experimental setup. The 150 fs laser pulses are slightly focused onto the sample. The THG light is filtered from the fundamental frequencies and detected as a function of the center laser frequency using a photon counting photomultiplier.

be used without increasing the laser pulse duration too much. The light is focused with a f = 100 mm lens onto the sample to a spot size of $\approx 10\mu$m. This leads to a small divergence angle of only 0.3° and the excitation of the antisymmetric waveguide mode can thus be neglected. The transmitted fundamental light and the third-harmonic light are recollimated with a second lens and spatially separated in a prism sequence in order to block the fundamental light. Since the pulse duration is longer compared to the ultrafast measurements, the peak intensity is much lower and the THG intensity is below the noise level of the photomultiplier. Therefore a photon counting photomultiplier with a higher sensitivity is used in the THG spectroscopy experiments.

The center wavelength of the laser can easily be tuned, however, the average power might slightly change for different center wavelength. In order to account for this variation it is ensured that the average power on the sample is always the same. It was found that an average power of 60 mW is sufficient for a satisfying signal to noise ration of the THG signal but it is small enough to avoid sample destruction [135]. Together with the average power, pulse duration, beam diameter, and beam path might vary as well upon tuning the center laser wavelength which results in undesired variations of the THG intensity. Therefore the THG intensity measured on the sample is always normalized to the signal that is obtained on a spot right next to the gold grating fields and which solely originates from the waveguide material and the quartz substrate. Furthermore, the setup allows to measure the intensity of the transmitted fundamental light behind the sample in order to determine the extinction for each wavelength step.

4.5. Experimental results

4.5.1. Variation of the plasmon resonance

In a first experimental step a sample series is investigated where the wire width is increased starting from 70 nm to 80 nm and 90 nm. Here, the WO_3 waveguide thickness is 165 nm, the period of the grating is 530 nm, and the thickness of the gold wires is 15 nm. Fig. 4.6(a)-(c) show the linear extinction spectra of the three samples measured with the white light transmission setup. A pronounced and narrow extinction dip at 790 nm is observable. Around 770 nm a kink is visible in the spectrum. It steams from the first Rayleigh anomaly of the grating [16]. At lower wavelength, higher diffraction orders for the fundamental light are opened which complicate further interpretations. Therefore the investigation is restricted to the range of larger wavelength than the Rayleigh anomaly. The PPP resonance is red-shifted with increased wire width while the extinction dip stays rather constant. Additionally, the extinction spectrum which is calculated using the scattering matrix algorithm is plotted. A very good agreement with the experimental curves is found. The spectral phase is a result of the scattering matrix calculations as well and will be discussed later.

Fig. 4.6(d)-(f) show the nonlinear spectra. First, for each wavelength the extinction is determined again using the laser in order to verify the exact position of the extinction dip. The average power of the transmitted fundamental light intensity is measured through the structure (I_T) and through the substrate at a point next to the structure (I_{T_0}). Then the extinction is calculated according to Eq. 2.30.

In the next step, the THG intensity is measured at the metallic photonic crystal structure and normalized to the substrate signal. In a first assumption one would expect a similar shape of the nonlinear spectra when compared to the linear spectra. Nonlinear effects are always very efficient if the fundamental or the higher harmonic light is resonant to a transition in the medium. If the absorption of the fundamental light is large, a lot of light can be converted to the nonlinear regime. Hence at peaks in the extinction, peaks of the THG signal are expected as well. However, the nonlinear spectra have a completely different shape when compared to the linear extinction spectra and all three spectra show a similar behavior. Indeed, a peak in the THG can be found at the long wavelength extinction maximum. However, there is a THG peak as well at the extinction dip. The long wavelength peak shows a red-shift for increased wire width. This observation indicates that this peak is related to the PPP resonance in the metal wires. The appearance of the other peak, however, is *a priori* not clear. Its origin will be investigated in section 4.6 with the help of theoretical descriptions.

Another important observation should be briefly pointed out. On the short wavelength side all three samples show a normalized THG intensity which is smaller than one. Here

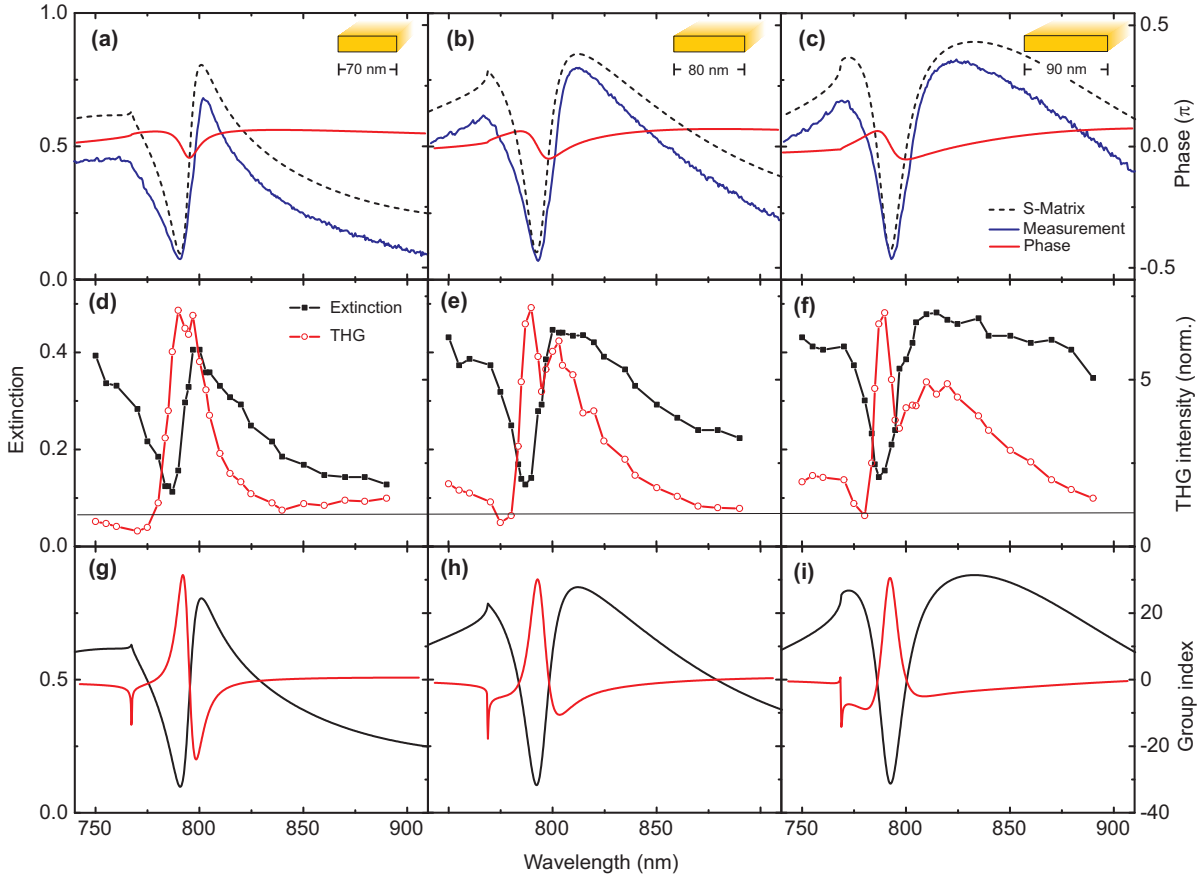

Figure 4.6.: (a)-(c) Extinction spectra of a sample series with increasing gold wire width together with the spectral phase distribution obtained from S-matrix calculations. (d)-(f) Extinction measured stepwise using the laser pulses (squares). The THG intensity is normalized to the signal from substrate plus waveguide and has a different shape than the linear spectrum (circles). (g)-(i) Extinction together with the group index calculated from the spectral phase. The group index is always largest at the extinction dip.

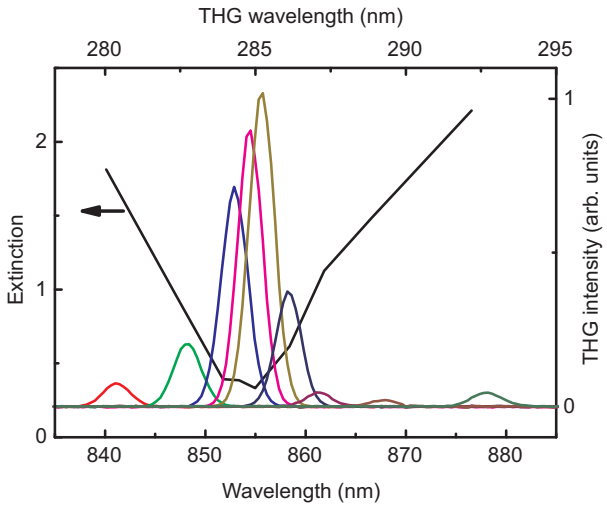

Figure 4.7.: THG spectra for certain center laser wavelength showing only a nonlinear signal at the threefold fundamental frequency.

the metallic photonic crystal structures generate less THG than substrate plus waveguide. This observation could be related to destructive interference of THG signals which originate from different spatial parts of the sample. Shadowing effects of the grating could be a further reason. This unusual effect will be object of further investigations in the future.

In a control experiment, the spectral shape of the individual THG signals is studied. Here, the THG signal is spectrally resolved with a spectrometer and plotted for several center laser wavelength in Fig. 4.7. It is found that the nonlinear spectra have a trivial shape. No other light except at the threefold fundamental frequencies is observed. It can be concluded that THG is the only relevant nonlinear process in the structures. Therefore it is reasonable to measure the THG signal in a spectrally integrated fashion.

4.5.2. Variation of the waveguide material

From the experimental results in the previous section it was assumed that the long wavelength peak in the THG spectra is related to the PPP resonance. If the PPP is red-shifted with increasing wire width, the spectral position of the THG peak changes as well. In a second experimental step the influence of the waveguide nonlinearity on the shape of the THG spectra should be investigated by varying the dielectric material.

A first sample is fabricated which has a Al_2O_3 waveguide on top of the plasmonic grating. The thickness of this waveguide is 190 nm. Since Al_2O_3 has a slightly smaller refractive index (n = 1.76) than WO_3, the sample geometry of the plasmonic grating is adjusted

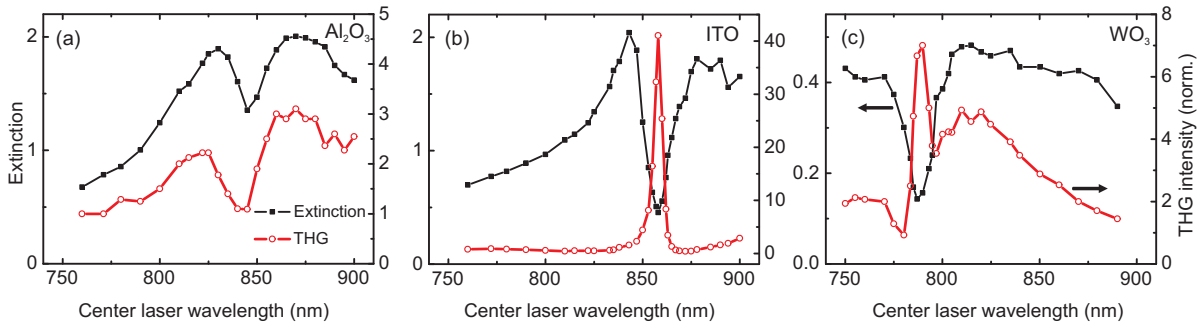

Figure 4.8.: THG spectral for metallic photonic crystal structures with different waveguide materials. (a) For Al_2O_3 as the waveguide material, the THG spectrum shows the same shape as the extinction. No THG peak at the extinction minimum is visible. (b) For ITO, the THG spectrum shows only an intense peak at the extinction minimum. (c) For comparison the THG spectrum of the WO_3-sample is plotted which shows mainly two peaks.

in order to shift the extinction dip to the tuning range of the laser. The grating period is 565 nm and the nanowire cross-section 150×30 nm^2. Figure 4.8(a) shows the linear extinction spectrum measured with the laser together with the THG spectrum. At this sample the extinction dip is less modulated than for the WO_3 samples. For verification white light transmission measurements were performed which show similar results. In contrast to the WO_3 samples, the nonlinear spectrum has a similar shape as the linear spectrum and the THG signal shows no peak at the position of the extinction dip.

For the second sample, ITO is used as the dielectric waveguide material. The thickness of the ITO layer on top of the plasmonic grating is 165 nm. Again the grating geometry is slightly adjusted in order to compensate the refractive index change ($n_{ITO} = 1.74$). Here the grating period is 570 nm and the nanowire cross-section 120×30 nm^2. The linear and the nonlinear spectrum are shown in Fig. 4.8(b). The extinction has again a narrow and pronounced dip at 855 nm. The nonlinear spectrum, however, has a completely different shape when compared to the samples before. The THG signal is low over a large spectral range. Only at the position of the extinction dip there is a strong increase of the nonlinear signal with a narrow linewidth. For a direct comparison Fig. 4.8(c) displays once more the measurements of the WO_3 waveguide with a wire width of 90 nm showing both THG peaks.

In order to obtain a first qualitative understanding of the THG spectrum shape variations for different waveguide materials, the tabulated nonlinear coefficients of the materials are compared. On the one hand, Al_2O_3 has a nonlinearity on the order of $\chi^{(3)} = 10^{-22} \frac{m^2}{V^2}$ only which is the same order of magnitude as for the quartz substrate [136]. On the other hand is has been found from the nonlinear ACF measurements in chapter 3 that a thin layer of ITO leads to a strong THG signal. As expected ITO has a rather large nonlinear coefficient. A tabulated value on the order of $\chi^{(3)} = 10^{-20} \frac{m^2}{V^2}$ can be

found in literature [137]. From the measurements it seems as if the THG peak at the extinction dip increases with the nonlinear coefficient of the waveguide material. In the theoretical descriptions it will be confirmed that the THG peak at the extinction dip indeed originates from the dielectric waveguide material.

Unfortunately, no tabulated value for the nonlinearity of WO_3 has been found in the literature so far. However, from the experimental results it can be assumed that the value of the third order nonlinearity lies somewhere between the values of Al_2O_3 and ITO since both peaks are visible in the spectrum, simultaneously.

4.6. Theoretical descriptions

In order to gain more insight into the origin of the nonlinearity in metallic photonic crystals, several theoretical descriptions are presented in this section to describe the shape of the THG spectra theoretically. The first one is based on rigorous electric field calculations. In the second one the fundamental modes of the system are modeled as damped harmonic oscillators. In the third explanation the linear optical processes are related to electromagnetically induced transparency.

4.6.1. Electric field distribution simulations

In the first theoretical approach the scattering matrix algorithm [74] is utilized to calculate the electric field distribution for the unit cell of the metallic photonic crystal structure. Figure 4.9 shows the amplitude of the electric field for the sample whose spectrum is presented in Fig. 4.6(f). For the wavelength of the extinction dip ($\lambda = 792$ nm) the electric field is mainly concentrated in the waveguide and in the substrate [see Fig. 4.9(a)]. Inside and in the vicinity of the metal the electric field is close to zero. This field distribution explains the extinction dip in the linear spectrum as well. The negligible field in the vicinity of the wire is a direct consequence of the destructive interference of the plasmonic field in the wire and the waveguide mode, thus leading to a high transmission.

Figure 4.9(b) shows the electric field for the extinction maximum at $\lambda = 832$ nm. Now the field distribution has a completely different shape. The electric field is mainly concentrated inside and in the vicinity of the metal. This observation confirms the plasmonic character of the broad WPP mode.

In the next step the nonlinear response is calculated from the electric field distribution $\mathbf{E}(\omega, \mathbf{r})$. Therefore a local nonlinear polarization is assumed which takes the dipolar bulk

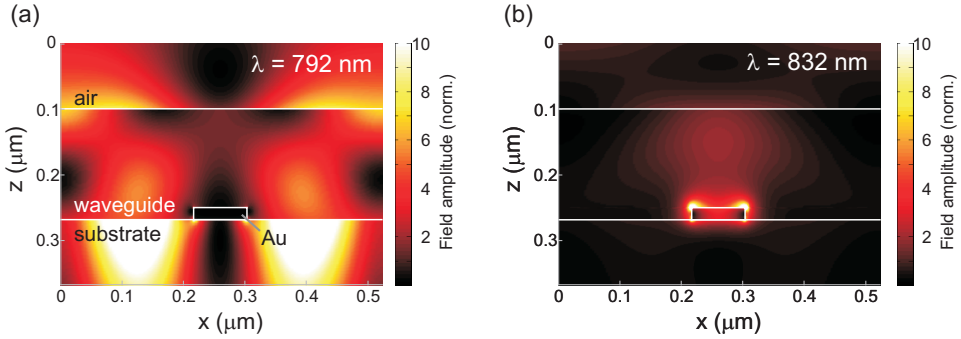

Figure 4.9.: Electric field distribution calculations for the unit cell of the structure. (a) At the wavelength of the extinction minimum the electric field is mainly concentrated in the waveguide material and the substrate, no field is inside the metal. (b) At the extinction maximum the electric field is predominantly located inside and in the vicinity of the metal. For optimum contrast the linear color scale is limited to a value of 10.

contributions of each material component into account:

$$\mathbf{P}^{(\mathrm{NL})}(3\omega, \mathbf{r}) = \hat{\chi}^{(3)}(-3\omega; \omega, \omega, \omega, \mathbf{r}) \vdots \mathbf{E}^3(\omega, \mathbf{r}). \tag{4.5}$$

From Eq. 4.5 it is obvious that $\mathbf{P}^{(\mathrm{NL})}(3\omega, \mathbf{r})$ strongly depends on the actual field distribution $\mathbf{E}(\omega, \mathbf{r})$ inside the nanostructure. Since the largest field enhancement is spectrally different in the metal and in the dielectric (compare Fig. 4.9), it is expected that the two THG peaks are related to the relevant constituent of the nanostructure. To confirm this assumption, rigorous numerical calculations relying on an extended scattering matrix algorithm are performed to determine the THG in the forward direction [138]. Applying this method, the tensorial character of the $\chi^{(3)}$ coefficients of all materials is fully taken into account which are assumed to belong to a cubic isotropic crystallographic lattice. Then the tensor comprises only a single independent component. The nonlinear feedback of the generated third-harmonic to the fundamental field is neglected (undepleted pump approximation). The relative amount of THG observed in the experiments strongly justifies this assumption to be valid. For simplification contributions from the substrate are always neglected because its THG signal is spectrally flat and rather weak.

To investigate the individual contributions of the two materials three different scenarios have been calculated. While keeping the linear properties of the structure constant, the ratios $\chi^{(3)}_{\mathrm{Au}}/\chi^{(3)}_{\mathrm{wg}}$ of the nonlinear coefficients are adapted. First, the two limiting cases when either $\chi^{(3)}_{\mathrm{wg}}$ or $\chi^{(3)}_{\mathrm{Au}}$ is set to zero are investigated. In Fig. 4.10(a) the nonlinearity of the dielectric waveguide material ($\chi^{(3)}_{\mathrm{wg}}$) is assumed to be zero. Hence a THG spectrum with a shape very similar to the linear extinction spectrum is obtained. At the extinction dip where the electric field in the metal is low [compare Fig. 4.9(a)], a reduced THG signal is observed. On the contrary if $\chi^{(3)}_{\mathrm{Au}}$ equals zero, the nonlinearity of the dielectric is dominating [see Fig. 4.10(b)]. The THG spectrum shows a pronounced peak which

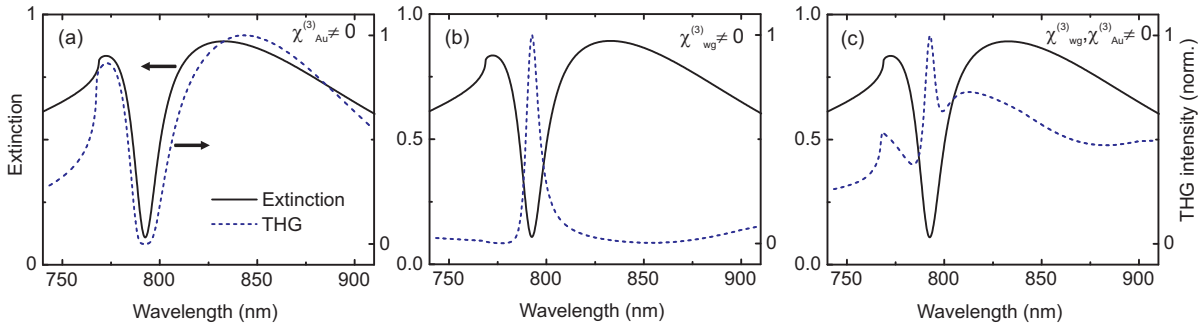

Figure 4.10.: Calculated THG spectra for different $\chi^{(3)}_{Au}/\chi^{(3)}_{WG}$ ratios. (a) If only the metal is considered to be nonlinear, the calculated THG spectrum has the same shape as the linear extinction spectrum. (b) If a nonlinear coefficient is only attributed to the dielectric waveguide material, the THG spectrum has a peak at the linear extinction minimum. (c) If both material contribute to the nonlinearity, the THG spectrum shows peaks at the linear extinction maxima and at the minimum.

coincides with the extinction dip. Finally, by carefully adjusting the ratios of the nonlinear coefficients, the case is reached where both materials contribute equally, such that a combination of the two previous cases is observed [Fig. 4.10(c)].

The situation in Fig. 4.10(a) corresponds to the measurements with the Al_2O_3 waveguide whose nonlinearity is rather low. Figure 4.10(b) is similar to the THG spectrum which has been obtained form the ITO sample with a large nonlinearity. Finally, Fig. 4.10(c) can be compared to the WO_3 measurement. From these simulations it can be concluded that the THG peak at the extinction dip originates from the dielectric waveguide material while the THG peak at the extinction maximum originates from the metal. Consequently, the shape of the nonlinear spectrum can help in order to determine the material origin of the nonlinear response.

It is interesting to note that the PPP-mediated field enhancement in the waveguide material, which is visible in the field distribution at 832 nm, does not show up as a second peak in Fig. 4.10(b). Although, the high field at the corners of the metal, which lacks out into the waveguide, is quite large, its contribution after integrating over the whole waveguide volume is not eminent.

In the future, this model could help in order to *quantitatively* compare simulations with experimental data. Maybe even values for the nonlinear susceptibility of gold could be determined. So far on gold surfaces a value of $\chi^{(3)}_{Au} = 2 \cdot 10^{-19} \frac{m^2}{V^2}$ has been reported in literature [139]. It would be very interesting to investigate if this value can be confirmed in metallic nanostructures.

From further theoretical investigations using this model it has been found that a sig-

nificant amount of THG intensity is diffracted away from the normal direction. Since the plasmonic grating is not sub-wavelength for the THG frequencies, higher diffraction orders are opened. Since in the experiment it is not possible to collect the higher diffraction orders so far, a closer investigation of the higher diffraction orders is still due.

4.6.2. Coupled harmonic oscillator model

In the previous description, the main focus was on the material properties of the metallic photonic crystal. So far, no model has been used in order to describe the resonances, instead the THG spectra were calculated *ab initio*. In the next description, the resonances are regarded in particular and the description starts again with an harmonic oscillator model. In contrast to section 3.1.4 where the WPP modes are modeled by harmonic oscillators, the fundamental linear optical modes, i.e., the PPP and the waveguide mode, are now described as damped harmonic oscillators which are driven by an external electric field $E(t)$ [40]. According to Eq. 2.20 and 2.21 this leads to two coupled differential equations

$$\ddot{x}_{pl} + 2\gamma_{pl}\dot{x}_{pl} + \omega_{pl}^2 x_{pl} + (NL)_{pl} - \omega_c^2 x_{wg} = -q_{pl}\frac{e}{m}E(t) \tag{4.6}$$

$$\ddot{x}_{wg} + 2\gamma_{wg}\dot{x}_{wg} + \omega_{wg}^2 x_{wg} + (NL)_{wg} - \omega_c^2 x_{pl} = -q_{wg}\frac{e}{m}E(t). \tag{4.7}$$

Here, $x_{pl}(t)$ and $x_{wg}(t)$ are the displacements representing the PPP and waveguide mode oscillation, respectively. The resonance frequencies, half widths at half maximum, and oscillator strengths of the uncoupled system are denoted by ω_j ,$\gamma_j = 1/T_2, j$, and q_j $(j = pl, wg)$, respectively. ω_c^2 represents the coupling strength between the oscillators. Since the coupling is not mediated by a spring such as in Eq. 2.20 and 2.21, the coupling terms are given by $\omega_c^2 x_j$. Without the nonlinear terms $(NL)_j$ the coupled linear differential equations can be easily solved and via the total linear polarization $P_j^{(1)}(\omega) \propto x_j^{(1)}(\omega)$ the absorption coefficient $\alpha(\omega)$ is calculated. Since the coupling of the PPP to the waveguide mode is inherent in the model, the calculated absorption shows the experimentally observed Fano line shapes in the spectrum. This is not possible with the previously discussed harmonic oscillator model where the WPP resonances are directly described by Lorentzian line shapes (compare section 3.1.4). The disadvantage of the present model is that it is more difficult to fit the theoretical spectrum to the experimental one since the parameters of the fundamental modes, such as γ_j or q_j, are not known beforehand.

In the nonlinear regime, the terms $(NL)_j$ are not zero. One might expect terms such as $(NL)_j \propto x_j^3$. However, it has been found that the terms are of a more general form

$$\eta_{j,k}\left[x_{pl}(t)\right]^{3-k}\left[x_{wg}(t)\right]^{k}, \tag{4.8}$$

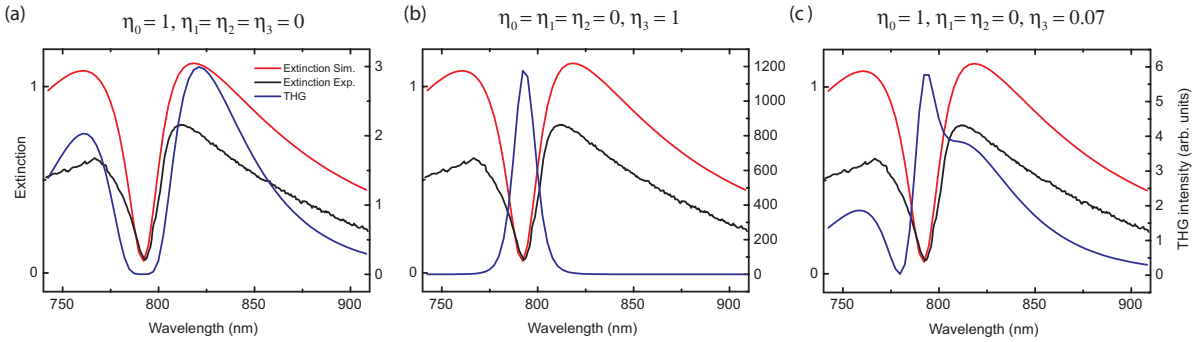

Figure 4.11.: THG calculated from the coupled oscillator model. (a) Only the contribution of the oscillator representing the PPP is taken into account ($\eta_0 = 1, \eta_1 = \eta_2 = \eta_3 = 0$). (b) Only the waveguide oscillator is considered to possess a nonlinearity ($\eta_0 = \eta_1 = \eta_2 = 0, \eta_3 = 1$). (c) Contributions of both oscillators are merged ($\eta_0 = 1, \eta_1 = \eta_2 = 0, \eta_3 = 0.07$).

$j = pl, wg; k = 0, 1, 2, 3$. Furthermore, the nonlinear displacements are given by

$$x_j^{(3)}(t) \propto \sum_{k=0}^{3} \eta_{j,k} \left[x_{pl}(t)\right]^{3-k} \left[x_{wg}(t)\right]^{k} . \tag{4.9}$$

The eight parameters $\eta_{j,k}$ are reduced to four, and the third-order polarization reads

$$P^{(3)}(t) \propto \sum_{k=0}^{3} \eta_{k} \left[x_{pl}(t)\right]^{3-k} \left[x_{wg}(t)\right]^{k} . \tag{4.10}$$

A detailed derivation can be found in Ref. [40]. In contrast to that, here the electric field of the narrow-band laser of the experiment is used, $P^{(3)}(t)$ is calculated for each center laser wavelength separately, and the THG spectrum is obtained.

Figure 4.11 shows the results. In a first step the linear absorption is calculated and fitted to the linear extinction spectra. The parameters for a reasonable agreement are $\hbar\omega_c = 0.42$ eV, $q_{wg}/q_{pl} = 0.01$, $T_{2,pl} = 3.8$ fs, $T_{2,wg} = 600$ fs, $\hbar\omega_{pl} = 1.565$ eV, and $\hbar\omega_{wg} = 1.58$ eV. However, the shape of the calculated spectrum still shows discrepancies to the measured ones. The main reason for this is the Rayleigh anomaly at 770 nm which cannot be reproduced by the harmonic oscillator model. Since scattering can be neglected in a first approximation, the calculated absorption is directly compared to the measured extinction.

For the nonlinear spectra three different scenarios are calculated. First, only the contribution of the PPP is taken into account. In Eq. 4.10 the four nonlinear parameters η_k are set to $\eta_0 = 1$ and $\eta_1 = \eta_2 = \eta_3 = 0$, thus only the displacement of the PPP oscillator $x_{pl}(t)$ contributes to the nonlinear polarization $P^{(3)}(t)$. The nonlinear spectrum is shown in Fig. 4.11(a) and has a similar shape as the linear extinction spectrum with no THG

contribution at the extinction dip. Second, only the waveguide contribution is taken into account and the nonlinear parameters are set to $\eta_0 = \eta_1 = \eta_2 = 0$, $\eta_3 = 1$. Now only $x_{wg}(t)$ contributes to the third-order polarization. The THG spectrum shows a single peak at the position of the extinction dip [see Fig. 4.11(b)]. Finally, the nonlinear parameters are adjusted in order to observe PPP and waveguide contributions simultaneously. For the present case the parameters are $\eta_0 = 1$, $\eta_1 = \eta_2 = 0$, and $\eta_3 = 0.07$. Indeed Fig. 4.11(c) shows one THG peak at the extinction maximum and one peak at the extinction dip.

The coupled harmonic oscillator model leads to a similar conclusion as the electric field distribution calculations: The origin of the THG signal can be unambiguously identified from the shape of the nonlinear spectrum. However with the present model, the origin is directly related to the PPP in the metal and the waveguide mode in the dielectric material. It is interesting to note that the nonlinear parameters η_0 and η_3 are very different in order to obtain both contributions simultaneously. This fact might be due to the higher quality factor (smaller FWHM) of the waveguide mode which is related to a larger dephasing time, hence more THG can be accumulated in the waveguide.

It should be mentioned that the THG spectrum can already be reproduced with reasonable quality without taking the influence of the parameters η_1 and η_2 into account. In Eq. 4.6 and 4.7 these two parameters lead to an additional nonlinear coupling of the two equations. However, by comparing the experimental and theoretical results it seems that the nonlinear coupling can be neglected so far.

4.6.3. Electromagnetically induced transparency

In the framework of EIT, the THG peak at the extinction dip can be phenomenologically explained in a straight forward way. Due to the embedding of the plasmonic grating, the linear spectra show a very narrow extinction dip similar to the plasmonic EIT structures which were discussed in chapter 2. Indeed, the embedded metallic photonic crystal structures can be regarded as well as an EIT-analog system. In the present structure, the PPP in the individual gold wires, on the one hand, serve as the bright mode, which can be easily excited by light. The broad resonance, the effective excitability, and the high damping have already been discussed. The waveguide mode, on the other hand, is interpreted as the dark mode (see Fig. 4.12). During the propagation of the light within the waveguide material, it experiences nearly no losses and the damping is very low. Hence, the condition $\gamma_d << \gamma_b << \omega_0$ for EIT is easily achieved [72]. Figure 4.12 visualizes the energy diagram. The coupling κ is mediated by the overlap of the electric fields of both materials.

In contrast to the pure plasmonic EIT systems, the extinction dip is much narrower in the embedded metallic photonic crystal structure. Since the dark mode is a photonic

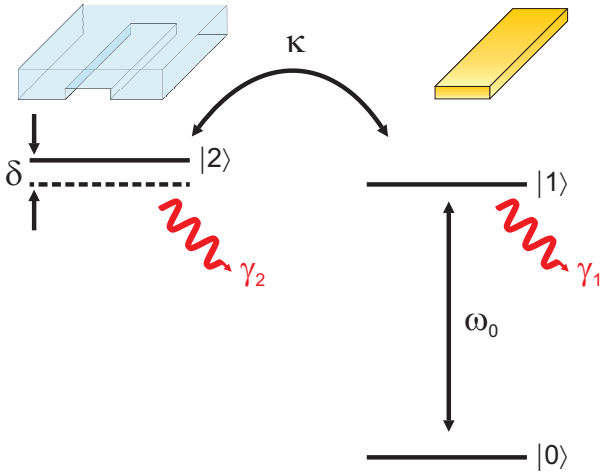

Figure 4.12.: Schematic of the plasmonic-photonic analog of electromagnetically induced transparency. The PPP is the bright mode which can be excited by an external light field ω_0 and the waveguide mode is the dark mode being only excited via the coupling κ in the idealized case.

mode, its damping can be much smaller and it is ultimately limited by the leakage via the grating arrangement of the gold wires. In the 3D EIT structure of Ref. [72], the damping of the dark mode is limited to Drude damping which is in comparison much larger.

The electric field distribution in Fig. 4.9 visualizes the EIT situation at the extinction dip. A large part of the electric field is located in the waveguide, i.e., the dark mode. In the vicinity of the gold wire, the electric field is out of phase by π with the field of the PPP (bright mode) which is directly externally excited [14]. The destructive interference leads to a cancellation of the fields at the wire and subsequently to the extinction dip.

The destructive interference is limited solely to the linear optical regime and does not hold in the nonlinear regime. The field distribution clearly shows that at the extinction dip a lot of energy in stored in the dark mode where it can interfere in a one-photon fashion with the directly excited bright mode. However in the nonlinear regime, the residual electric field in the dark mode can still be converted to its higher harmonics. Therefore, even at the extinction dip a peak in the THG spectrum is observed. It is important to note that in the nonlinear regime the fundamental light is resonant to the bright mode. The situation would be different if the higher harmonic of the light would be resonant to the transition. In the future it would be very interesting to investigate this situation as well. Additionally, the nonlinear response of the 3D plasmonic EIT structures [72] could be compared to the results of the plasmonic-photonic EIT structures.

4.7. THG enhancement with slow light

The nonlinear coefficients of the contributing materials are not the only parameters which influence the intensity of the higher harmonic signals. Recently it has been demonstrated how the group refractive index in a photonic crystal waveguide enhances third-harmonic generation. [140, 141]. The group index is defined as the ratio of the velocity of light c in vacuum to the group velocity v_g of light in a medium:

$$n_g = \frac{c}{v_g}. \tag{4.11}$$

The group velocity is related to the slope of the dispersion relation as

$$v_g = \frac{\partial \omega}{\partial k}. \tag{4.12}$$

Hence, in a spectral region where the dispersion relation is very flat, the group velocity is low and the group index is large.

In Ref. [140] the fundamental light was spatially compressed and slowed down in a silicon-based photonic crystal structure which enhances the electric field intensity. It is calculated by

$$I_\omega \propto \frac{P_\omega}{A\omega} \cdot \frac{n_g}{n}, \tag{4.13}$$

where P_ω is the peak power, A is the effective area, and n_g is the group index of the fundamental light. In the nonlinear regime the THG intensity is proportional to the third power of the fundamental light intensity:

$$I_{3\omega} \propto I_\omega^3. \tag{4.14}$$

Together with Eq. 4.13, $I_{3\omega}$ is subsequently proportional to the third power of the group index. Hence, a large group index can be exploited to increase the nonlinear response.

In the metallic photonic crystal structures, rather large group indices are found as well. In Fig. 4.6(a)-(c) the spectral phase is calculated using the scattering matrix approach. If the spectral phase $\phi(\omega)$ is known, the group index is calculated as

$$n_g = \frac{c}{t} \cdot \frac{d\phi}{d\omega}, \tag{4.15}$$

where t is the thickness of the medium. In the present case the thickness of the waveguide is applied [133]. In Fig. 4.6(a)-(c), the spectral phase $\phi(\lambda)$ has a negative slope around the extinction dip. Therefore, from Eq. 4.15 this results in a positive group index [see Fig. 4.6(g)-(i)]. For all three cases the calculated group index is maximum at the wavelength of the extinction dip and values up to $n_g = 30$ are obtained. By comparing Fig. 4.6(d)-(f) with Fig. 4.6(g)-(i) it is obvious that the THG peak at the extinction

dip always coincides with the maximum group index. At the extinction dip, the light is significantly slowed down in the structure which increases the light-matter interaction time. Hence, by applying Eq. 4.13 and 4.14, the THG peak can be directly related to the maximum group index.

4.7.1. THG enhancement by tailoring the group index

Finally in the last section of this chapter, the group index influence on the intensity of the THG signal is investigated. Therefore a systematic variation of the group index is required. It has been shown previously that the group index is directly related to the coupling strength of the PPP to the waveguide mode. In Fig. 4.4(c) the coupling strength has been investigated and it was found that the coupling decreases when the plasmonic grating is buried deeper into the waveguide slab. With decreasing coupling, the polariton splitting of the WPP modes decreases as well. Therefore the spectral phase changes occur in a less broad spectral range which increases the slopes in the phase spectrum. The group index increases accordingly.

Consequently, the group index can easily be changed by varying the grating position within the waveguide, i.e., the distance d in Fig. 4.13(a). Since an experimental variation of the plasmonic grating position in the waveguide would be extremely challenging, the investigation is restricted to theory. Here, only the nonlinear contribution of the dielectric waveguide material is important. Therefore, a metallic photonic crystal structure with an ITO waveguide is assumed [compare Fig. 4.8(b)] and the same sample parameters as before are chosen. Figure 4.13(b) shows the amplitude of the electric field E_x-component for the actual sample configuration. In order to reproduce the real sample geometry consistently, the thin gray area below $x = 0$ represents a thin ITO adhesion layer which has been used in the experiment.

In the first step, three grating positions are compared. In the first one, the grating is at the bottom of the waveguide ($d = 0$ nm). In the second configuration, the grating is placed in the middle of the waveguide ($d = 67.5$ nm). Finally, the grating is located below the waveguide-to-air interface ($d = 135$ nm). The linear extinction spectra are calculated with the scattering matrix algorithm together with the spectral phases for the three grating configurations. Figures 4.14(a)-(c) show the calculated spectra. As expected, the polariton splitting strongly increases with an increasing distance d of the grating from the bottom of the waveguide. Additionally, the slope of the spectral phase at the extinction dip decreases. The phase evolution is slightly disturbed by the Rayleigh anomaly at around 830 nm but the overall behavior is straight forward as expected.

From the spectral phase the group index is calculated and imposed on the extinction spectra in Figures 4.14(d)-(f). Indeed, the largest group index is found at the extinction dip for the smallest polariton splitting and is drastically decreasing as the grating is

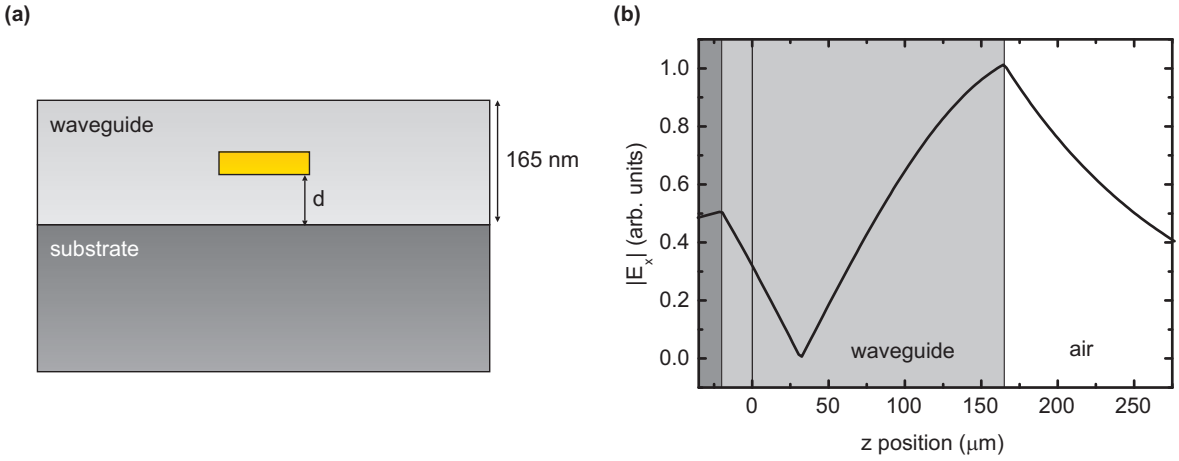

Figure 4.13.: (a) Schematic of the embedded metallic photonic crystal structure. The wire in shifted upwards from the bottom of the waveguide to the top. (b) Amplitude of the E_x-component of the electric field throughout the structure.

placed higher inside the waveguide.

In the next step the observations are related to the intensity of the THG peak. Here, the extended scattering matrix algorithm of section 4.6.1 is utilized again and the THG spectra are calculated from the electric field distribution in the waveguide. For simplification, the nonlinearity of the metal is set to zero. Figures 4.14(g)-(i) show the nonlinear results. Just like the group index, the THG intensity is maximum if the grating is placed at the bottom of the waveguide. For the sample configuration with the grating in the middle of the waveguide, the THG peak is already close to zero. Since the THG intensity depends on n_g^3 (compare Eq. 4.13 and 4.14), the decrease is even stronger than the decrease of the group index.

It is found that the change in the THG intensity is very large from the first grating configuration to the second one. In order to further resolve the evolution, the THG spectra are calculated again for small distances d with a higher resolution. Figure 4.15 shows the THG spectra for small distances d. Interestingly, the THG peak does not decrease monotonously. Rather in the beginning, the THG peak increases with the distance d and after $d = 30$ nm quickly drops to zero. This observation can be understood with the help of Fig. 4.13(b). Starting from $x = 0$ nm, the amplitude of E_x is first decreasing for small x-positions. It reaches its minimum at $x = 35$ nm and increases afterwards. Since $|E_x|$ is not minimal for the grating position $d = 0$ nm, the largest THG peak is not found in the first spectrum.

However, the THG spectrum for $d = 20$ nm does not fit into this series. Here, a unique configuration is achieved. Due to the thickness of the wire of 30 nm, the grating is placed

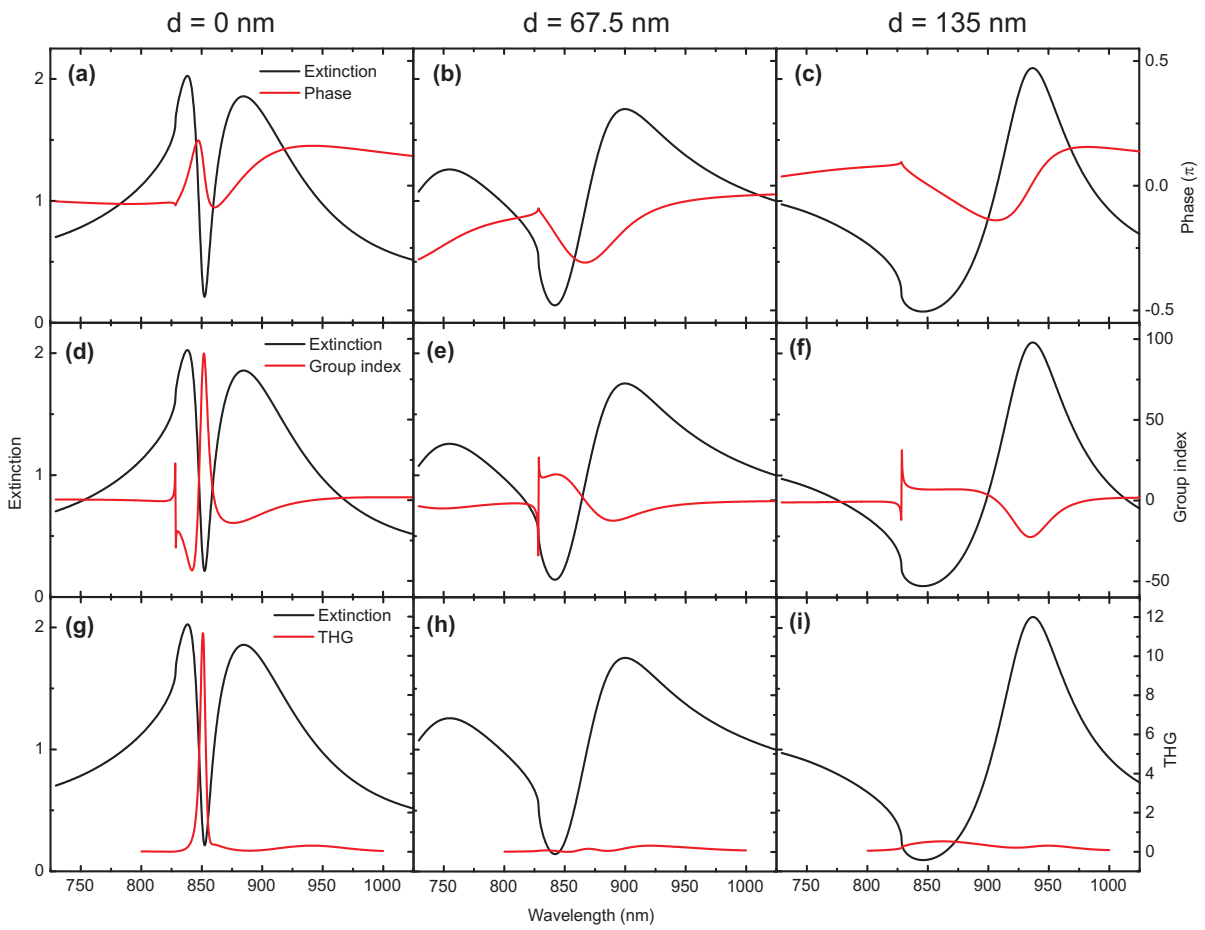

Figure 4.14.: (a)-(c) Extinction spectra for three different wire positions in the waveguide (d = 0 nm, 67.5 nm, and 135 nm) together with the spectral phase from scattering matrix calculations. (d)-(f) Group index calculated from the spectral phase. (g)-(i) THG calculated for the three configurations.

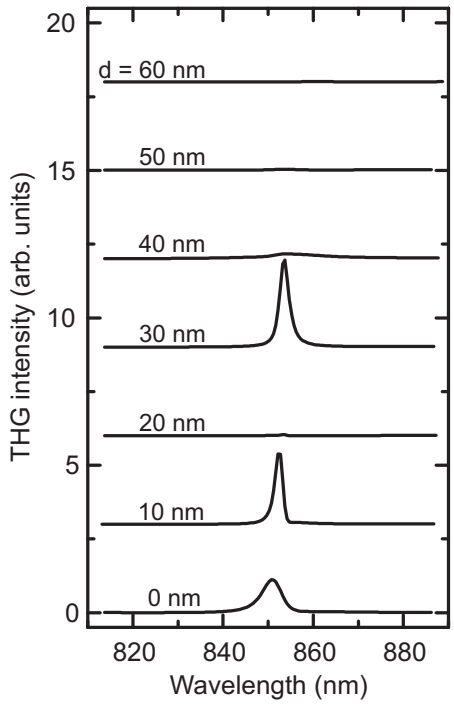

Figure 4.15.: Extinction spectra for different wire positions in the waveguide. The distance d of the wire to the waveguide is increased from bottom to top.

exactly at the minimum of $|E_x|$ if $d = 20$ nm. At this position, the field amplitude in the waveguide is drastically reduced and the waveguide mode cannot be excited by the grating. Hence, the electric field in the waveguide is negligible and no THG is generated. In summary, this parameter study qualitatively confirms the connection of the THG intensity to the group index in the system and presents an alternative qualitative, yet easy to grasp explanation for optical nonlinearities in plasmonic EIT structures.

5. Coherent control of hybrid plasmonic systems

In plasmonic systems, one of the most important challenges is the dynamic ultrafast control of the optical near fields on the nanometer scale and the optical processes on a femtosecond time scale [142]. A static *spatial* control of the optical near fields is achievable by appropriate structuring of the plasmonic system. For example in the gap of a pair of nanoparticles, large electrical near fields can be realized [26]. By changing the structure for example to a bow tie gap antenna, even larger near fields are generated [55]. In 2007 Ropers *et al.* used a sharp metal tip and launched surface plasmon polaritons with a grating corrugation at the broad end of the tip [27]. Dependent on the light incidence with respect to the grating, the near field concentration to the tip was significantly controlled. Only if SPP were launched at the grating, their propagation led to a high concentration of the electric field at the tip.

In chapter 3 it has been demonstrated how the *temporal* dynamics of a plasmonic system can be tailored by using the hybridization method. However, this is a static control method as well, since a change of the temporal dynamics requires a variation of the structure geometry. Therefore, it would be advantageous to employ a method to dynamically control plasmonic systems in space *and* time. One experimental parameter, which can be changed rather fast is the electric field of the light which excites the system. In other physical and chemical systems, such experiments, where the outcome is controlled by light, are well known as *coherent control* and the main concepts are presented in the next sections.

5.1. Definition of coherent control

In general, the term coherent control refers to experiments where a quantum mechanical excitation is affected by light due to quantum interference of different excitation pathways. However, it is used nowadays in a versatile manner and for a variety of experiments with each other, which are based on different approaches. Therefore, it is not always possible to compare coherent control experiments and controversial discussions arise whether an actual experiment can be termed coherent control or not.

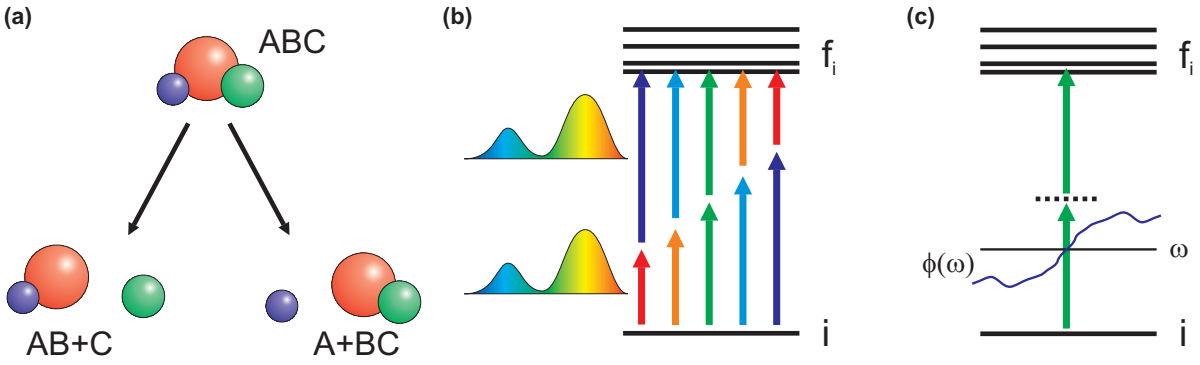

Figure 5.1.: (a) In chemical systems, the concept of coherent control has been utilized to direct the outcome of a chemical reaction. (b) In the two-photon picture, a transition $|i\rangle$ to $|f\rangle$ is excited by any two photons of the laser pulse fulfilling the condition $\omega_1 + \omega_2 = \omega_{if}$. (c) The final state of the system is controlled via the spectral phase of the two photons which can lead to destructive interference of different excitation pathways.

To avoid confusion about the present experiment on coherent control of a hybrid plasmonic system and to position it in the proper context of other experiments, a short classification of coherent control experiments is presented in the following. In the first step, weak field and strong field control [143] experiments can be distinguished. Weak field control experiments are further divided into two-photon and one-photon control experiments. Strong field control experiments require high field intensities and are closely related to effects such as Rabi oscillations. Since strong field control is not object of this thesis, the reader is referred to [144–149] and the discussion is limited to weak field control.

5.1.1. Two-photon coherent control

Coherent control has first been proposed by Brumer and Shapiro in 1986 as a tool to manipulate the yield of a chemical reaction by light [150, 151]. In a simplified picture the task was to control the probability of a molecule compound ABC to dissociate into either the product state $AB + C$ or into $A + BC$ [see Fig. 5.1(a)]. The concept utilizes the interference of different excitation pathways from the initial to the final states of the system. The population in one final state can be tuned via constructive or destructive interference by modifying amplitude and phase of the electric light fields which correspond to the transitions. This concept was first experimentally demonstrated in 1990 by Chen *et al.* [152].

In a slightly different approach, Tannor and Rice proposed to control chemical reactions via a two-photon process using complex shapes of the exciting laser pulses which provides

more degrees of freedom for the control [153]. This approach became possible with the development of pulse shapers in the year 2000 [154]. With them, the pulses are spectrally dispersed in the Fourier domain where amplitude, polarization, and spectral phase can be modulated for each wavelength window, separately.

However, the question remained, what the exact pulse shape has to be for a desired outcome. Judson and Rabitz proposed a learning algorithm by which the optimal pulse shape is obtained iteratively during the experiment [155]. The algorithm processes the signal which is detected from the system upon irradiation with differently shaped laser pulses. In an iterative manner, the optimization algorithm imposes slight changes on the pulse shape in order to optimize the desired experimental outcome. After each step, the pulse shape is slightly improved until the ideal shape is found. Adaptive control was first presented by Bardeen *et al.* who controlled the fluorescence efficiency of dissolved dye molecules [156].

Afterwards, a variety of two-photon coherent control experiments has been presented in different physical and chemical systems. Among others, coherent control in cesium atoms [157–160], iron based molecules [161], and dye molecules [162] should be mentioned. For a detailed collection of experiments the reader is referred to Ref. [163] and [164].

In general, the two-photon coherent control concept can be explained in a simplified picture [see Fig. 5.1(b)]. A quantum mechanical system is excited from an initial state $|i\rangle$ to an excited state $|f_i\rangle$. A first photon of an ultrashort laser pulse excites the system to an intermediate state and a second photon of the same pulse excites the system to the final state. Since the pulse contains a broad spectrum of frequency components, each pair of photons whose frequencies ω_1 and ω_2 fulfill the condition $\omega_{if} = \omega_1 + \omega_2$, where ω_{if} is the transition frequency, contributes to the transition probability. Since the intermediate state is a virtual state with a very short decay time, photon 1 and 2 have to arrive simultaneously. If the spectral phase of the pulse is changed, i.e., the relative phase between photon 1 and 2, the excitation can be inhibited and the total transition probability decreases [see Fig. 5.1(c)]. It is important to note that, although the spectral intensity of the pulse stays the same, the transition is controlled solely by varying the spectral phase of the pulse.

5.1.2. One-photon coherent control

Soon after Brumer and Shapiro coherent control experiments were suggested, where a one-photon excitation is exploited by extremely short laser pulses [165]. However, it was shown by Brumer and Shapiro that this method is only a passive control fashion which is not due to *quantum* interference [166].

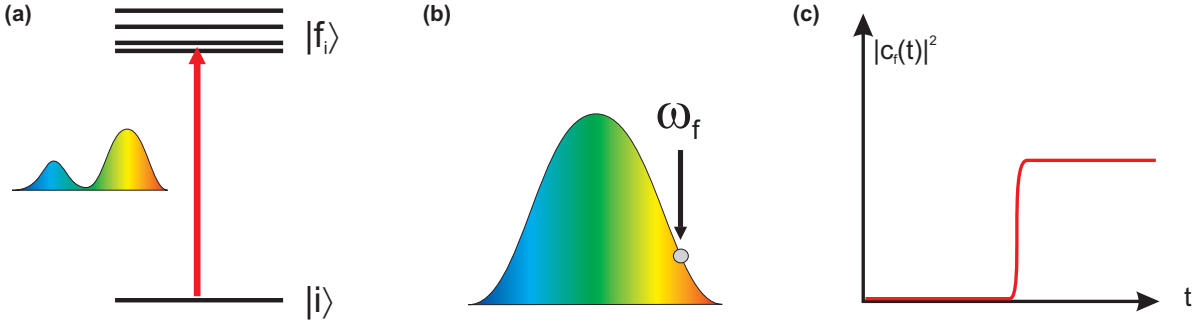

Figure 5.2.: (a) In the one-photon picture a transition $|i\rangle$ to $|f\rangle$ can be excited by a laser pulse. (b) Only the frequency which is resonant to the transition will interact with the system. (c) Therefore the final state of the system does not depend on the pulse shape.

In the simplified picture of one-photon coherent control, the initial state $|i\rangle$ can only be excited to a final state $|f_i\rangle$ by one single frequency ω_f within the laser spectrum, which corresponds to the transition [see Fig. 5.2(a) and (b)]. The transition is only excited if the spectral intensity of the laser pulse at ω_f is non-zero. Therefore, the same result would be achieved with a *cw*-light source at the required frequency by switching it on or off. Hence, this control scheme does not utilize the spectral phase of the laser pulses but only the spectral intensity. If only the spectral phase of the pulse is changed, the probability $|c_f|^2$ of the system to be in state $|f_i\rangle$ after the excitation will be the same for all pulse shapes [see Fig. 5.2(c)]. However, it should be mentioned that one-photon coherent control is still controversially discussed as can be seen from [167–169].

5.1.3. One-photon coherent control with a pulse sequence

Despite the fact that the original work on coherent control necessarily required a multiphoton transition, a different kind of experiments has been termed *coherent control* as well throughout a number of publications in the past. It has been first presented by Planken *et al.* [170] as well as Heberle *et al.* [41] in semiconductor quantum well systems.

This temporal coherent control scheme requires a sequence of ultrashort laser pulses which are phase-locked with respect to each other [see Fig. 5.3(a)]. The first pulse in the series excites the system, i.e., quantum well excitons in Ref. [41], which has to maintain its coherence for a sufficiently long time. Dependent on the exact time delay between the two pulses, the second pulse either interferes constructively or destructively with the coherent exciton polarization, leading to either additional excitation or a destruction of the polarization. Hence, the aim of this technique is different from the traditional coherent control experiments where a final outcome of the system is desired. Rather,

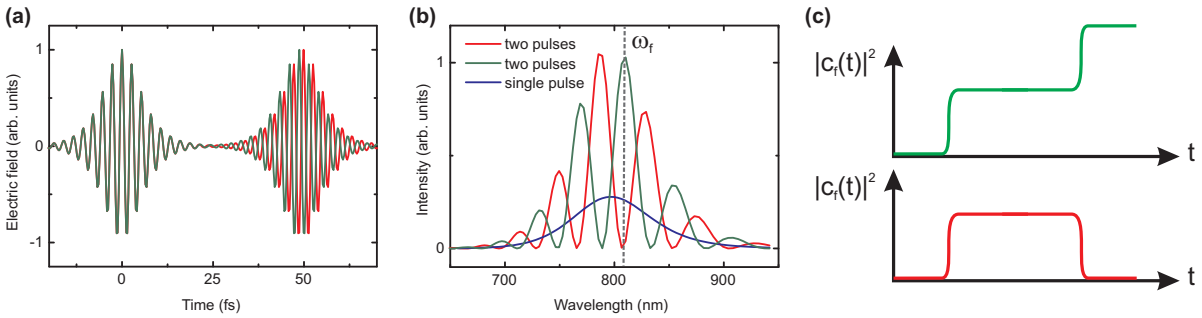

Figure 5.3.: (a) Pulse pair having an even (red) and odd (green) multiple of π as phase difference. (b) In the spectral domain the pulse pair leads to interference fringes while the fringe position depends on the temporal phase difference of the two pulses. The spectrum of a single pulse is smooth (blue). (c) A transition which is resonant to ω_f can be either excited in the constructive case (green) or excited and subsequently de-excited in the destructive case (red).

the temporal evolution of the system, i.e., being turned on or off after the excitation, is object of the control process.

In contrast to the two-photon coherent control experiments, it is not the spectral phase but the temporal phase between the pulses which influences the outcome of the system. A variation of the temporal phase necessarily leads to a variation in the spectral intensity of the pulse pair. This can be understood from Fig. 5.3(b). In the spectral domain a single light pulse with a temporal Gaussian shape has a Gaussian shaped intensity distribution as well (blue). A pulse sequence, however, leads to a Gaussian spectrum which is superimposed by spectral fringes, i.e., local maxima and minima. The spectral fringe position is a direct consequence of the temporal phase between the pulses. For the pulse configuration in Fig. 5.3(a) which is shown in red, the spectrum has a local minimum at a certain frequency ω_f and a maximum for the pulse configuration which is shown in green. If the pulse sequence is considered in the (time integrated) spectral domain alone, the destructive case (red) could be interpreted as a situation where a transition at ω_f is not excited at all since the spectral intensity is zero. In that way, the final outcome could be achieved as well by turning a *cw*-laser at ω_f either on or off.

However, in the temporal domain, the destructive case is different from not exciting the system. Figure 5.3(c) visualizes the probability $|c_f|^2$ of the system to be in the excited state for the constructive and the destructive case. In the constructive case (green), $|c_f|^2$ increases after the first pulse and grows again after the second pulse. In the destructive case (red) it increases after the first pulse but drops to zero after the second pulse. Thus, the system is indeed excited for a short period of time in the destructive case. In order to verify the excitation and de-excitation of the system, a temporal resolution of the coherent control process is mandatory. So far, this has usually been accomplished

by a third pulse which probes the system at every time step throughout the control process [41].

In the past, the pulse sequence coherent control concept has been utilized in several systems such as electrons in metals [90], LO-phonons in GaAs [171], phonons in photonic crystal fibers [172], and recently on spin waves [173]. Concerning energy conservation, it has been shown in an experiment by Yee *et al.* that the energy of the system is transfered to the second pulse in the destructive case [174].

5.1.4. Coherent control in plasmonic systems

The concept of coherent control has been introduced in plasmonics by Stockman *et al.* [142, 175–177]. The authors theoretical investigated a V-shaped plasmonic nanostructure upon excitation by chirped laser pulses [see Fig. 5.4(a)]. For example, for a negatively chirped pulse it could be shown that the field concentrates at various positions in the nanostructure for different time steps. If the pulse was positively chirped, the temporal evolution of the field concentration completely changed. Therefore, by applying an appropriate chirp, i.e., spectral phase, of the pulse, the field enhancement one the nanoscale could be controlled in the V-shape tip. Additionally, the authors showed that the same concept also works for a random plasmonic structure. Here, the field concentration at a certain location was not simply due to the specific structure [178] but rather due to the pulse shape.

However, for an experimental approach the ideal pulse shape for a certain near field distribution in the nanostructure is not known in advance. Stockman *et al.* proposed an intriguing method which is based on time reversal [179]: The pulse shape that is necessary to concentrate the electric field to a specific location in a random nanostructure, is uniquely related to that location. If a dipole source would be placed at that location, it would lead via the coupling to the nanostructure to a certain pulse shape in the far field. Consequently, if this pulse is reversed in time and incident to the structure, it would lead to the concentration of the electric field at the desired location. However, in an experiment this method is still challenging and other approaches have been utilized so far.

The first experiment regarding temporal coherent control in plasmonic systems has been performed by Kubo *et al.* [180]. In the experiment a nanostructured silver surface was illuminated by a sequence of two 10 fs laser pulses [see Fig. 5.4(b)]. Due to the surface roughness SPP were launched and led to localized plasmons (hot spots) at certain locations in the film. These hot spots were imaged by two-photon photoemission electron microscopy (PEEM) as a function of the time delay between the pulses. Here, two photons of the incident light generate a free electron which is accelerated in an inverse electron microscope to a detector. From the spatial electron distribution at the detector,

an image of the nanostructure is obtained while larger local fields in the nanostructure lead to a stronger signal at the detector. As a result, it was observed that some hot spots lit up for certain delays and became dark for other delays. Thus, it was possible to excite localized plasmons by the first pulse and subsequently turn them down by the second pulse. However, this experiment did not provide a temporal resolution such as in the pulse sequence coherent control experiments [41], therefore the evolution of the excitation could not be mapped.

A few years later, a much more sophisticated approach has been demonstrated by a collaboration of research groups around Aeschlimann *et al.* [181]. Similar to the suggestions by Stockman they used pulse shaping to spatially control the optical near field in a star-shaped nanostructure [see Fig. 5.4(c)]. The structure was excited by a short laser pulse and a two-photon PEEM image of the structure was recorded, similar to the experiment by Kubo. By using a pulse shaper, arbitrary pulses could be generated. Still, the pulse shape for a certain spatial near field distribution in the structure was not known in advance. However, by applying a genetic algorithm with a feedback, the pulse shape was improved step by step until a desired near field distribution in the nanostructure was achieved.

The reason why this concept works successfully lies in the different orientations of the electric field components in the far field and in the near field. If in the far field one electric field component $\mathbf{E}_1$ points in the x-direction and another one, $\mathbf{E}_2$, in y-direction, they cannot interfere:

$$I = (\mathbf{E}_1) + \mathbf{E}_2))^2 = (\mathbf{E}_1)^2 + (\mathbf{E}_2)^2. \tag{5.1}$$

However, the corresponding field components in the near field $\mathbf{E}_1^{NF}(\mathbf{r}), \mathbf{E}_2^{NF}(\mathbf{r})$ do not have to point in the same directions as in the far field. This leads to interference of the components in the near field:

$$I(\mathbf{r}) = (\mathbf{E}_1^{NF})^2 + (\mathbf{E}_2^{NF})^2 + 2\mathbf{E}_1^{NF} \cdot \mathbf{E}_2^{NF} \tag{5.2}$$

Due to the interference terms, $I(\mathbf{r})$ can be controlled via the phase between $\mathbf{E}_1$ and $\mathbf{E}_2$.

The genetic algorithm method is a sufficient way to determine the necessary pulse shape for a desired field enhancement in the nanostructure, however, the experiment requires a huge effort. Recently, even the first steps towards spatial *and* temporal control have been suggested [182].

5.2. All-optical control concept

In this work the coherent control concept, which is based on a laser pulse sequence excitation, is utilized for a hybrid plasmonic system. In order to avoid confusion with other

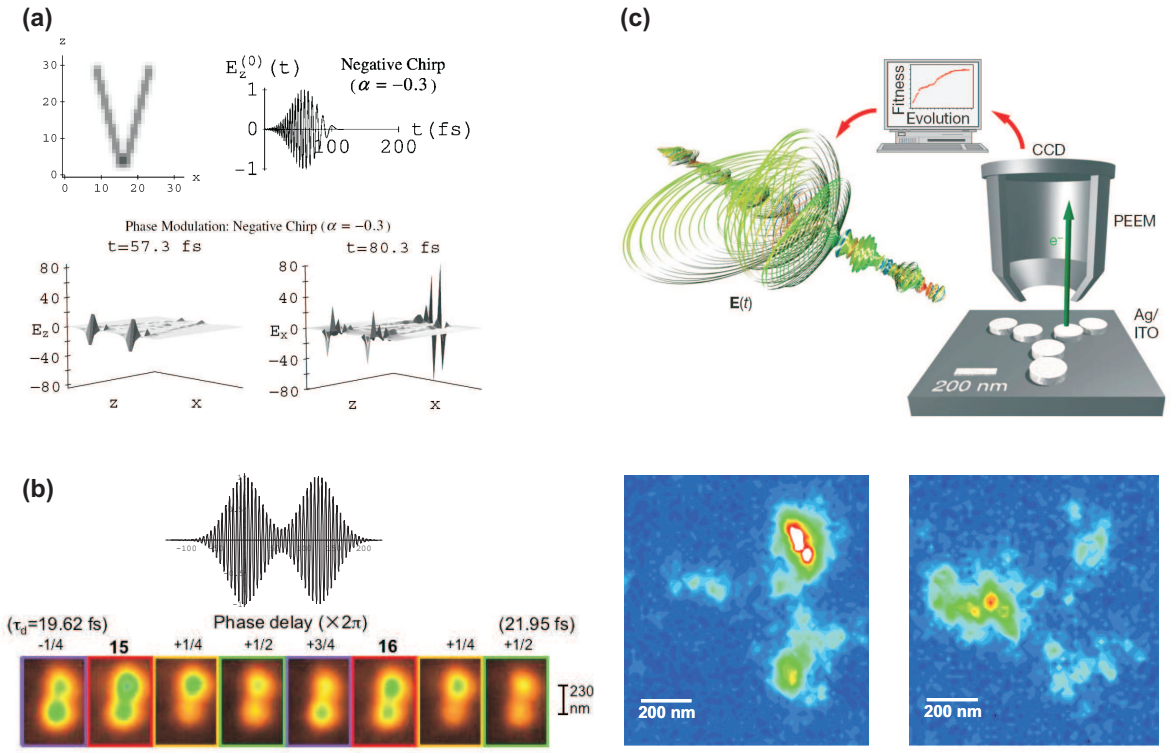

Figure 5.4.: Variety of simulations and experiments concerning coherent control on the nanoscale. (a) Coherent control in a V-shaped nanostructure via chirped laser pulses (from [142]). (b) Coherent control of localized surface plasmons using a pulse sequence (from [180]). (c) Adaptive sub wavelength control of the field enhancement in a plasmonic nanostructure (from [181]).

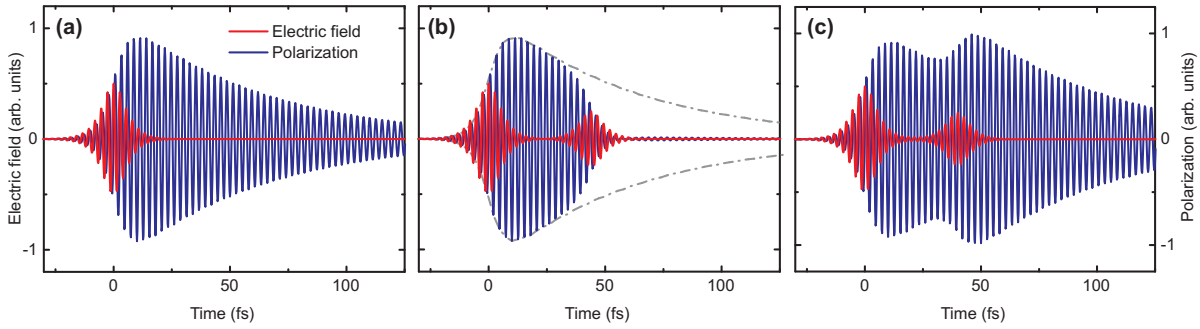

Figure 5.5.: Simulation of the local polariton polarization excited by a first 8 fs laser pulse and controlled by a second delayed pulse. (a) Without the second pulse the polariton polarization follows a free polarization decay (T_2=50 fs). (b) The second pulse interferes destructively with the polariton polarization and turns it off (destructive case). Therefore the polariton polarization is well below the free polarization decay (dashed line). (c) The second pulse interferes constructively with the polariton polarization and reexcites it.

coherent control techniques, the term *all-optical control* will be used in the following. For this technique it is required that the system under control maintains its coherence on a larger time scale as the pulse duration. Otherwise the excitation cannot be controlled by a second pulse. In Ref. [41] pulse duration and pulse delay were in the sub-picosecond range while the coherence time of the excitons was several picoseconds. In a plasmonic system, however, this requirement is a major challenge due to the short dephasing times of pure PPP on the order of a few femtoseconds. Even with ultrashort laser pulses it would be hardly possible to utilize the pulse sequence coherent control technique.

However, this problem can be circumvented by employing the hybridization of PPP with photonic waveguide modes. It has been shown in chapter 3 that dephasing times up to several tens of femtoseconds are obtained for the WPP eigenmodes. Figure 5.5(a) shows a simulation which is based on the harmonic oscillator model (chapter 3.1.4). A single oscillator with a dephasing time of $T_2 = 50$ fs which is resonantly driven by a single 8 fs laser pulse is considered. Together with the electric field of the laser pulse the polariton polarization grows in time. When the electric field is already decreasing after a few oscillations of the electric field, the polariton polarization still grows since energy is further transfered from the pulse to the system. After the pulse is gone, the polariton polarization follows a free polarization decay and the envelope of the polariton polarization oscillation decreases exponentially. For a dephasing time of 50 fs the polariton polarization amplitude is still present even 150 fs after the laser pulse. This temporal window should be sufficient to impose the control with a second pulse on the system.

For the all-optical control scheme two scenarios are distinguished again. The first one is the destructive case where the second pulse (control pulse) turns the polariton polariza-

tion completely down. In Fig. 5.5(b) the control pulse maximum is at a delay of 44 fs. As soon as the electric field of the control pulse starts to increase, the polariton polarization drops faster than in the free polarization decay. After the control pulse the polariton polarization is zero. In the destructive case it is very important that the amplitude of the control pulse is attenuated. If the amplitude was too large, the polariton polarization would be completely turned down before the electric field of the control pulse is zero. The remaining electric field would enhance the polariton polarization again.

The second scenario is the constructive case, where the control pulse reexcites the slowly decaying polariton polarization [see Fig. 5.5(b)]. The delay with respect to the start pulse is slightly changed and the polariton polarization increases when the electric field of the control pulse starts to build up. After the control pulse the polariton polarization amplitude is now even higher than in the free polarization decay. After the control pulse has transfered its energy to the polariton polarization, the polarization starts to decay again but at later times than before.

In this manner, the second pulse imposes the control on the polariton polarization. As stated before, additionally to the pulse sequence, a method has to be employed which delivers the time resolution throughout the control process. In the present experimental approach, the temporal resolution is provided by a third laser pulse (probe pulse) with variable delay, which interacts as well with the polariton polarization in the system in a nonlinear fashion. Here, the nonlinearity of the plasmonic system is utilized again. Before discussing the nonlinear mixing, the experimental setup is explained in detail.

5.3. Experimental setup

For the all-optical control experiments the experimental setup which has been discussed in chapter 3 is further extended. Here, the two pulses from the Michelson interferometer serve as start and control pulse with a temporal delay τ_c. From the simulations it has been found that the control pulse has to be slightly attenuated in order to achieve complete suppression of the polariton polarization in the destructive case. The only possibility to vary the amplitudes of the pulses separately is within the two interferometer arms where the pulses are spatially separated. The dispersion which is imposed by the attenuators, should be as low as possible. Therefore, a pair of ultra thin (200 μm) sheet polarizers is used in the interferometer arm of the control pulse for the attenuation. The first polarizer is rotated in order to reduce the transmitted intensity and the second one retains the polarization. In order to introduce the same amount of dispersion for both pulses, another pair of sheet polarizers is mounted in the beam path of the start pulse while the rotation is set to perfect transmission.

In the experiment, it turned out that a rotation of the sheet polarizers can lead to a

small beam walk-off and a realignment of the interferometer is necessary. Unfortunately, this prevents a continuous variation of the control pulse amplitude. It has been carefully verified in the setup that the light of the He:Ne laser within the interferometer arms is not affected by the polarizers.

The all-optical control experiments require a third laser pulse which serves as the probe pulse. In order to separate the probe pulse from the original laser pulse, an ultra thin beam splitter (d = 500 μm) is used in front of the Michelson interferometer. The beam splitter has a reflection to transmission ratio of 25:75. Thus, the probe pulse finally has approximately the same amplitude as the start pulse. First, the probe pulse passes a piece of glass which provides the same dispersion as the beam splitters for start and control pulse. Following that, the probe pulses follows a delay line which sets the temporal delay τ_p with respect to the start pulse. This delay is not actively stabilized, therefore the temporal resolution is smaller than for τ_c. However, it turns out that the resolution of the piezo actuator of the delay line (*Physikinstrumente, NanoCube*) of 1 nm is sufficient for a passive stabilization of the delay. The piezo actuator has a travel range of 100 μm which leads to a temporal delay range of 333 fs.

Figure 5.6(a) shows a picture of the pulse preparation part of the experimental setup. The Michelson interferometer is located in the lower part of the image. The interferometer arm in the vertical direction provides the start pulse while the control pulse passes the horizontal interferometer arm including the piezo actuator. The sheet polarizer attenuator is not shown here. The upper part includes the delay line for the probe pulse with the retro reflector mirror which is mounted on the *NanoCube* piezo actuator. The other optical components are used for the interferometer stabilization with the He:Ne laser.

The probe pulse is finally guided to the sample with a parallel offset of 5 mm below the start/control beam. This configuration enables to selectively modulate the two beams using chopper wheels and a separation of the nonlinear signal behind the sample. Since the two beams are parallel in front of the spherical mirror, their foci overlap at the same point on the sample. However, in oder to allow for fine adjustment, both beams hit separate mirrors in front of the spherical mirror and a perfect spatial overlap of the beams on the sample can be guaranteed.

Figure 5.6(b) shows a schematic of the beam configuration. The start/control beam is incident normal to the sample. The probe beam is aligned at a small angle of $\varphi = 3°$. The light polarization is horizontal and the orientation of the wires is vertical in order to excite the WPP modes in TM polarization. Since the tilt of the probe beam is along the wires, the antisymmetric waveguide mode is not excited if φ is small.

In order to probe the polariton polarization in the sample with the third pulse, the electric fields have to be mixed in a nonlinear fashion. Just like in the ACF measurements, the metallic photonic crystal structures serve as the nonlinear medium itself. Due to the

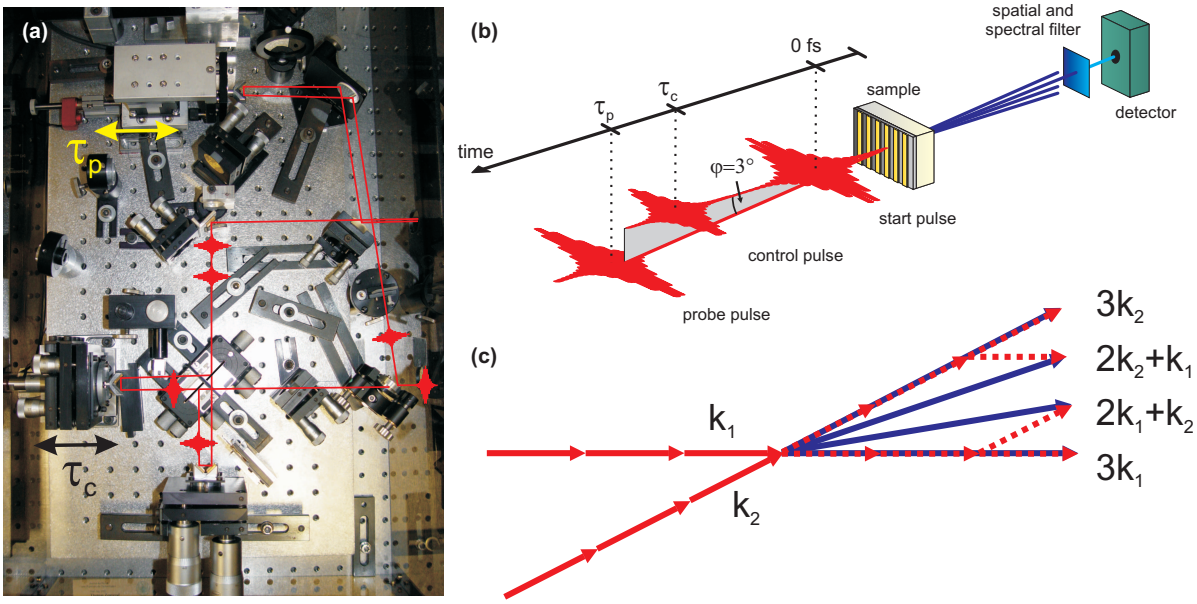

Figure 5.6.: (a) Image of the pulse preparation part in the experimental setup showing the Michelson interferometer (bottom) and the delay path for the probe pulse (top). (b) Schematic of the control setup. The start pulse excites the polariton polarization and the control pulse interferes with it after the delay τ_c. The pulses are aligned with normal incidence to the sample and the electric field is polarized perpendicular to the wires. (c) In the third-harmonic regime, photons of each pulse (wave vector $\mathbf{k}_1$ and $\mathbf{k}_2$) generate higher harmonic photons in their forward directions ($3\mathbf{k}_1$ and $3\mathbf{k}_2$) and signals in the directions $2\mathbf{k}_1 + \mathbf{k}_2$ and $2\mathbf{k}_2 + \mathbf{k}_1$.

oblique incidence of the probe pulse beam, several components at the third-harmonic can be spatially distinguished behind the sample [see Fig. 5.6(c)]. The nonlinear polarization can be written in general as

$$\tilde{\mathbf{P}}^{(3)}(\mathbf{r},t) = \epsilon_0 \chi^{(3)} \tilde{\mathbf{E}}^3(\mathbf{r},t) \tag{5.3}$$

with

$$\tilde{\mathbf{E}}(\mathbf{r},t) = E_1 e^{-(\omega t + \mathbf{k}_1 \mathbf{r})} + E_2 e^{-(\omega t + \mathbf{k}_2 \mathbf{r})} + c.c., \tag{5.4}$$

where the two electric fields have the same frequency ω but different wave vectors $\mathbf{k}$. When calculating $\tilde{\mathbf{P}}^{(3)}(\mathbf{r},t)$, several terms appear with different wave vector combinations such as

$$\begin{aligned} P(3\mathbf{k}_1) &= \epsilon_0 \chi^{(3)} E_1^3 \\ P(3\mathbf{k}_2) &= \epsilon_0 \chi^{(3)} E_2^3 \\ P(2\mathbf{k}_1 + \mathbf{k}_2) &= 3\epsilon_0 \chi^{(3)} E_1^2 E_2 \\ P(2\mathbf{k}_2 + \mathbf{k}_1) &= 3\epsilon_0 \chi^{(3)} E_1 E_2^2 \\ &\dots . \end{aligned} \tag{5.5}$$

Further terms will be discussed in the last section of this chapter. The four contributions in Eq. 5.5 are indeed found in the experiment behind the sample and are interpreted as follows: The start/control beam (with wave vector $\mathbf{k}_1$) generates light at the third-harmonic in its forward direction ($3\mathbf{k}_1$). The same holds true for the probe beam ($3\mathbf{k}_2$). However, there are also two additional components. The first one incorporates two photons of the start/control beam and one photon of the probe beam. The resulting nonlinear signal ($2\mathbf{k}_1 + \mathbf{k}_2$) is found inbetween $3\mathbf{k}_1$ and $3\mathbf{k}_2$. The second one refers to the opposite case where one photon of the start/control beam and two photons of the probe beam generate the third-harmonic signal ($2\mathbf{k}_2 + \mathbf{k}_1$). The two components in the middle are the interesting ones for the experiment since they originate from a nonlinear mixing of the beams. By using an iris diaphragm in front of the prism sequence, one of the four THG components can be selected for detection. However, since the angle φ has to be very small, the nonlinear signals might slightly overlap behind the sample. For example, when detecting the signal in the direction $2\mathbf{k}_2 + \mathbf{k}_1$, contributions from the $3\mathbf{k}_2$ and the $2\mathbf{k}_1 + \mathbf{k}_2$ might influence the results. In order to suppress the signal in the direction $3\mathbf{k}_2$, a lock-in technique is applied were only the start/control beam is periodically modulated with an optical chopper wheel at ≈ 550 Hz. The modulation is conveyed to all nonlinear signals which incorporate a $\mathbf{k}_1$ photon. Thus, the detection is not sensitive to the THG signal in the direction $3\mathbf{k}_2$. However, the $2\mathbf{k}_2 + \mathbf{k}_1$ signal might still be disturbed by the $2\mathbf{k}_1 + \mathbf{k}_2$. It will turn out that this interference leads to interesting effects in the final results revealing a pseudo-phase of the polariton polarization oscillation.

When using the metallic photonic crystal structures, the temporal pulse overlap of the laser pulses is not the only possibility in order to generate a THG signals in the directions $2\mathbf{k}_2 + \mathbf{k}_1$ and $2\mathbf{k}_1 + \mathbf{k}_2$. As in the ACF measurements, the polariton polarization in the sample imposed by the three pulses has to be considered as well. To understand the signal generation, e.g., in the direction $2\mathbf{k}_2 + \mathbf{k}_1$, different pulse and delay configurations are discussed now separately.

In the first steps, the control pulse is neglected. Figure 5.7(a) shows on the one hand a schematic of the start pulse together with the polariton polarization which is generated in the sample. The probe pulse, on the other hand, generates a polariton polarization itself which follows the pulse on the time axis. The start pulse and the subsequent polariton polarization have the wave vector $\mathbf{k}_1$ while the probe pulse together with the subsequent polariton polarization has the wave vector $\mathbf{k}_2$. In Fig. 5.7(a) the probe pulse does not temporarily overlap with the start pulse but with the $\mathbf{k}_1$-polarization. Therefore, the $2\mathbf{k}_2 + \mathbf{k}_1$ THG signal is present. In Fig. 5.7(b) the delay between the pulses is reversed in time and the probe pulse arrives first. The $2\mathbf{k}_2 + \mathbf{k}_1$-signal is again present, but with lower intensity, since the two directions contribute differently. In Fig. 5.7(c), the delay is very large and the probe pulse does not temporarily overlap with the $\mathbf{k}_1$-polarization. Therefore the THG signal is zero.

Now the control pulse is included. Figure 5.7(d) shows the destructive case where the $\mathbf{k}_1$-polarization is turned down by the probe pulse. The probe pulse arrives after the control pulse, thus the THG signal is zero. In the constructive case [see Fig. 5.7(e)], the $\mathbf{k}_1$-polarization is reexcited by the control pulse and the THG signal is present. Finally, in Fig. 5.7(f) τ_p is reversed. The THG signal is present but it is again weaker due to the wave vector asymmetry in $2\mathbf{k}_2 + \mathbf{k}_1$.

Figures 5.7(d) and 5.7(e) clearly show that it is possible by utilizing the probe pulse to distinguish between the destructive and the constructive case. Thus the control experiment can be performed in two fashions. In the first one, the probe pulse delay is fixed to a value which is larger than τ_c and the control pulse delay is continuously varied. Therefore the configuration will alter between the cases in Fig. 5.7(d) and 5.7(e). However, this configuration does not provide the necessary temporal resolution of the control process or in other words the polariton polarization inbetween start and control pulse.

In a more sophisticated fashion, the control pulse delay is fixed to either the destructive case [Fig. 5.7(d)] or the constructive case [Fig. 5.7(e)] and the probe pulse delay is varied from negative to positive values. In this manner, the presence of the $\mathbf{k}_1$-polarization can as well be confirmed inbetween start and control pulse.

5.4. Experimental results

5.4.1. Sample selection

For optimum all-optical control results, a metallic photonic crystal structure with a particular linear response is necessary. First, one of the WPP modes should be rather

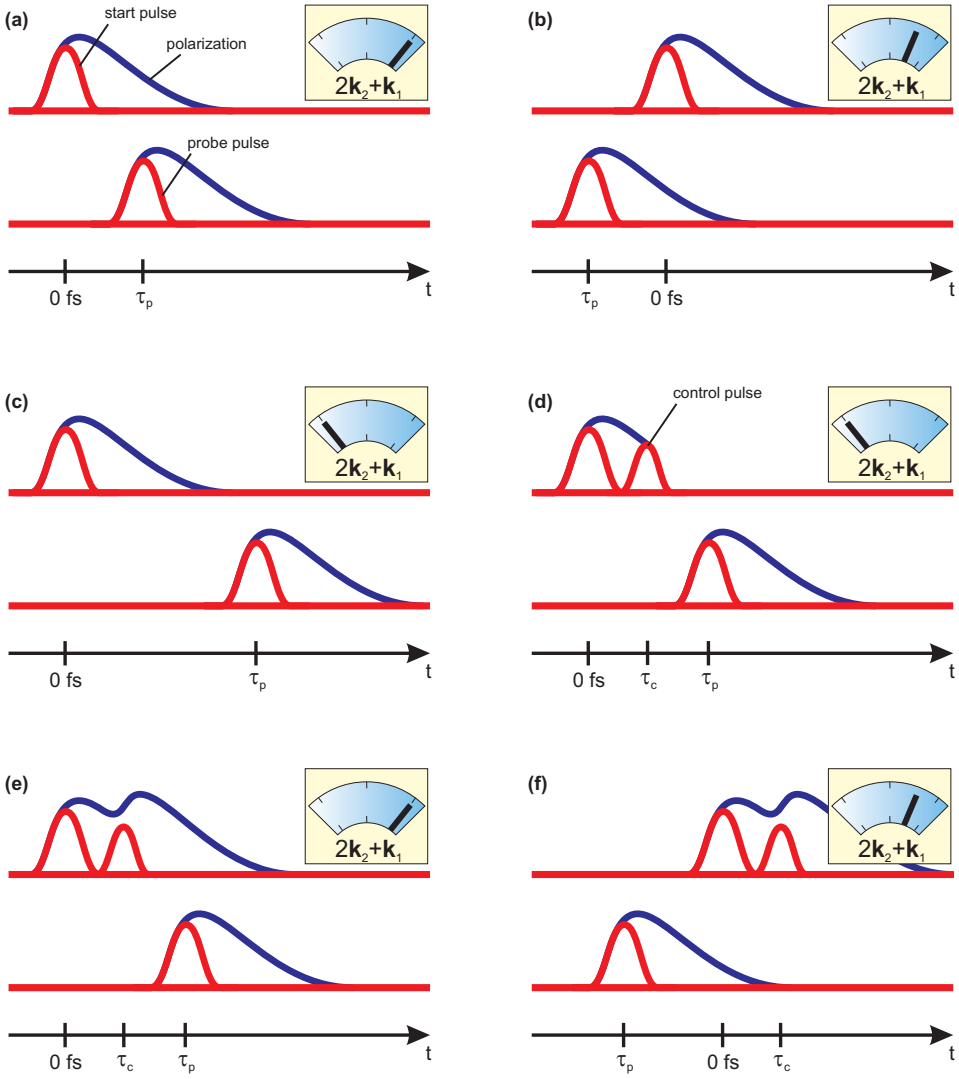

Figure 5.7.: Schematics of different pulse and delay configurations leading to a small or large THG signal in the direction $2\mathbf{k}_2 + \mathbf{k}_1$.

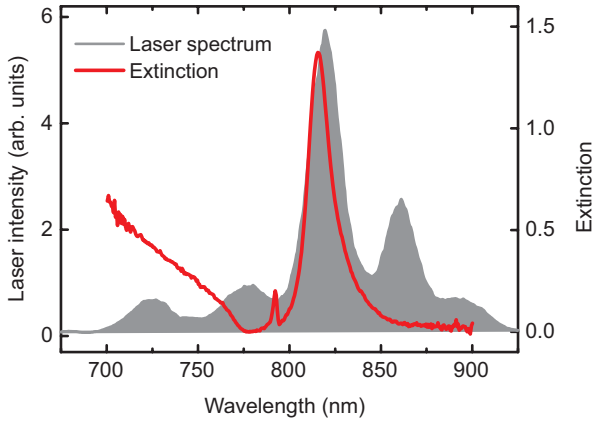

Figure 5.8.: Extinction spectrum of the metallic photonic crystal structure together with the laser spectrum showing that mainly the narrow WPP mode is excited by the laser.

narrow in order to obtain large dephasing times. Second, this WPP mode should be effectively excited by the laser while the other one should not be excited. Figure 5.8 shows the extinction spectrum of a sample which renders ideal for the experiment. The same sample has been used before in order to introduce the nonlinear ACF (see Fig. 3.4). Here, the extinction is directly measured with the broad laser spectrum. The long-wavelength WPP mode at 825 nm fits nicely to the main peak of the laser spectrum and the linewidth is only about 20 nm. The other WPP mode at 685 nm is hardly excited by the broad laser spectrum. The small peak in the extinction at 792 nm can be related to the antisymmetric waveguide mode. Due to the focusing of the laser beams, its appearance cannot be suppressed completely. However, it turns out that this mode has very little oscillator strength such that it does not influence the all-optical control experiments.

The present sample consists of a 180 nm thick hafnium dioxide HfO_2 waveguide on a quartz substrate. The refractive index of HfO_2 is $n = 1.89$. It turns out that the HfO_2 slab generates negligible THG. Therefore, in accordance to chapter 4, the THG spectrum has the same shape as the linear extinction spectrum. The gold grating on top of the waveguide has a period of 530 nm and the wire cross-section is 100×20 nm^2.

From the shape and the linewidth of the WPP mode at 825 nm it can be assumed that sufficient plasmonic character is maintained in the resonance since the resonance has a different shape than in TE polarization. The presence of the THG signal, which only originates from the PPP in this sample, confirms the plasmonic contribution to the WPP mode. In comparison, no THG signal could be measured in TE polarization.

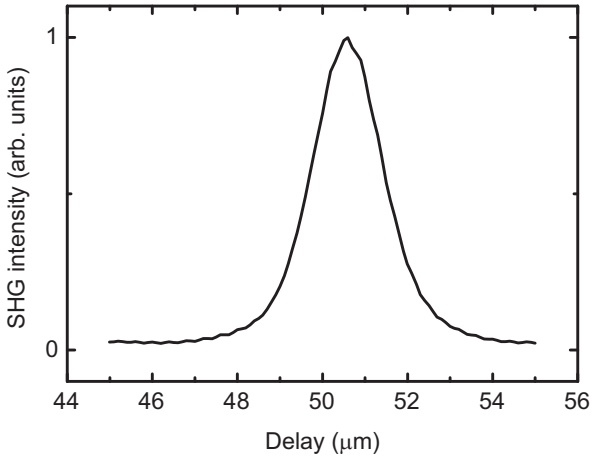

Figure 5.9.: Cross correlation measured at a BBO crystal to calibrate the time delay τ_p between start and probe pulse.

5.4.2. Preparing the experiment

In order to prepare the experimental setup, the two pulse delays have to be calibrated first. The $\tau_c = 0$ position is easily found by maximizing the THG signal in the direction $3\mathbf{k}_2$. For the delay τ_p a BBO crystal is placed at the position of the sample and the control pulse is blocked. If start and probe pulse do not temporally overlap, there are only two SHG spots behind the BBO crystal, i.e., in the directions $2\mathbf{k}_1$ and $2\mathbf{k}_2$. Now the probe pulse delay τ_p is shifted by moving the piezo actuator until a third SHG spot inbetween the others, i.e., in the direction $\mathbf{k}_1 + \mathbf{k}_2$, is observable. Figure 5.9 shows this SHG signal as a function of the piezo displacement. In the present example, the $\tau_p = 0$ position is found for a displacement of 51.5 μm. To improve the symmetry of the curve, the spatial overlap of the two beams on the sample is optimized. The figure indicates that the overlap range is only on the order of a few micrometers due to the short pulse duration. Thus, the length of the probe pulse beam paths has to match the length of the other path nearly perfectly in advance.

After calibrating the delays, the control pulse has to be attenuated in order to achieve complete suppression of the signal in the destructive case. Since the rotation of the attenuating sheet polarizer affects the alignment of the Michelson interferometer, a single attenuation is chosen for the following experiments where the control pulse possesses 60% of the average power of the start pulse.

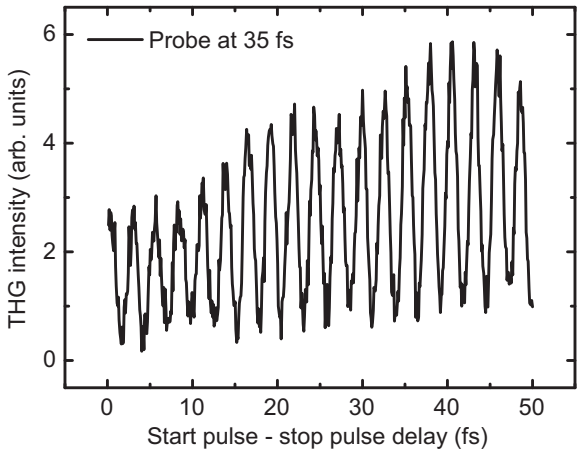

Figure 5.10.: THG signal in the direction $2\mathbf{k}_2 + \mathbf{k}_1$ measured at a metallic photonic crystal as a function of the time delay between start and control pulse. The probe pulse is set to 35 fs. The oscillations in the signal correspond to alternating destructive (minimum) and constructive (maximum) cases.

5.4.3. All-optical control with variable control pulse delay

The all-optical control configuration with variable control pulse delay will only be discussed shortly since the temporal resolution of the control process is lacking.

Figure 5.10 show an experimental result. The probe pulse delay is fixed to $\tau_p = 35$ fs and the THG signal in the direction $2\mathbf{k}_2+\mathbf{k}_1$ is plotted as a function of the delay between start and control pulse. One observes a periodic interference pattern. For small delays τ_c this pattern is a result of the destructive and constructive interference of start and control pulse. For larger delays the minima in the THG signal correspond to the destructive case where the control pulse has turned the polariton polarization down [compare Fig. 5.5(b) and Fig. 5.7(d)]. For increasing delay τ_c the configuration changes to the constructive case where the polariton polarization is reexcited [compare Fig. 5.5(c) and Fig. 5.7(e)].

One can show that a comparable result has already been achieved with the nonlinear ACF. For delays much larger than the pulse duration the local minima in the ACF correspond to the destructive case as well, while the local maxima correspond to the constructive case. However, there is no temporal resolution and the evolution of the polariton polarization throughout the control process cannot be monitored in this configuration. Additionally, since both pulses have the same amplitude in the ACF measurements, no complete destruction is achieved.

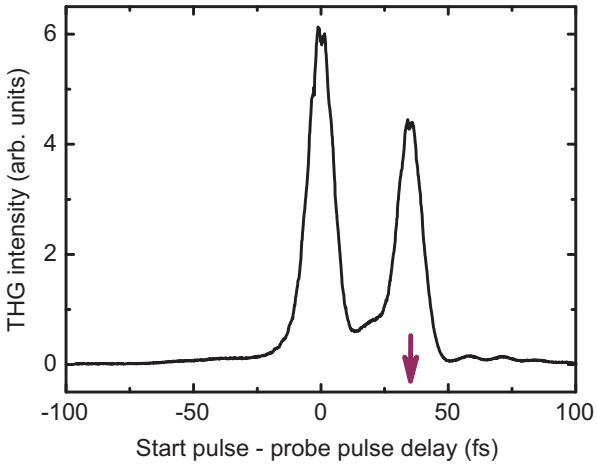

Figure 5.11.: THG signal measured at an ITO layer as a function of the time delay between start and probe pulse. The position of the control pulse is indicated by the arrow. There is only a signal present if the probe pulse either overlaps temporally with the start or with the control pulse. From the different amplitudes it is obvious that the control pulse is attenuated.

5.4.4. All-optical control with variable probe pulse delay

The other approach to perform the all-optical control experiment is achieved by continuously varying the probe pulse delay τ_p while setting the control pulse delay τ_c either for the destructive or the constructive case [183]. In a first experimental step the ITO layer is used instead of the metallic photonic crystal structure in order to provide a better understanding of the shape of the THG signal. Since ITO provides an instantaneous nonlinear response to the excitation, there should only be a THG signal in the direction $2\mathbf{k}_1 + \mathbf{k}_2$ and $2\mathbf{k}_2 + \mathbf{k}_1$ if the probe pulse either overlaps temporally with the start or with the control pulse. Figure 5.11 shows the result when the control pulse delay is set to $\tau_c = 35$ fs. Two THG peaks are observable in the figure. The first one is at $\tau_p = 0$ and corresponds to the temporal overlap of the probe pulse with the start pulse. The second peak is at $\tau_p = 35$ fs and corresponds to the temporal overlap of probe and control pulse. Due to the attenuation of the control pulse, the second peak is smaller in amplitude. The small peaks for larger delays are again a consequence of the laser satellite pulses. Since start and control pulse do not temporally overlap, there is no difference in the THG signal if the control pulse is slightly shifted and the destructive case cannot be distinguished from the constructive case.

The results drastically change if the metallic photonic crystal structure is used instead of the ITO layer. For the following experiments three control pulse delays are chosen. Figure 5.12 shows the delay positions with the help of the nonlinear ACF which has been measured at this particular sample. As mentioned before, local minima in the ACF correspond to the destructive case (red line) and local maxima correspond to the

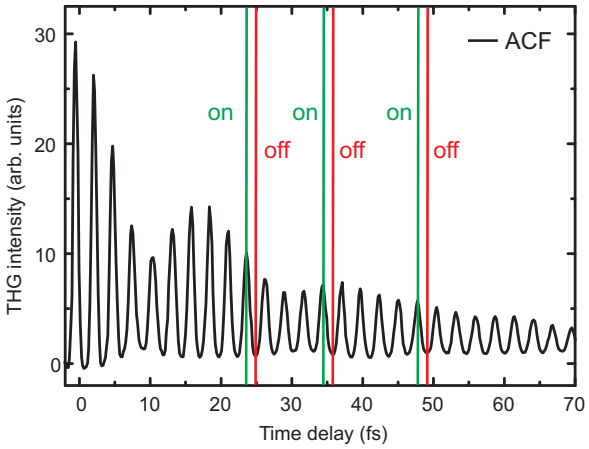

Figure 5.12.: THG autocorrelation function measured on the sample together with the six delay positions for the control experiments shown in Figure 5.13 and 5.14. The constructive case (green line) always corresponds to a local maximum in the autocorrelation and the destructive case (red line) to a local minimum.

constructive case (green line). The three delays are around 24 fs, 35 fs, and 48 fs, respectively.

Figure 5.13 shows the results of the control experiment. In the first step the control pulse is blocked, hence only start and probe pulse act on the WPP mode. The blue curve in Fig. 5.13(a) shows the THG signal for the free polarization decay. It is maximum for $\tau_p = 0$ where the pulses overlap perfectly. Due to the polariton polarization, the signal drops rather slowly with increasing delay τ_p. The signal is also present for negative delays due to the polariton polarization which is excited by the probe pulse. However, as discussed in Fig. 5.7(a) and 5.7(b), the signal is not symmetric around $\tau_p = 0$ due to the asymmetric contribution of the beams to the THG signal.

The red curve corresponds to the destructive case. For negative delays τ_p up to the position of the control pulse it has the same shape as in the free polarization decay. However, after the control pulse, the signal drastically drops and is nearly zero. As predicted in Fig. 5.7(d), the control pulse has turned the polariton polarization down and the THG signal cannot be generated if $\tau_p > \tau_c$.

For the constructive case, the control pulse is slightly shifted and the green curve is measured. After the control pulse the THG signal is drastically increased and lasts for larger delays than in the free polarization decay. It is worth noting that the amplitude of the THG signal at $\tau_p = 0$ differs in the three cases. This is a consequence of the temporal integration of the THG signal for each delay step at the detector. In the constructive case the integrated polariton polarization is larger than in the destructive case which

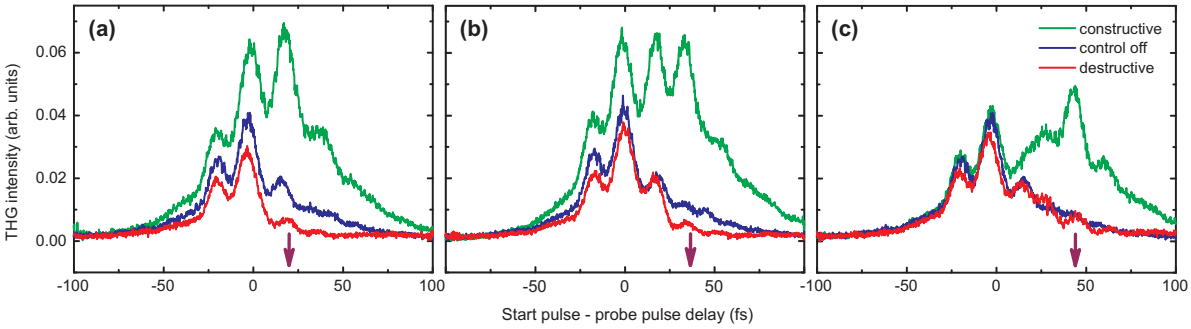

Figure 5.13.: (a)-(c) Experimental results of the coherent nonlinear signal in the direction $2\mathbf{k}_2 + \mathbf{k}_1$ as a function of the time delay τ_p between start and probe pulse for three different delays of the control pulse (τ_c ≈24 fs, 35 fs, and 48 fs, marked by the arrows). For the blue line, the control pulse is switched off, and the free polarization decay of the hybrid mode is visible. The red line always indicates the destructive case. The polariton polarization is completely turned off after the control pulse and stays off. The green line shows the constructive case. Here, the polariton polarization is reexcited.

leads to a higher THG amplitude.

Figure 5.13(b) shows the same behavior for a slightly larger delay of $\tau_c = 35$ fs, except that the WPP mode is turned down at a larger delay τ_p. In Fig. 5.13(c) the delay τ_c is further increased to 48 fs. Here, only little difference between the destructive case and the free polarization decay is found since the WPP mode has already nearly completely dephased after 48 fs.

In the experiment it is important to find exactly the right delay in order to achieve complete suppression of the THG signal in the destructive case. To simplify the experiment, the amplitude of the control pulse has not been changed for the three delays. This would, however, improve the contrast of the signals even more.

The results confirm that the polariton polarization can indeed be completely turned on or off at any desired time after its excitation and within the dephasing time of the WPP mode. Together with the linear polariton polarization, the coherent nonlinear response in the directions $2\mathbf{k}_2 + \mathbf{k}_1$ and $2\mathbf{k}_1 + \mathbf{k}_2$ is controlled as well which makes the method suitable for ultrafast plasmonic switching, with mechanisms different from [184].

Due to the small angle between the start/control beam and the probe pulse beam, it is not easy to separate the THG signal in the direction $2\mathbf{k}_2 + \mathbf{k}_1$ from the THG signal in the direction $2\mathbf{k}_1 + \mathbf{k}_2$. However, interference of both signals at the detector leads to an interesting variation in the signal which will be discussed now. Figures 5.14(a)-(c) show a series of measurements comparable to Fig. 5.11 but with a small contribution

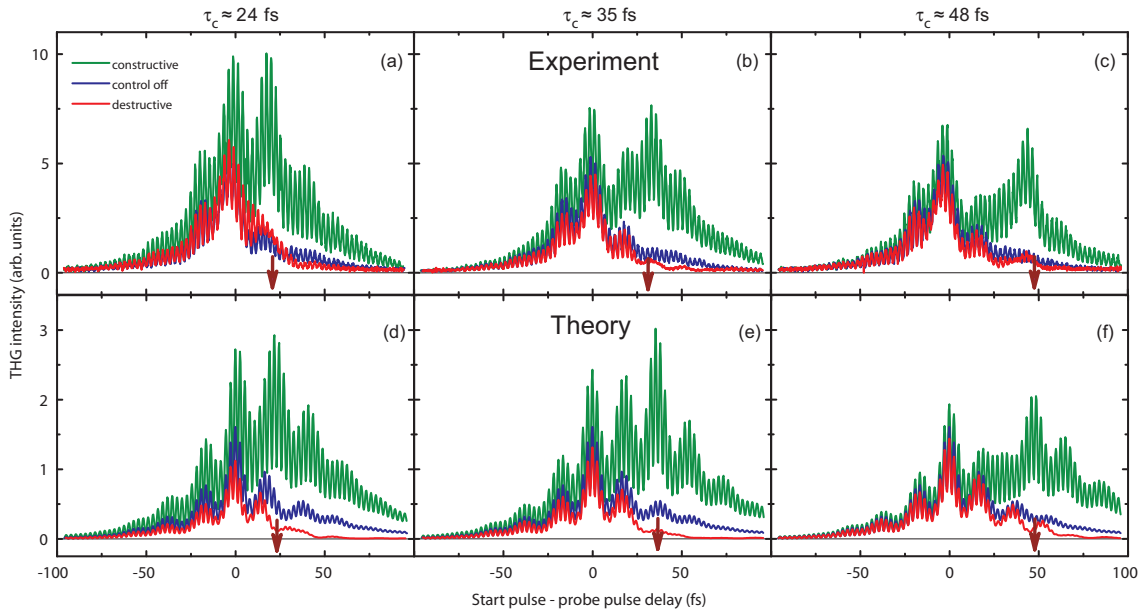

Figure 5.14.: (a)-(c) Results such as in Figure 5.13 but with an admixture of the signal in the direction $2\mathbf{k}_1 + \mathbf{k}_2$ leading to the fast oscillations. (d)-(f) Theoretical results for the coherent nonlinear signal corresponding to panels (a)-(c).

of the THG signal in the direction $2\mathbf{k}_1 + \mathbf{k}_2$. The curves are now superimposed by a fast oscillation which is comparable to the fringe pattern in the interferometric ACF (see Fig. 3.3). Just like the nonlinear ACF, Fig. 5.14(a)-(c) show the THG signal as a function of the delay. Therefore the oscillation should not be mistaken for the oscillation in Fig. 5.5 where the polariton polarization is plotted as a function of time. However, the oscillation in Fig. 5.14(a)-(c) mimic the pseudo-phase of the polariton polarization which oscillates in the sample and gives an intuitive picture of the ultrafast dynamics. For example in Fig. 5.14(b), in the destructive case, the oscillation amplitude decreases rapidly together with the envelope of the THG signal after the control pulse has arrived. No oscillations are observable for larger delays. On the contrary in the constructive case, the oscillation amplitude increases after the control pulse. For different delays τ_c the THG signals show a similar behavior as in Fig. 5.13, especially for $\tau_c = 48$ fs the difference between the free polarization decay and the destructive case is rather small.

In the following section, the harmonic oscillator model is employed again in order to investigate the THG signals in all details.

5.5. Harmonic-oscillator-based simulations

The harmonic oscillator model, which has been used to describe the nonlinear ACF of metallic photonic crystals in chapter 3.1.4 will be expanded now in order to understand the results of the all-optical control measurements. Previously, the local electric field in the vicinity of the nanostructure was given by

$$E^{WPP}(t,\tau) \propto \int_{-\infty}^{t} \sum_{j} E_{tot}(t',\tau) A_j e^{-\gamma_j (t-t')} \sin\left[\omega_j'(t-t')\right] dt'. \tag{5.6}$$

In the present case, three pulses with two different delays contribute to the total electric field $E_{tot}(t,\tau)$. If τ_p is used as the variable delay, Eq. 5.6 changes to

$$E^{WPP}(t,\tau_p) \propto \int_{-\infty}^{t} \sum_{j=1,2} E_{tot}(t',\tau_p) A_j e^{-\gamma_j (t-t')} \sin\left[\omega_j'(t-t')\right] dt', \tag{5.7}$$

with

$$E_{tot}(t,\tau_p) = E_{\text{start}}(t) + E_{\text{control}}(t+\tau_c) + E_{\text{probe}}(t+\tau_p). \tag{5.8}$$

In order to separate the nonlinear terms behind the sample and since start and control pulse are in a different beam as the probe pulse, Eq. 5.7 can be split into two equations which represent the two beams:

$$E_{sc}^{WPP}(t) \propto \int_{-\infty}^{t} \sum_{j=1,2} \left[E_{\text{start}}(t') + E_{\text{control}}(t'+\tau_c)\right] A_j e^{-\gamma_j (t-t')} \sin\left[\omega_j'(t-t')\right] dt', \tag{5.9}$$

$$E_{probe}^{WPP}(t,\tau_p) \propto \int_{-\infty}^{t} \sum_{j=1,2} \left[E_{\text{probe}}(t'+\tau_p)\right] A_j e^{-\gamma_j (t-t')} \sin\left[\omega_j'(t-t')\right] dt'. \tag{5.10}$$

Here, only the second equation depends on τ_p. For the total nonlinear polarization follows:

$$\begin{aligned} P^{(NL)}(t,\tau_p) &\propto \left(E_{probe}^{WPP}(t,\tau_p) + E_{sc}^{WPP}(t)\right)^3 \\ &= \left(E_{probe}^{WPP}\right)^3 + 3\cdot\left(E_{probe}^{WPP}\right)^2 E_{sc}^{WPP} + 3\cdot E_{probe}^{WPP}\left(E_{sc}^{WPP}\right)^2 + \left(E_{sc}^{WPP}\right)^3. \end{aligned} \tag{5.11}$$

These four terms correspond to the nonlinear signals in the four different directions behind the sample [see Fig. 5.6(c)]. The second term for example corresponds to the direction $2\mathbf{k}_2 + \mathbf{k}_1$, which yields the coherent sum THG signal at the detector as a function of τ_p. Before calculating the intensity according to

$$I_{\text{THG}}(\tau_p) \propto \int^{T_D} \left(P^{(3)}(t,\tau_p)\right)^2 dt \propto \int^{T_D} \left((E^{WPP}(t,\tau_p))^3\right)^2 dt, \tag{5.12}$$

Eq. 5.11 is Fourier transformed to the frequency domain. Only the components around $\pm 3\omega$ are spectrally separated and transformed back into the time domain.

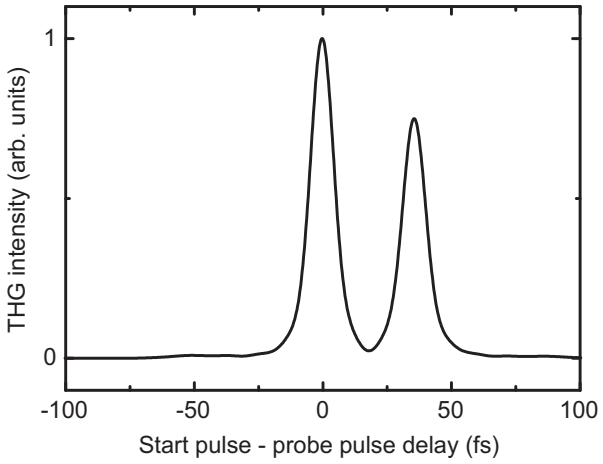

Figure 5.15.: Simulation of the THG signal in the direction $2\mathbf{k}_2 + \mathbf{k}_1$ for a sample with an instantaneous linear response and using the electric field obtained from the laser spectrum. There is just a signal if the probe pulse temporarily overlaps with start or control pulse (compare Figure 5.11)

In the first simulation step, the result for the ITO sample, which has been shown in Fig. 5.11, is reproduced. Due to the instantaneous response of ITO with no resonances in the relevant spectral range, the amplitudes of the two harmonic oscillators (A_1, A_2) are set to zero and only the electric fields of the pulses contribute to the THG signal. The electric fields are obtained again from the linear laser spectrum by assuming a flat spectral phase. The simulations in Fig. 5.15 reproduce the experimental results quite well.

In the next step, contributions of the oscillators are included. First, $sech^2$-pulses centered at 800 nm and with a pulse duration of 8 fs are assumed for the electric field in order to exclude effects of the complicated laser spectrum in the experiment. A single resonant harmonic oscillator with a dephasing time of $T_2^1 = 50$ fs is taken into account ($A_1 = 1, A_2 = 0$). Figure 5.16(a) shows THG signals for this most ideal situation. For the free polarization decay, the amplitude of the probe pulse is set to $E_{control} = 0$. The THG signal simply grows for negative delays τ_p and drops for positive delays. The curve is not symmetric with respect to $\tau_p = 0$ since start and probe pulse enter with different weight in the nonlinear signal. Due to the temporal integration of the signal for each delay step, the signal does not show an oscillatory behavior such as Fig. 5.5. In the destructive case, the control pulse is included. However, the signal does not show a peak at the position of the control pulse such as in the simulation for ITO. The control pulse rather interferes destructively with the polariton polarization and the signal drops to zero much earlier. Additionally, due to the temporal integration, the signal at $\tau_p = 0$ is as well smaller. In the constructive case, the THG signal shows a second maximum at the position of the control pulse due to the constructive interference and it drops later than in the free polarization decay.

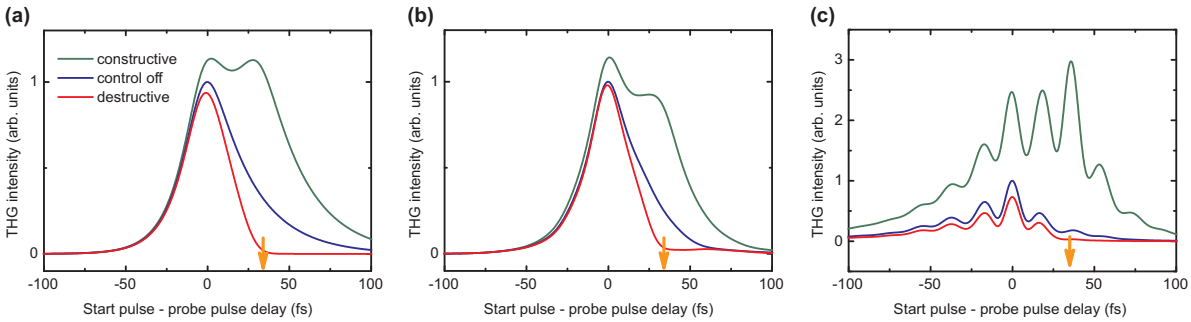

Figure 5.16.: Simulations of the THG signal in the direction $2\mathbf{k}_2 + \mathbf{k}_1$ for a resonant oscillator with a dephasing time of 50 fs (a) using $sech^2$-pulses and (b) using the electric field obtained from the laser spectrum. (c) Same THG signal for two oscillators with the parameters obtained from the fit in Figure 3.3 using the electric field from the laser spectrum.

Following that, the $sech^2$-pulses are replaced by the experimental laser pulses. Figure 5.16(b) shows a similar behavior of the THG signal for a single resonant oscillator as before. However, in the destructive case, the signal drops not completely to zero due to the influence of the satellite pulses. Nevertheless, the contrast of the three curves is nearly maintained. From this simulation it can finally be assumed that the complicated laser spectrum and the satellite pulses do not influence the results too much.

Finally, two harmonic oscillators corresponding to the two WPP modes are taken into account together with the electric field obtained form the laser spectrum. Here the oscillator parameters are chosen which have been obtained by fitting the nonlinear ACF in Fig. 3.3(c). Figure 5.16(c) now shows a drastic change of the shape of the THG signal. The three cases have the same overall behavior but the THG signal is superimposed by the beating modulation which has been observed in the experimental data as well (see Fig. 5.13). From the simulations it is now obvious that the modulation is a consequence of the simultaneous excitation of the short wavelength WPP mode. In total, good agreement to the experimental data in Fig. 5.13(b) is found.

In the simulations it is also possible to include the THG signal in the direction $2\mathbf{k}_1 + \mathbf{k}_2$ in order to observe the fast oscillation in the THG signal. Therefore, when calculating the nonlinear polarization, the term $3 \cdot E_{probe}^{WPP} \left(E_{sc}^{WPP}\right)^2$ is added with a weighting factor f:

$$P^{(NL)}(t, \tau_p) = \left(E_{probe}^{WPP}\right)^2 E_{sc}^{WPP} + f \cdot E_{probe}^{WPP} \left(E_{sc}^{WPP}\right)^2 . \tag{5.13}$$

Figures 5.14(d)-(f) show a very good agreement to the experimental data in Fig. 5.14(a)-(c). The modulation depth of the fast oscillations in the experiment is nearly perfectly reproduced with a factor $f = 0.2$ [183]. If f is increased, the modulation of the fast oscillation would increases as well.

Although the shape of the laser pulses is not ideal in the experiment, results with a large contrast have been achieved with the all-optical control technique. Even though, the dephasing dynamics of the hybrid plasmonic system occur on a timescale of a few tens of femtoseconds only, the control was possible with a high contrast. In further experimental steps in the future, the data quality could be improved with more ideal laser pulses, i.e., Gaussian spectral shape. It can be envisioned that the electric or even magnetic modes in more complicated plasmonic structures such as 3D metamaterials or plasmonic nanoantennas could be controlled in the same fashion.

5.6. First steps towards four-wave mixing in plasmonic nanostructures

So far in the experiments the plasmonic resonances were assumed to be solely homogeneously broadened. This approximation is valid in first place since scattering electron microscope pictures usually reveal nearly no size variations of the plasmonic structures. However, if the dephasing time of a plasmonic excitation is to be determined with high accuracy, inhomogeneous broadening has necessarily to be considered.

From linear and many nonlinear experiments it is not possible to distinguish inhomogeneous from homogeneous broadening [40]. In semiconductor physics, usually FWM experiments are employed for this purpose and the basic ideas are shortly discussed. For further details the reader is referred to [185, 186].

In a typical FWM experiment, two pulses E_1 and E_2 with variable delay and with different wave vectors $\mathbf{k}_1$ and $\mathbf{k}_2$, excite a system and are nonlinearly mixed by a third-order nonlinear process in the sample. So far, the situation is similar to the all-optical control configuration by neglecting the control pulse. However, in a FWM experiment, one makes use of a different nonlinear signal.

So far in the nonlinear regime behind the sample, only the nonlinear signals, which result from an additive combination of the two fundamental wave vectors, were considered. However, in the nonlinear regime, signals at difference frequencies should be generated as well. They are a consequence of the complex conjugate terms in Eq. 5.4 and lead to nonlinear polarization terms such as

$$P(2\mathbf{k}_1 - \mathbf{k}_2) = 3\epsilon_0 \chi^{(3)} E_1^2 E_2^* \tag{5.14}$$

and

$$P(2\mathbf{k}_2 - \mathbf{k}_1) = 3\epsilon_0 \chi^{(3)} E_2^2 E_1^*. \tag{5.15}$$

Figure. 5.17(a) shows these signals in the directions $2\mathbf{k}_2 - \mathbf{k}_1$ and $2\mathbf{k}_1 - \mathbf{k}_2$ schematically.

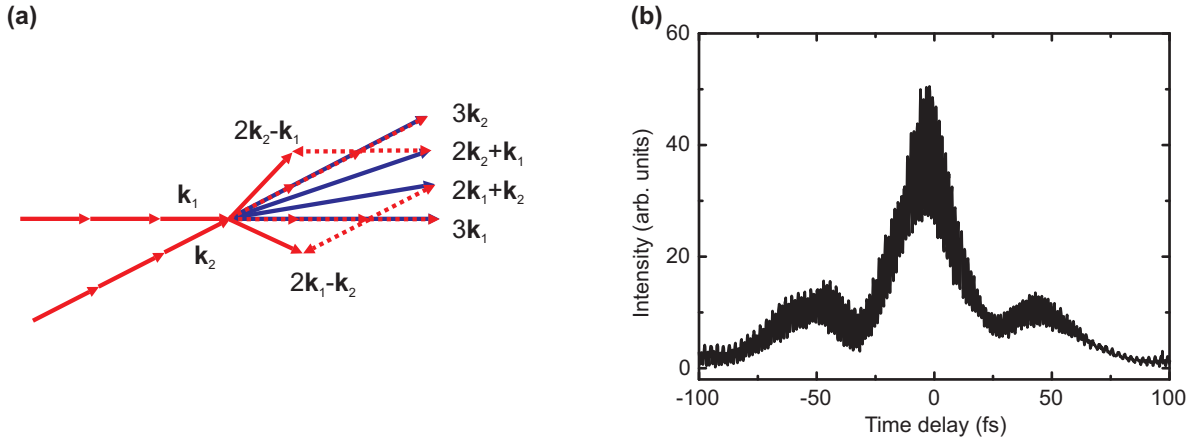

Figure 5.17.: (a) Beam configuration in a FWM experiment. The signal in the direction $2\mathbf{k}_1 - \mathbf{k}_2$ or $2\mathbf{k}_2 - \mathbf{k}_1$ is detected. (b) Measurement using a plasmonic grating.

Due to the complex conjugation, the electric field, which enters linearly into the equations, contributes a negative frequency term. Therefore, the frequency of the nonlinear signal is calculated as $2\omega_1 - \omega_2$ and $2\omega_2 - \omega_1$. In the degenerate case, where ω_1 and ω_2 are similar, the FWM signal is found again at the fundamental frequency.

In order to determine the inhomogeneous broadening, the experiment is performed as follows. The first pulse with wave vector $\mathbf{k}_1$ excites a material polarization in the sample which decays with T_2. After a delay τ, the second pulse with wave vector $\mathbf{k}_2$ arrives at the sample and creates itself a material polarization, which interferes with the remaining coherent part of the first one. Due to the oblique incidence of the light, the interference generates a polarization grating in the sample which radiates its first orders in the directions $\mathbf{k_1}$ and $2\mathbf{k}_2 - \mathbf{k}_1$. The following discussion is restricted to the second term since it is background-free.

In the case of purely homogeneous broadening, the intensity of the scattered signal I_s as a function of the pulse delay τ can be calculated as [186]

$$I_s(\tau) \propto |\mathbf{P}(\tau)|^2 \propto [exp(-\tau/T_2)]^2 \,. \tag{5.16}$$

From the decay of $I_s(\tau)$, the dephasing time T_2 is determined.

In the case of additional inhomogeneous broadening, the coherent part of the material polarization amplitude decays with T_2 as well. However, due to the resonance frequency distribution of the oscillators, their relative phase is lost in a time which is proportional to the inverse of the inhomogeneous broadening $\tau_{in} \propto (\Delta\omega_{in})^{-1}$. Hence, the macroscopic material polarization decays with τ_{in} as well. Due to the complex conjugation of E_2 in Eq. 5.14, the second pulse introduces a time reversal at the delay τ which results in a rephasing of the individual oscillators. After another time τ the oscillators are in phase

again and radiate the so-called photon echo. It can be shown that its temporal width is proportional to τ_{in}, while the previous decay of I_s still depends on T_2. Thus, the observation of the photo echo is a clear indication of inhomogeneous broadening.

By applying these experimental concepts, it should be possible to determine the inhomogeneous broadening of a plasmonic resonance in a FWM experiment as well. FWM experiments with slightly different approaches have been presented before in plasmonic systems [139, 187–189]. Fortunately, the present all-optical control setup provides all necessities for the measurement. In a first experimental step, the signal in either the direction $2\mathbf{k}_2 - \mathbf{k}_1$ or $2\mathbf{k}_1 - \mathbf{k}_2$ behind the sample has to be found. In order to simplify the system, a pure plasmonic grating with a PPP resonance at 800 nm and without a waveguide is used. The control pulse is blocked and the delay between start and probe pulse is set to zero in order to maximize the signal. The FWM signal in the direction $2\mathbf{k}_2 - \mathbf{k}_1$ is detected with a PMT which is optimized for the visible spectral range.

Although the FWM signal is background-free, stray light of the other components has to be suppressed at the detector. Since the FWM signal is at the fundamental frequency, it cannot be separated with a filter from the remaining fundamental light behind the sample. Therefore, a lock-in technique with double modulation is utilized. Both beams are separately modulated at slightly different frequencies Ω_1 and Ω_2 by optical chopper wheels and the signal at the sum $(\Omega_1 + \Omega_2)$ or the difference $(\Omega_1 - \Omega_2)$ frequency is detected with the lock-in. Therefore, the detection is only sensitive to signals which are caused by both pulses.

Once the signal is found, it can be detected as a function of the time delay between the pulses. Figure 5.17(b) shows a first experimental result. The signal has its maximum for perfect pulse overlap but also shows side maxima in the envelope at $\pm$ 50 fs. The signal is furthermore superimposed by a fast oscillation which corresponds to twice the carrier frequency of the pulses. So far, the presence of the FWM signal is proven evident but a deeper understanding of its temporal shape and the fast oscillations is still lacking. This will be object of further investigations in the future.

In order to observe the photon echo in a plasmonic structure, the width of the individual structures could be deterministically varied, hence a desired inhomogeneous broadening would be introduced. Additionally, a temporal resolution of the FWM signal would be necessary in order to extract the width of the photon echo signal. This could be achieved by combining the FWM signal with a third laser pulse with variable delay in another nonlinear medium. Since the amplitude of the FWM signal is very low so far, the last step would be extremely challenging.

6. Conclusion

Localized plasmon polaritons in metallic nanostructures are interesting systems in nanooptics as they can be easily excited by light in the visible range. The coherent collective oscillation of the free conduction band electrons leads to a material polarization which manifests in broad resonances in the linear optical spectra. The resonance position is mainly determined by the size and the shape of the nanostructure and by the dielectric function of the surrounding media. The size of the structures is typically on the order of 10 to 100 nm. After the excitation, the collective electron oscillation loses its coherence due to several elastic and inelastic scattering events. It turns out that the dominating dephasing channel for larger particles is the radiative decay, where photons are emitted from the structures. Typical dephasing times are on the order of 10 fs only.

Within the concept of plasmon hybridization, the influences of the near field coupling of nanoparticle pairs on the linear spectra is discussed. Here, several resonances appear which originate from different eigenmodes of the coupled system where the charge distribution in the two particles is either symmetric or antisymmetric. By utilizing the concept of two coupled classical harmonic oscillators, the shape of the absorption spectra can be successfully modeled. In certain nanostructure geometries, situations can be found where only one fundamental mode (bright mode) is excited by the far field. The other mode (dark mode) is only excitable via the near field coupling. The back-action of the dark mode onto the bright mode leads to a narrow transmission window within the broad plasmon resonance. This concept is equivalent to electromagnetically induced transparency (EIT) in atomic systems and can be utilized in order to tailor the linear optical spectra of plasmonic hybrid systems. Furthermore, these structures are ideal for sensor applications.

The plasmonic modes in metallic nanostructures can be effectively hybridized as well with photonic modes which are excited in dielectric slab waveguides. These waveguides with a thickness of typically 180 nm provide transverse electric (TE) as well as transverse magnetic (TM) modes. By introducing a periodic grating on top of the waveguide, the eigenmodes can be excited by external illumination which is normal to the slab. Dependent on the grating period, narrow Fano resonances appear in the linear spectra. If the grating consists of metallic nanowires in a metallic photonic crystal structure, particle plasmon polaritons can be excited simultaneously in the wires if the light is polarized perpendicular to the wires. If the particle plasmon polaritons are resonant to the TM waveguide modes, the near field coupling leads to a hybridization of the

fundamental modes. In the linear spectra, two resonances appear which correspond to the eigenmodes of the coupled system (waveguide plasmon polariton). Dependent on the coupling efficiency, which is mainly determined by the structure geometry, the two eigenmodes differ in amplitude and linewidth. Therefore, the hybridization to photonic waveguide modes is an ideal method to tailor the linear optical response deterministically. Since the linear optical properties of waveguide plasmon polaritons are well understood, they serve as a model system within this thesis.

The linear optical spectra are obtained from white light transmission measurements. In order to model the linear optical response theoretically, a scattering matrix algorithm is used. Here, the Maxwell equations are solved for each layer of the structure separately and the solutions are coupled to the solutions in the adjacent layers. As a result, the absorbance, transmittance, and reflectance as well as the spectral phase can be calculated.

Together with the shape of the waveguide plasmon polariton eigenmodes in the linear spectra, the dephasing dynamics of the eigenmodes are tailored as well. In order to measure the dephasing dynamics of hybrid plasmonic systems, special techniques have to be employed due to the ultrafast decay of the polariton polarization. Especially, nonlinear interferometric autocorrelation measurements render to be ideal for this purpose. A pair of identical sub-10 fs laser pulses excites the system with a variable time delay. In the nonlinear regime, the pulses together with the excited polariton polarization are mixed in a third-order nonlinear process. The shape of the measured autocorrelation function depends strongly on the dephasing dynamics of the polaritonic system and a beating of the nonlinear signal is observed.

To understand the influence of the polaritonic system on the shape of the autocorrelation function and to determine the dephasing times of the polaritonic eigenmodes, a harmonic oscillator model is utilized where the eigenmodes are described as separate damped oscillators. Via the polariton polarization, the nonlinear autocorrelation function is calculated and fitted to the experimental data. For certain sample configurations, dephasing times up to 90 fs are achieved. By spectrally resolving the third harmonic signal, the autocorrelations reveal additional information. Several spectral components in the nonlinear regime are distinguishable which show a different temporal evolution.

Information about the spectral phase change of the transmitted light, which is induced by the metallic photonic crystal structure, can be retrieved from the spectrally resolved autocorrelations as well. Here, a technique is developed which is based on frequency-resolved optical gating (FROG). This method is usually used in order to characterize ultrashort laser pulses. By Fourier-filtering of the spectrally resolved interferometric autocorrelation trace, the usual FROG trace is obtained. By applying a common retrieval algorithm, the spectral phase is finally extracted. A good agreement is found in comparison to scattering matrix calculations.

In the ultrafast experiments, metallic photonic crystals show a strong nonlinear optical response. However, the origin of the nonlinearity is controversially discussed. In order to achieve a deeper understanding of the nonlinear processes, third harmonic generation spectroscopy experiments are performed. It turns out that metallic photonic crystal structures with an embedded grating in the waveguide tend to be ideal for this kind of experiments. Several peaks in the nonlinear spectra are found and the nonlinear spectra show a complete different shape when compared to the linear spectra.

By carefully varying the structure geometry, one peak in the third harmonic spectrum can be attributed to the particle plasmon resonance in the metallic nanostructures while a second peak originates from the waveguide material. This result is further supported by varying the waveguide material, i.e., its nonlinear susceptibility.

Several theoretical approaches confirm the experimental findings. In a first approach, the third harmonic signal is rigorously calculated from the field distribution in the constituent materials without applying a model for the modes in the system. Since the field distribution spectrally differs in the materials, the peaks in the nonlinear spectra can be unambiguously assigned to the materials. In a second approach, the model of coupled harmonic oscillators is expanded with a nonlinear coupling term. From the qualitative agreement to the experimental data it can be confirmed that the nonlinear coupling can be neglected and the nonlinearities of the fundamental modes, i.e., the particle plasmon polariton and the waveguide mode, are sufficient to explain the nonlinear spectra. In a third theoretical description, the EIT concept is applied. It turns out the the destructive interference of the dark and the bright mode, which are related to the waveguide mode and the particle plasmon mode, respectively, has a consequence on the linear spectra alone and does not occur in the nonlinear regime.

Furthermore, the influence of the group refractive index on the nonlinear response is investigated theoretically. The amplitude of the group index is directly related to the coupling efficiency of the particle plasmon polariton to the waveguide mode. The latter one can be easily varied by changing the position of the plasmonic grating within the waveguide material. A direct relation of the third harmonic signal from the waveguide material to the group index is found. It can be concluded that a high group index slows the light down in the waveguide material which increases the light-matter interaction time and thus the amplitude of the nonlinear signal.

In order to coherently control plasmonic excitations dynamically, their short dephasing times are a serious drawback. However, the hybridization of plasmonic excitations in a metallic photonic crystal structure is a sophisticated method in order to achieve sufficiently long dephasing times. By carefully designing the metallic photonic crystal structure, one of the waveguide plasmon polariton modes can be tuned in resonance to the laser while the other one in barely excited.

Coherent control is accomplished in a pulse sequence configuration. A first pulse gener-

ates a polariton polarization in the sample. Dependent on the exact time delay, a second pulse in the series either turns the polariton polarization completely down or reexcites it. In order to temporally resolve the control process, a third pulse is utilized which is mixed with the polariton polarization in the sample in a nonlinear fashion. Due to its oblique incidence, a variety of nonlinear signal can be observed behind the sample. One of the signals is separated and measured as a function of the time delay of the third pulse.

Although the temporal shape of the ultrashort laser pulses is not ideal so far, a large contrast between the signal in the two configurations is found where the polariton polarization is either turned on or off. The data show that the plasmonic excitation in the metallic photonic crystal structure can be indeed coherently controlled at any desired time after its excitation by all-optical means. Together with the linear polarization, the nonlinear response is controlled as well which renders this technique ideal for ultrafast switching applications in nonlinear optics.

In order to understand all the details of the experimental data, the harmonic oscillator model is further extended in order to account for the three-pulse excitation. A beating phenomenon in the nonlinear signal is attributed to the slight excitation of the second waveguide plasmon polariton mode by the broad laser spectrum. The simulations prove as well that the temporal shape of the laser pulses has only minor influence on the outcome.

Finally, first experimental steps are discussed in order to distinguish between homogeneous and inhomogeneous broadening of plasmonic resonances. From semiconductor physics it is known that four-wave mixing experiments have to be performed for this purpose. The decay of the coherence in the system due to inhomogeneous broadening can be inverted in time by a laser pulse and a photon echo can be detected at a delay after the pulse. The observation of a photon echo would be a clear evidence for inhomogeneous broadening. The experimental configuration of the coherent control experiment is ideal for such kind of experiments. Within this thesis first results are discussed. The four-wave mixing signal was indeed observed in the experiment for a plasmonic nanostructure. In further investigations, it would be very interesting to prove the existence of the photon echo signal as well.

7. Outlook

From the results of this thesis, several further investigations can be envisioned. In the linear optical regime, the embedded metallic photonic crystal structures with the narrow resonances in the linear optical spectra could be utilized as efficient sensors for fluids and gases.

In the nonlinear optical regime, the spectrally resolved autocorrelation measurements together with the extended FROG algorithm could be employed in order to measure the spectral phase of an embedded metallic photonic crystal structure over a broad spectral range. From these measurements, the theoretically expected large group refractive index could be confirmed experimentally. Furthermore, the results could be compared to measurements, where a nonlinear crystal serves as the nonlinear medium and where the metallic photonic crystal structure interacts with the light only in a linear fashion. Any variations of the spectral phase could be directly related to the nonlinear susceptibilities of the structure.

Regarding the origin of the nonlinearity in plasmonic systems, a deeper investigation of the normalized THG signal is necessary which can be below the signal of the substrate. Additionally, higher diffraction orders of nonlinear signal can be studied and compared to the simulations. In the next steps it would be interesting to investigate single plasmonic structures as well. Here, THG imaging measurements could help to reveal the spatial origin of the nonlinear signal within the structures. Furthermore, one could compare the nonlinear signals in the case where the fundamental light is resonant to the PPP with the case where the THG is resonant to the PPP.

The THG spectroscopy technique could be utilized in the future in order to investigate the nonlinear response of more complicated plasmonic structure shapes and metamaterials, as well. By employing the polarization state of the fundamental and the higher harmonic light it could be possible to even determine the nonlinear susceptibility tensors. In 3D metamaterial structures, such as stereometamaterials [190], it could be investigated how the electric as well as the magnetic coupling between the constituent structures influences the nonlinear response. 2D and 3D plasmonic oligomers [60] with single and multiple Fano and/or EIT resonances could be utilized for nonlinear generation as well.

For the all-optical control experiments it would be possible to exclude the linear optical

interaction of the probe pulse with the structure. Such an experiment would require an additional nonlinear medium behind the sample which combines the transmitted fundamental light through the structure with the probe pulse. The variation of the probe pulse delay could be accomplished as well in a fast-scan technique where the delay is varied with a high frequency and the nonlinear signal is measured using a lock-in technique.

More complicated plasmonic structures such as superlattices could be used for the all-optic control experiments. It would be very interesting as well to study the temporal behavior of purely plasmonic hybrid structures without photonic waveguide contribution. In order to avoid inhomogeneous broadening, the hybrid modes in single plasmonic structures could be controlled as well. Furthermore, in magnetic photonic crystals it should be even possible to control optical magnetism on a femtosecond time scale. By spectrally resolving the THG signal which is utilized for the all-optical control experiments, more information about the temporal evolution of the different spectral THG components could be obtained. Certainly, an improvement of the laser pulse shape would enhance the contrast of the results. First steps in this direction by utilizing a pulse shaper are already in progress.

In order to investigate the inhomogeneous broadening of plasmonic nanostructures, not only four-wave mixing experiments but also experiments using nonlinear difference frequency generation or optical rectification would be very interesting. It remains to be seen if the field enhancement around the metallic nanostructures can be utilized for an enhanced terahertz radiation emission.

A. Appendix

A.1. List of acronyms

1D one-dimensional

2D two-dimensional

3D three-dimensional

ACF autocorrelation function

BBO beta barium borate

CCD charge coupled device

EBL electron beam lithography

EIT electromagnetically induced transparency

FROG frequency-resolved optical gating

FWHM full width at half maximum

FWM four-wave mixing

ITO indium tin oxide

MIBK methyl isobutyl ketone

MIIPS multiphoton intrapulse interference phase scan

NMP N-methyl-2-pyrrolidone

PEEM photoemission electron microscopy

PMMA poly(methyl methacrylate)

PMT photomultiplier tube

PPP particle plasmon polariton

SEM scattering electron microscope

SERS surface enhanced Raman scattering

SFG sum frequency generation

SHG second harmonic generation

SPP surface plasmon polariton

SRR split ring resonator

TE transverse electric

THG third harmonic generation

TM transverse magnetic

UV ultraviolet

WPP waveguide plasmon polariton

XFROG cross-correlation frequency-resolved optical gating

List of Figures

Bibliography

[1] Y. N. Xia, P. D. Yang, Y. G. Sun, Y. Y. Wu, B. Mayers, B. Gates, Y. D. Yin, F. Kim, and Y. Q. Yan, *One-dimensional nanostructures: Synthesis, characterization, and applications*, Advanced Materials **15**, 353 (2003).

[2] L. Bányai and S. W. Koch, *Semiconductor Quantum Dots*, volume 2, World Scientific (1993).

[3] H. W. Kroto, J. R. Heath, S. C. Obrien, R. F. Curl, and R. E. Smalley, *C-60 - buckminsterfullerene*, Nature **318**, 162 (1985).

[4] R. H. Baughman, A. A. Zakhidov, and W. A. de Heer, *Carbon nanotubes - the route toward applications*, Science **297**, 787 (2002).

[5] A. Gruber, A. Drabenstedt, C. Tietz, L. Fleury, J. Wrachtrup, and C. vonBorczyskowski, *Scanning confocal optical microscopy and magnetic resonance on single defect centers*, Science **276**, 2012 (1997).

[6] K. J. Vahala, *Optical microcavities*, Nature **424**, 839 (2003).

[7] U. Kreibig and M.Vollmer, *Optical Properties of Metal Clusters*, Springer Verlag (1995).

[8] G. Mie, *Beiträge zur Optik trüber Medien, speziell kolloidaler Metallösungen.*, Ann. Phys. **25**, 377 (1908).

[9] V. G. Veselago, *The electrodynamics of substances with simultaneously negative values of epsilon and mu*, Soviet Physics Uspekhi **10**, 509 (1968).

[10] J. Valentine, S. Zhang, T. Zentgraf, E. Ulin-Avila, D. A. Genov, G. Bartal, and X. Zhang, *Three-dimensional optical metamaterial with a negative refractive index*, Nature **455**, 376 (2008).

[11] J. B. Pendry, *Negative refraction makes a perfect lens*, Physical Review Letters **85**, 3966 (2000).

[12] T. Ergin, N. Stenger, P. Brenner, J. B. Pendry, and M. Wegener, *Three-dimensional invisibility cloak at optical wavelengths*, Science **328**, 337 (2010).

[13] E. Prodan, C. Radloff, N. J. Halas, and P. Nordlander, *A hybridization model for the plasmon response of complex nanostructures*, Science **302**, 419 (2003).

[14] S. Linden, J. Kuhl, and H. Giessen, *Controlling the interaction between light and gold nanoparticles: Selective suppression of extinction*, Physical Review Letters **86**, 4688 (2001).

[15] A. Christ, S. Tikhodeev, N. Gippius, J. Kuhl, and H. Giessen, *Waveguide-plasmon polaritons: Strong coupling of photonic and electronic resonances in a metallic photonic crystal slab*, Physical Review Letters **91**, 183901 (2003).

[16] A. Christ, T. Zentgraf, J. Kuhl, S. G. Tikhodeev, N. A. Gippius, and H. Giessen, *Optical properties of planar metallic photonic crystal structures: Experiment and theory*, Physical Review B **70**, 125113 (2004).

[17] T. Zentgraf, A. Christ, J. Kuhl, N. A. Gippius, S. G. Tikhodeev, D. Nau, and H. Giessen, *Metallodielectric photonic crystal superlattices: Influence of periodic defects on transmission properties*, Physical Review B **73**, 115103 (2006).

[18] D. Nau, A. Schönhardt, C. Bauer, A. Christ, T. Zentgraf, J. Kuhl, M. Klein, and H. Giessen, *Correlation effects in disordered metallic photonic crystal slabs*, Physical Review Letters **98**, 133902 (2007).

[19] C. L. Baciu, J. Becker, A. Janshoff, and C. Sonnichsen, *Protein-membrane interaction probed by single plasmonic nanoparticles*, Nano Letters **8**, 1724 (2008).

[20] N. Liu, T. Weiss, M. Mesch, L. Langguth, U. Eigenthaler, M. Hirscher, C. Sonnichsen, and H. Giessen, *Planar metamaterial analogue of electromagnetically induced transparency for plasmonic sensing*, Nano Letters **10**, 1103 (2010).

[21] C. Loo, A. Lowery, N. J. Halas, J. West, and R. Drezek, *Immunotargeted nanoshells for integrated cancer imaging and therapy*, Nano Letters **5**, 709 (2005).

[22] D. J. Bergman and M. I. Stockman, *Surface plasmon amplification by stimulated emission of radiation: Quantum generation of coherent surface plasmons in nanosystems*, Physical Review Letters **90**, 027402 (2003).

[23] M. I. Stockman, *Spasers explained*, Nature Photonics **2**, 327 (2008).

[24] N. I. Zheludev, S. L. Prosvirnin, N. Papasimakis, and V. A. Fedotov, *Lasing spaser*, Nature Photonics **2**, 351 (2008).

[25] P. Zijlstra, J. W. M. Chon, and M. Gu, *Five-dimensional optical recording mediated by surface plasmons in gold nanorods*, Nature **459**, 410 (2009).

[26] P. Mühlschlegel, H.-J. Eisler, O. J. F. Martin, B. Hecht, and D. W. Pohl, *Resonant optical antennas*, Science **308**, 1607 (2005).

[27] C. Ropers, C. C. Neacsu, T. Elsaesser, M. Albrecht, M. B. Raschke, and C. Lienau, *Grating-coupling of surface plasmons onto metallic tips: A nanoconfined light source*, Nano Letters **7**, 2784 (2007).

[28] P. Ghenuche, S. Cherukulappurath, T. H. Taminiau, N. F. van Hulst, and R. Quidant, *Spectroscopic mode mapping of resonant plasmon nanoantennas*, Physical Review Letters **101**, 116805 (2008).

[29] D. Brinks, F. D. Stefani, F. Kulzer, R. Hildner, T. H. Taminiau, Y. Avlasevich, K. Mullen, and N. F. Van Hulst, *Visualizing and controlling vibrational wave packets of single molecules*, Nature **465**, 905 (2010).

[30] O. L. Muskens, V. Giannini, J. A. Sánchez-Gil, and J. G. Rivas, *Strong enhancement of the radiative decay rate of emitters by single plasmonic nanoantennas*, Nano Letters **7**, 2871 (2007).

[31] M. Pfeiffer, K. Lindfors, C. Wolpert, P. Atkinson, M. Benyoucef, A. Rastelli, O. G. Schmidt, H. Giessen, and M. Lippitz, *Enhancing the optical excitation efficiency of a single self-assembled quantum dot with a plasmonic nanoantenna*, Nano Letters **10**, 4555 (2010).

[32] S. Kim, J. Jin, Y.-J. Kim, I.-Y. Park, Y. Kim, and S.-W. Kim, *High-harmonic generation by resonant plasmon field enhancement*, Nature **453**, 757 (2008).

[33] M. Lippitz, M. A. van Dijk, and M. Orrit, *Third-harmonic generation from single gold nanoparticles*, Nano Letters **5**, 799 (2005).

[34] B. K. Canfield, H. Husu, J. Laukkanen, B. Bai, M. Kuittinen, J. Turunen, and M. Kauranen, *Local field asymmetry drives second-harmonic generation in noncentrosymmetric nanodimers*, Nano Letters **7**, 1251 (2007).

[35] V. K. Valev, A. V. Silhanek, N. Verellen, W. Gillijns, P. Van Dorpe, O. A. Aktsipetrov, G. A. E. Vandenbosch, V. V. Moshchalkov, and T. Verbiest, *Asymmetric optical second-harmonic generation from chiral g-shaped gold nanostructures*, Physical Review Letters **104**, 127401 (2010).

[36] M. W. Klein, C. Enkrich, M. Wegener, and S. Linden, *Second-harmonic generation from magnetic metamaterials*, Science **313**, 502 (2006).

[37] B. Lamprecht, J. Krenn, A. Leitner, and F. R. Aussenegg, *Resonant and off-resonant light-driven plasmons in metal nanoparticles studied by femtosecond-resolution third-harmonic generation*, Physical Review Letters **83**, 4421 (1999).

[38] T. Zentgraf, A. Christ, J. Kuhl, and H. Giessen, *Tailoring the ultrafast dephasing of quasiparticles in metallic photonic crystals*, Physical Review Letters **93**, 243901 (2004).

[39] C. Ropers, D. J. Park, G. Stibenz, G. Steinmeyer, J. Kim, D. S. Kim, and C. Lienau, *Femtosecond light transmission and subradiant damping in plasmonic crystals*, Physical Review Letters **94**, 113901 (2005).

[40] M. W. Klein, T. Tritschler, M.Wegener, and S. Linden, *Lineshape of harmonic generation by metallic nanoparticles and metallic photonic crystal slabs*, Physical Review B **72**, 115113 (2005).

[41] A. P. Heberle, J. J. Baumberg, and K. Köhler, *Ultrafast coherent control and destruction of excitons in quantum wells*, Physical Review Letters **75**, 2598 (1995).

[42] P. B. Johnson and R. W. Christy, *Optical-constants of noble-metals*, Physical Review B **6**, 4370 (1972).

[43] E. A. Stern and R. A. Ferrell, *Surface plasma oscillations of a degenerate electron gas*, Physical Review **120**, 130 (1960).

[44] W. L. Barnes, A. Dereux, and T. W. Ebbesen, *Surface plasmon subwavelength optics*, Nature **424**, 824 (2003).

[45] H. Raether, *Surface Plasmons on Smooth and Rough Surfaces and on Gratings*, Springer Verlag B (1988).

[46] S. V. Popruzhenko, D. F. Zaretsky, and W. Becker, *Third harmonic generation by small metal clusters in a dielectric medium*, Journal of Physics B-atomic Molecular and Optical Physics **39**, 4933 (2006).

[47] W. A. Murray and W. L. Barnes, *Plasmonic materials*, Advanced Materials **19**, 3771 (2007).

[48] T. Zentgraf, *Optische Eigenschaften und Dynamik von photonisch gekoppelten Metall-Partikel-Plasmonen*, Ph.D. thesis, University of Stuttgart (2006).

[49] G. v. Plessen, M. Perner, and J. Feldmann, *Ultrafast relaxation dynamics of electronic excitations in nobel-metal clusters*, Applied Physics B **71**, 381 (2000).

[50] G. Weick, R. A. Molina, D. Weidmann, and R. A. Jalabert, *Liftime of the first and second collective excitations in metallic nanoparticles*, Physical Review B **72**, 115410 (2005).

[51] J. Crowell and R. H. Ritchie, *Radiative decay of coulomb-stimulated plasmons in spheres*, Physical Review **172**, 436 (1968).

[52] B. Lamprecht, J. Krenn, A. Leitner, and F. Aussenegg, *Particle-plasmon decay-time determination by measuring the optical near-field's autocorrelation: influence of inhomogeneous line broadening*, Applied Physics B **69**, 223 (1999).

[53] C. Sönnichsen, T. Franzl, T. Wilk, G. von Plessen, J. Feldmann, O. Wilson, and P. Mulvaney, *Drastic reduction of plasmon damping in gold nanorods*, Physical Review Letters **88**, 077402 (2002).

[54] S. Nie and S. R. Emory, *Probing single molecules and single nanoparticles by surface-enhanced raman scattering*, Science **275**, 1102 (1997).

[55] D. P. Fromm, A. Sundaramurthy, P. J. Schuck, G. Kino, and W. E. Moerner, *Gap-dependent optical coupling of single "bowtie" nanoantennas resonant in the visible*, Nano Letters **4**, 957 (2004).

[56] P. Nordlander, C. Oubre, E. Prodan, K. Li, and M. I. Stockman, *Plasmon hybridizaton in nanoparticle dimers*, Nano Letters **4**, 899 (2004).

[57] H. Haken and H. C. Wolf, *Molecular Physics and Elements of Quantum Chemistry*, Springer Verlag (1995).

[58] F. Wang and Y. R. Shen, *General properties of local plasmons in metal nanostructures*, Physical Review Letters **97**, 206806 (2006).

[59] N. Liu, H. C. Guo, L. W. Fu, S. Kaiser, H. Schweizer, and H. Giessen, *Plasmon hybridization in stacked cut-wire metamaterials*, Advanced Materials **19**, 3628 (2007).

[60] M. Hentschel, M. Saliba, R. Vogelgesang, H. Giessen, A. P. Alivisatos, and N. Liu, *Transition from isolated to collective modes in plasmonic oligomers*, Nano Letters **10**, 2721 (2010).

[61] U. Fano, *Effects of configuration interaction on intensities and phase shifts*, Physical Review **124**, 1866 (1961).

[62] B. Luk'yanchuk, N. I. Zheludev, S. A. Maier, N. J. Halas, P. Nordlander, H. Giessen, and C. T. Chong, *The fano resonance in plasmonic nanostructures and metamaterials*, Nature Materials **9**, 707 (2010).

[63] K. J. Boller, A. Imamoglu, and S. E. Harris, *Observation of electromagnetically induced transparency*, Physical Review Letters **66**, 2593 (1991).

[64] S. E. Harris, *Electromagnetically induced transparency*, Physics Today **50**, 36 (1997).

[65] M. Fleischhauer, A. Imamoglu, and J. P. Marangos, *Electromagnetically induced transparency: Optics in coherent media*, Reviews of Modern Physics **77**, 633 (2005).

[66] C. L. G. Alzar, M. A. G. Martinez, and P. Nussenzveig, *Classical analog of electromagnetically induced transparency*, American Journal of Physics **70**, 37 (2002).

[67] D. D. Smith, H. Chang, K. A. Fuller, A. T. Rosenberger, and R. W. Boyd, *Coupled-resonator-induced transparency*, Physical Review A **69**, 063804 (2004).

[68] M. F. Yanik, W. Suh, Z. Wang, and S. H. Fan, *Stopping light in a waveguide with an all-optical analog of electromagnetically induced transparency*, Physical Review Letters **93**, 233903 (2004).

[69] A. G. Litvak and M. D. Tokman, *Electromagnetically induced transparency in ensembles of classical oscillators*, Physical Review Letters **88**, 095003 (2002).

[70] S. Zhang, D. A. Genov, Y. Wang, M. Liu, and X. Zhang, *Plasmon-induced transparency in metamaterials*, Physical Review Letters **101**, 047401 (2008).

[71] N. Verellen, Y. Sonnefraud, H. Sobhani, F. Hao, V. V. Moshchalkov, P. Van Dorpe, P. Nordlander, and S. A. Maier, *Fano resonances in individual coherent plasmonic nanocavities*, Nano Letters **9**, 1663 (2009).

[72] N. Liu, L. Langguth, T. Weiss, J. Kastel, M. Fleischhauer, T. Pfau, and H. Giessen, *Plasmonic analogue of electromagnetically induced transparency at the drude damping limit*, Nature Materials **8**, 758 (2009).

[73] A. Christ, *Optical properties of metallic photonic crystal structures*, Ph.D. thesis, University of Marburg (2005).

[74] S. G. Tikhodeev, A. L. Yablonskii, E. A. Muljarov, N. A. Gippius, and T. Ishihara, *Quasiguided modes and optical properties of photonic crystal slabs*, Physical Review B **66**, 045102 (2002).

[75] E. Yablonovitch, *Inhibited spontaneous emission in solid-state physics and electronics*, Physical Review Letters **58**, 2059 (1987).

[76] S. John, *Strong localization of photons in certain disordered dielectric superlattices*, Physical Review Letters **58**, 2486 (1987).

[77] C. Weisbuch, M. Nishioka, A. Ishikawa, and Y. Arakawa, *Observation of the coupled exciton-photon mode splitting in a semiconductor quantum microcavity*, Physical Review Letters **69**, 3314 (1992).

[78] G. Khitrova, H. M. Gibbs, M. Kira, S. W. Koch, and A. Scherer, *Vacuum rabi splitting in semiconductors*, Nature Physics **2**, 81 (2006).

[79] V. Yannopapas, E. Paspalakis, and N. V. Vitanov, *Electromagnetically induced transparency and slow light in an array of metallic nanoparticles*, Physical Review B **80**, 035104 (2009).

[80] H. G. Craighead and G. A. Niklasson, *Characterization and optical properties of arrays of small gold particles*, Applied Physics Letters **44**, 1134 (1984).

[81] N. Liu, H. C. Guo, L. W. Fu, S. Kaiser, H. Schweizer, and H. Giessen, *Three-dimensional photonic metamaterials at optical frequencies*, Nature Materials **7**, 31 (2008).

[82] H. C. Guo, D. Nau, A. Radke, X. P. Zhang, J. Stodolka, X. L. Yang, S. G. Tikhodeev, N. A. Gippius, and H. Giessen, *Large-area metallic photonic crystal fabrication with interference lithography and dry etching*, Applied Physics B-Lasers and Optics **81**, 271 (2005).

[83] M. C. Gwinner, E. Koroknay, L. W. Fu, P. Patoka, W. Kandulski, M. Giersig, and H. Giessen, *Periodic large-area metallic split-ring resonator metamaterial fabrication based on shadow nanosphere lithography*, Small **5**, 400 (2009).

[84] D. M. Whittaker and I. S. Culshaw, *Scattering-matrix treatment of patterned multilayer photonic structures*, Physical Review B **60**, 2610 (1999).

[85] T. Weiss, *Adaptive Spatial Resolution and Factorization Rules in an Optical S-Matrix Approach: Improved Convergence for 1D and 2D Metallic Photonic Crystals and Metamaterials*, Master's thesis, University of Stuttgart (2008).

[86] K. Leo, J. Shah, E. O. Goebel, T. C. Damen, S. Schmittrik, W. Schaefer, and K. Kohler, *Coherent oscillations of a wave packet in a semiconductor double-quantum-well structure*, Physical Review Letters **66**, 201 (1991).

[87] K. Minoshima, M. Taiji, K. Misawa, and T. Kobayashi, *Femtosecond nonlinear-optical dynamics of excitons in j-aggregates*, Chemical Physics Letters **218**, 67 (1994).

[88] M. Wolf, *Femtosecond dynamics of electronic excitations at metal surfaces*, Surface Science **377**, 343 (1997).

[89] M. Fierz, K. Siegmann, M. Scharte, and M. Aeschlimann, *Time-resolved 2-photon photoionization on metallic nanoparticles*, Applied Physics B-Lasers and Optics **68**, 415 (1999).

[90] H. Petek, A. P. Heberle, W. Nessler, H. Nagano, S. Kubota, S. Matsunami, N. Moriya, and S. Ogawa, *Optical phase control of coherent electron dynamics in metals*, Physical Review Letters **79**, 4649 (1997).

[91] J. C. Diels and W. Rudolph, *Ultrashort Laser Pulse Phenomena*, Academic Press, 2nd edition (2006).

[92] T. Utikal, *Ultraschnelle Spektroskopie an metallischen photonischen Kristallen*, Master's thesis, University of Bonn (2007).

[93] J. M. Diels, J. J. Fontaine, I. C. McMichael, and F. Simoni, *Control and measurement of ultrashort pulse shapes (in amplitude and phase) with femtosecond accuracy*, Applied Optics **24**, 1270 (1985).

[94] V. V. Lozovoy, I. Pastirk, and M. Dantus, *Multiphoton intrapulse interference. iv. ultrashort laser pulse spectral phase characterization and compensation*, Optics Letters **29**, 775 (2004).

[95] C. Spielmann, L. Xu, and F. Krausz, *Measurement of interferometric autocorrelations: comment*, Applied Optics **36**, 2523 (1997).

[96] S. Pancharatnam, *Generalized theory of interference and its applications*, Proc. Indian Acad. Sci. Sect. A **44**, 247 (1956).

[97] M. U. Wehner, M. H. Ulm, and M. Wegener, *Scanning interferometer stabilized by use of pancharatnam's phase*, Optics Letters **22**, 1455 (1997).

[98] T. Utikal, T. Zentgraf, J. Kuhl, and H. Giessen, *Dynamics and dephasing of plasmon polaritons in metallic photonic crystal superlattices: Time- and frequency-resolved nonlinear autocorrelation measurements and simulations*, Physical Review B **76**, 245107 (2007).

[99] T. Hanke, G. Krauss, D. Trautlein, B. Wild, R. Bratschitsch, and A. Leitenstorfer, *Efficient nonlinear light emission of single gold optical antennas driven by few-cycle near-infrared pulses*, Physical Review Letters **103**, 257404 (2009).

[100] S. Linden, M. Decker, and M. Wegener, *Model system for a one-dimensional magnetic photonic crystal*, Physical Review Letters **97**, 083902 (2006).

[101] M. Geiselmann, *Nichtlineare Optik an Metamaterialien*, Master's thesis, University of Stuttgart (2008).

[102] M. Geiselmann, T. Utikal, M. Lippitz, and H. Giessen, *Tailoring the ultrafast dynamics of the magnetic mode in magnetic photonic crystals*, Physical Review B **81**, 235101 (2010).

[103] C. Enkrich, M. Wegener, S. Linden, S. Burger, L. Zschiedrich, F. Schmidt, J. F. Zhou, T. Koschny, and C. M. Soukoulis, *Magnetic metamaterials at telecommunication and visible frequencies*, Physical Review Letters **95**, 203901 (2005).

[104] D. J. Cho, F. Wang, X. Zhang, and Y. R. Shen, *Contribution of the electric quadrupole resonance in optical metamaterials*, Physical Review B **78**, 121101 (2008).

[105] N. Liu, L. Fu, S. Kaiser, H. Schweizer, and H. Giessen, *Plasmonic building blocks for magnetic molecules in three-dimensional optical metamaterials*, Advanced Materials **20**, 3859 (2008), submitted.

[106] R. Trebino and D. J. Kane, *Using phase retrieval to measure the intensity and phase of ultrashort pulses - frequency-resolved optical gating*, Journal of the Optical Society of America A-Optics Image Science and Vision **10**, 1101 (1993).

[107] K. W. DeLong, R. Trebino, J. Hunter, and W. E. White, *Frequency-resolved optical gating with the use of 2nd-harmonic generation*, Journal of the Optical Society of America B-Optical Physics **11**, 2206 (1994).

[108] T. Tsang, M. A. Krumbügel, K. W. DeLong, D. N. Fittinghoff, and R. Trebino, *Frequency-resolved optical-gating measurements of ultrashort pulses using surface third-harmonic generation*, Optics Letters **21**, 1381 (1996).

[109] J. N. Sweetser, D. N. Fittinghoff, and R. Trebino, *Transient-grating frequency-resolved optical gating*, Optics Letters **22**, 519 (1997).

[110] S. Linden, *Kontrolle der Wechselwirkung zwischen Licht und Partikelplasmonen durch selektive Unterdrückung der Extinktion*, Ph.D. thesis, University of Marburg (2001).

[111] S. Linden, H. Giessen, and J. Kuhl, *XFROG - a new method for amplitude and phase characterization of weak ultrashort pulses*, Physica status solidi (b) **206**, 119 (1998).

[112] I. Amat-Roldán, I. G. Cormack, P. Loza-Alvarez, E. J. Gualda, and D. Artigas, *Ultrashort pulse characterisation with shg collinear-frog*, Optics Express **12**, 1169 (2004).

[113] G. Stibenz and G. Steinmeyer, *Interferometric frequency-resolved optical gating*, Optics Express **13**, 2617 (2005).

[114] A. Anderson, K. S. Deryckx, X. J. G. Xu, G. Steinmeyer, and M. B. Raschke, *Few-femtosecond plasmon dephasing of a single metallic nanostructure from optical response function reconstruction by interferometric frequency resolved optical gating*, Nano Letters **10**, 2519 (2010).

[115] A. Schönhardt, *Pulspropagation in metallischen photonischen Kristallen*, Master's thesis, Univerity of Bonn (2005).

[116] S. V. Fomichev, S. V. Popruzhenko, D. F. Zaretsky, and W. Becker, *Laser-induced nonlinear excitation of collective electron motion in a cluster*, Journal of Physics B-atomic Molecular and Optical Physics **36**, 3817 (2003).

[117] S. Weisenburger, *Nonlinear Microscopy on Plasmonic Nanostructures*, Master's thesis, University of Stuttgart (2010).

[118] K. R. Li, M. I. Stockman, and D. J. Bergman, *Self-similar chain of metal nanospheres as an efficient nanolens*, Physical Review Letters **91**, 227402 (2003).

[119] K. R. Li, M. I. Stockman, and D. J. Bergman, *Enhanced second harmonic generation in a self-similar chain of metal nanospheres*, Physical Review B **72**, 153401 (2005).

[120] R. W. Boyd, *Nonlinear Optics*, Elsevier, 3rd edition (2008).

[121] M. I. Stockman, D. J. Bergman, C. Anceau, S. Brasselet, and J. Zyss, *Enhanced second-harmonic generation by metal surfaces with nanoscale roughness: Nanoscale dephasing, depolarization, and correlations*, Physical Review Letters **92**, 057402 (2004).

[122] J. B. Pendry, A. J. Holden, D. J. Robbins, and W. J. Stewart, *Magnetism from conductors and enhanced nonlinear phenomena*, Ieee Transactions on Microwave Theory and Techniques **47**, 2075 (1999).

[123] M. W. Klein, *Nonlinear Optics of Metallic Photonic Crystal Slabs and Planar Metamaterials*, Ph.D. thesis, University of Karlsruhe (2007).

[124] S. Linden, C. Enkrich, M. Wegener, J. F. Zhou, T. Koschny, and C. M. Soukoulis, *Magnetic response of metamaterials at 100 terahertz*, Science **306**, 1351 (2004).

[125] S. I. Bozhevolnyi, J. Beermann, and V. Coello, *Direct observation of localized second-harmonic enhancement in random metal nanostructures*, Physical Review Letters **90**, 197403 (2003).

[126] S. Y. Chen, A. Maksimchuk, and D. Umstadter, *Experimental observation of relativistic nonlinear Thomson scattering*, Nature **396**, 653 (1998).

[127] F. B. P. Niesler, N. Feth, S. Linden, J. Niegemann, J. Gieseler, K. Busch, and M. Wegener, *Second-harmonic generation from split-ring resonators on a GaAs substrate*, Optics Letters **34**, 1997 (2009).

[128] A. A. Zharov, I. V. Shadrivov, and Y. S. Kivshar, *Nonlinear properties of left-handed metamaterials*, Physical Review Letters **91**, 037401 (2003).

[129] A. K. Popov, V. V. Slabko, and V. M. Shalaev, *Second harmonic generation in left-handed metamaterials*, Laser Physics Letters **3**, 293 (2006).

[130] Y. Zeng, W. Hoyer, J. J. Liu, S. W. Koch, and J. V. Moloney, *Classical theory for second-harmonic generation from metallic nanoparticles*, Physical Review B **79**, 235109 (2009).

[131] F. X. Wang, F. J. Rodriguez, W. M. Albers, R. Ahorinta, J. E. Sipe, and M. Kauranen, *Surface and bulk contributions to the second-order nonlinear optical response of a gold film*, Physical Review B **80**, 233402 (2009).

[132] C. Bauer, *Einfluss der photonischen Kopplung auf die optischen Eigenschaften von plasmonischen Kristallen*, Master's thesis, University of Stuttgart (2006).

[133] T. Zentgraf, S. Zhang, R. F. Oulton, and X. Zhang, *Ultranarrow coupling-induced transparency bands in hybrid plasmonic systems*, Physical Review B **80**, 195415 (2009).

[134] D. Nau, A. Seidel, R. B. Orzekowsky, S. H. Lee, S. Deb, and H. Giessen, *Hydrogen sensor based on metallic photonic crystal slabs*, Optics Letters **35**, 3150 (2010).

[135] S. Link, C. Burda, B. Nikoobakht, and M. A. El-Sayed, *Laser-induced shape changes of colloidal gold nanorods using femtosecond and nanosecond laser pulses*, Journal of Physical Chemistry B **104**, 6152 (2000).

[136] R. W. Boyd, *Nonlinear Optics*, Elsevier, 3rd edition (2008).

[137] N. Ueda, H. Kawazoe, Y. Watanabe, M. Takata, M. Yamane, and K. Kubodera, *3rd-order nonlinear optical susceptibilities of electroconductive oxide thin-films*, Applied Physics Letters **59**, 502 (1991).

[138] T. Paul, C. Rockstuhl, and F. Lederer, *A numerical approach for analyzing higher harmonic generation in multilayer nanostructures*, Journal of the Optical Society of America B-Optical Physics **27**, 1118 (2010).

[139] J. Renger, R. Quidant, N. van Hulst, and L. Novotny, *Surface-enhanced nonlinear four-wave mixing*, Physical Review Letters **104**, 046803 (2010).

[140] B. Corcoran, C. Monat, C. Grillet, D. J. Moss, B. J. Eggleton, T. P. White, L. O'Faolain, and T. F. Krauss, *Green light emission in silicon through slow-light enhanced third-harmonic generation in photonic-crystal waveguides*, Nature Photonics **3**, 206 (2009).

[141] C. Monat, B. Corcoran, M. Ebnali-Heidari, C. Grillet, B. J. Eggleton, T. P. White, L. O'Faolain, and T. F. Krauss, *Slow light enhancement of nonlinear effects in silicon engineered photonic crystal waveguides*, Optics Express **17**, 2944 (2009).

[142] M. I. Stockman, S. V. Faleev, and D. J. Bergman, *Coherent control of femtosecond energy localization in nanosystems*, Physical Review Letters **88**, 067402 (2002).

[143] M. Wollenhaupt, *Pulse shaping and coherent control* (2009), ultrafast Nanooptics Summer School, Bad Dürkheim, Germany.

[144] T. H. Stievater, X. Q. Li, D. G. Steel, D. Gammon, D. S. Katzer, D. Park, C. Piermarocchi, and L. J. Sham, *Rabi oscillations of excitons in single quantum dots*, Physical Review Letters **87**, 133603 (2001).

[145] X. Q. Li, Y. W. Wu, D. Steel, D. Gammon, T. H. Stievater, D. S. Katzer, D. Park, C. Piermarocchi, and L. J. Sham, *An all-optical quantum gate in a semiconductor quantum dot*, Science **301**, 809 (2003).

[146] T. Unold, K. Mueller, C. Lienau, T. Elsaesser, and A. D. Wieck, *Optical stark effect in a quantum dot: Ultrafast control of single exciton polarizations*, Physical Review Letters **92**, 157401 (2004).

[147] T. Unold, K. Mueller, C. Lienau, T. Elsaesser, and A. D. Wieck, *Optical control of excitons in a pair of quantum dots coupled by the dipole-dipole interaction*, Physical Review Letters **94**, 137404 (2005).

[148] T. Voss, I. Ruckmann, J. Gutowski, V. M. Axt, and T. Kuhn, *Coherent control of the exciton and exciton-biexciton transitions in the generation of nonlinear wave-*

mixing signals in a semiconductor quantum well, Physical Review B **73**, 115311 (2006).

[149] S. Leinss, T. Kampfrath, K. von Volkmann, M. Wolf, J. T. Steiner, M. Kira, S. W. Koch, A. Leitenstorfer, and R. Huber, *Terahertz coherent control of optically dark paraexcitons in Cu2O*, Physical Review Letters **101**, 246401 (2008).

[150] P. Brumer and M. Shapiro, *Control of unimolecular reactions using coherent-light*, Chemical Physics Letters **126**, 541 (1986).

[151] P. Brumer and M. Shapiro, *Coherence chemistry - controlling chemical-reactions with lasers*, Accounts of Chemical Research **22**, 407 (1989).

[152] C. Chen, Y. Y. Yin, and D. S. Elliott, *Interference between optical-transitions*, Physical Review Letters **64**, 507 (1990).

[153] D. J. Tannor and S. A. Rice, *Control of selectivity of chemical-reaction via control of wave packet evolution*, Journal of Chemical Physics **83**, 5013 (1985).

[154] A. M. Weiner, *Femtosecond pulse shaping using spatial light modulators*, Review of Scientific Instruments **71**, 1929 (2000).

[155] R. S. Judson and H. Rabitz, *Teaching lasers to control molecules*, Physical Review Letters **68**, 1500 (1992).

[156] C. J. Bardeen, V. V. Yakovlev, K. R. Wilson, S. D. Carpenter, P. M. Weber, and W. S. Warren, *Feedback quantum control of molecular electronic population transfer*, Chemical Physics Letters **280**, 151 (1997).

[157] V. Blanchet, C. Nicole, M. A. Bouchene, and B. Girard, *Temporal coherent control in two-photon transitions: From optical interferences to quantum interferences*, Physical Review Letters **78**, 2716 (1997).

[158] V. Blanchet, M. A. Bouchene, and B. Girard, *Temporal coherent control in the photoionization of Cs-2: Theory and experiment*, Journal of Chemical Physics **108**, 4862 (1998).

[159] D. Meshulach and Y. Silberberg, *Coherent quantum control of two-photon transitions by a femtosecond laser pulse*, Nature **396**, 239 (1998).

[160] D. Meshulach and Y. Silberberg, *Coherent quantum control of multiphoton transitions by shaped ultrashort optical pulses*, Physical Review A **60**, 1287 (1999).

[161] A. Assion, T. Baumert, M. Bergt, T. Brixner, B. Kiefer, V. Seyfried, M. Strehl,

and G. Gerber, *Control of chemical reactions by feedback-optimized phase-shaped femtosecond laser pulses*, Science **282**, 919 (1998).

[162] T. Brixner, N. H. Damrauer, P. Niklaus, and G. Gerber, *Photoselective adaptive femtosecond quantum control in the liquid phase*, Nature **414**, 57 (2001).

[163] D. J. Gauthier, *Alternate schemes for the coherent laser control of chemical-reactions*, Journal of Chemical Physics **99**, 1618 (1993).

[164] P. Nuernberger, G. Vogt, T. Brixner, and G. Gerber, *Femtosecond quantum control of molecular dynamics in the condensed phase*, Physical Chemistry Chemical Physics **9**, 2470 (2007).

[165] S. H. Shi, A. Woody, and H. Rabitz, *Optimal-control of selective vibrational-excitation in harmonic linear-chain molecules*, Journal of Chemical Physics **88**, 6870 (1988).

[166] P. Brumer and M. Shapiro, *One photon mode selective control of reactions by rapid or shaped laser-pulses - an emperor without clothes*, Chemical Physics **139**, 221 (1989).

[167] V. I. Prokhorenko, A. M. Nagy, S. A. Waschuk, L. S. Brown, R. R. Birge, and R. J. D. Miller, *Coherent control of retinal isomerization in bacteriorhodopsin*, Science **313**, 1257 (2006).

[168] M. Joffre, *Comment on "coherent control of retinal isomerization in bacteriorhodopsin"*, Science **317**, 453b (2007).

[169] V. I. Prokhorenko, A. M. Nagy, S. A. Waschuk, L. S. Brown, R. R. Birge, and R. J. D. Miller, *Response to comment on "coherent control of retinal isomerization in bacteriorhodopsin"*, Science **317**, 5837 (2007).

[170] P. C. M. Planken, I. Brener, M. C. Nuss, M. S. C. Luo, and S. L. Chuang, *Coherent control of terahertz charge oscillations in a coupled-quantum-well using phase-locked optical pulses*, Physical Review B **48**, 4903 (1993).

[171] M. U. Wehner, D. S. Chemla, and M. Wegener, *Electron-lo-phonon quantum kinetics in semiconductor quantum wells*, Physical Review B **58**, 3590 (1998).

[172] G. S. Wiederhecker, A. Brenn, H. L. Fragnito, and P. S. J. Russell, *Coherent control of ultrahigh-frequency acoustic resonances in photonic crystal fibers*, Physical Review Letters **100**, 203903 (2008).

[173] T. Kampfrath, A. Sell, G. Klatt, A. Pashkin, S. Mährlein, T. Dekorsy, M. Wolf,

M. Fiebig, A. Leitenstorfer, and R. Huber, *Coherent terahertz control of antiferromagnetic spin waves*, Nature Photonics **5**, 31 (2011).

[174] D. S. Yee, K. J. Yee, S. C. Hohng, D. S. Kim, T. Meier, and S. W. Koch, *Coherent control of absorption and polarization decay in a gaas quantum well: Time and spectral domain studies*, Physical Review Letters **84**, 3474 (2000).

[175] M. I. Stockman, D. J. Bergman, and T. Kobayashi, *Coherent control of nanoscale localization of ultrafast optical excitation in nanosystems*, Physical Review B **69**, 054202 (2004).

[176] M. Durach, A. Rusina, and M. I. Stockman, *Toward full spatiotemporal control on the nanoscale*, Nano Letters **7**, 3145 (2007).

[177] M. I. Stockman, *Ultrafast nanoplasmonics under coherent control*, New Journal of Physics **10**, 025031 (2008).

[178] M. I. Stockman, *Femtosecond optical responses of disordered clusters, composites, and rough surfaces: "the ninth wave" effect*, Physical Review Letters **84**, 1011 (2000).

[179] X. T. Li and M. I. Stockman, *Highly efficient spatiotemporal coherent control in nanoplasmonics on a nanometer-femtosecond scale by time reversal*, Physical Review B **77**, 195109 (2008).

[180] A. Kubo, K. Onda, H. Petek, Z. Sun, Y. S. Jung, and H. K. Kim, *Femtosecond imaging of surface plasmon dynamics in a nanostructured silver film*, Nano Letters **5**, 1123 (2005).

[181] M. Aeschlimann, M. Bauer, D. Bayer, T. Brixner, F. J. G. de Abajo, W. Pfeiffer, M. Rohmer, C. Spindler, and F. Steeb, *Adaptive subwavelength control of nano-optical fields*, Nature **446**, 301 (2007).

[182] M. Aeschlimann, M. Bauer, D. Bayer, T. Brixner, S. Cunovic, F. Dimler, A. Fischer, W. Pfeiffer, M. Rohmer, C. Schneider, F. Steeb, C. Struber, and D. V. Voronine, *Spatiotemporal control of nanooptical excitations*, Proceedings of the National Academy of Sciences of the United States of America **107**, 5329 (2010).

[183] T. Utikal, M. I. Stockman, A. P. Heberle, M. Lippitz, and H. Giessen, *All-optical control of the ultrafast dynamics of a hybrid plasmonic system*, Physical Review Letters **104**, 113903 (2010).

[184] K. F. MacDonald, Z. L. Samson, M. I. Stockman, and N. I. Zheludev, *Ultrafast active plasmonics*, Nature Photonics **3**, 55 (2009).

[185] M. Wegener, D. S. Chemla, S. Schmitt-Rink, and W. Schäfer, *Line shape of time-resolved four-wave mixing*, Physical Review A **42**, 5675 (1990).

[186] C. F. Klingshirn, *Semiconductor Optics*, Springer Verlag Berlin (2007).

[187] M. Danckwerts and L. Novotny, *Optical frequency mixing at coupled gold nanoparticles*, Physical Review Letters **98**, 026104 (2007).

[188] S. Palomba and L. Novotny, *Nonlinear excitation of surface plasmon polaritons by four-wave mixing*, Physical Review Letters **101**, 056802 (2008).

[189] J. Renger, R. Quidant, N. van Hulst, S. Palomba, and L. Novotny, *Free-space excitation of propagating surface plasmon polaritons by nonlinear four-wave mixing*, Physical Review Letters **103**, 266802 (2009).

[190] N. Liu, H. Liu, S. N. Zhu, and H. Giessen, *Stereometamaterials*, Nature Photonics **3**, 157 (2009).

Lebenslauf

Persönliche Daten:

Nachname	Utikal
Vorname	Tobias
Geburtsdatum/-ort	05.07.1980 / Neuwied
Familienstand	ledig
Adresse	Rosenbergstr. 95, 70193 Stuttgart
Telefon	0711-1239361
E-Mail	t.utikal@physik.uni-stuttgart.de, tutikal@gmx.de

Schulbildung:

08/1987 - 06/2000	Grundschule und Gymnasium in Neuwied, Abschluss: Abitur

Wehrdienst:

07/2000 - 08/2001	Deutsche Marine, Navigator an Bord einer Fregatte

Studium:

10/2001 - 01/2007	Studium der Physik an der Universität Bonn, Nebenfächer: Astronomie, Volkswirtschaftslehre, Nuklearmedizin
08/2003	Vordiplom in Physik, Note: sehr gut
01/2006 - 01/2007	Externe Diplomarbeit an der Universität Stuttgart
01/2007	Diplom in Physik, Note: sehr gut

Promotion:

02/2007 - heute	Promotionsstudium an der Universität Stuttgart und am Max-Planck-Institut für Festkörperforschung, Stuttgart

Praktika:

01/2003 - 12/2003	Studentischer Operateur am Elektronenbeschleuniger der Universität Bonn
09/2003 - 10/2003	Werkstudent am Max-Planck-Institut für Plasmaphysik, Garching
03/2004	Wissenschaftliche Hilfskraft am CERN, Genf
07/2004 - 09/2004	Teilnahme am DESY Summer-Student Programm, Hamburg
10/2004 - 04/2005	Wissenschaftliche Hilfskraft am Institut für angewandte Physik, Uni Bonn
04/2005 - 06/2005	Praktikum im Qualitätsmanagement der Robert Bosch GmbH

Sonstiges:

08/2005 - heute	Förderstudent der Robert Bosch GmbH
07/2008	Dr.-Heinrich-Düker Preis
	Sprachen: Englisch, Französisch, Latein

Acknowledgments

Finally I would like to thank all the people how contributed to the success of this thesis.

In the first place I would like to thank my advisor Prof. Dr. Harald Giessen for giving me the opportunity to prepare this thesis at his institute and for his endless enthusiasm and continuous support. Additionally I would like to thank him for all the conferences I was able to attend and the involvement in the institute administration.

I thank Prof. Dr. Tilman Pfau for the interest in my work and for being my co-advisor and Prof. Dr. H. P. Büchler as dissertation committee member.

I would like to express my gratitude as well to Prof. Dr. Markus Lippitz for providing the lab space for the experiments at the Max Planck Institute for Solid State Research, Stuttgart and for many fruitful discussions and suggestions.

Despite his absence from Stuttgart, Dr. Thomas Zentgraf was a valuable supervisor. He always provided me with countless suggestions and advices and had a continuous interest in the progress. I thank him very much.

For successful collaboration I would like to thank Prof. Dr. Albert P. Heberle, Prof. Dr. Mark I. Stockman, and Prof. Dr. Sergei G. Tikhodeev as well as the research groups of Prof. Dr. Falk Lederer, Prof. Dr. Torsten Meier, and Prof. Dr. Markus B. Raschke.

Furthermore, I would like to thank Ulrike Waizmann and Thomas Reindl from the Max Planck Institute for Solid State Research for their invaluable help concerning sample preparation.

I express my gratitude to all members of the 4th Physics Institute at the University of Stuttgart and the Junior Research Group *Ultrafast Nanooptics* at the Max Planck Institute for Solid State Research for the nice and warm working atmosphere. Especially Tolga Ergin, Mario Hentschel, and Christian Wolpert should be mentioned.

Last but not least I would like to thank my parents, my family, and Svenja for their support throughout all the years. You helped me through all ups and downs and took a lot of load off me.